Finite-Size Effects
In A One-Dimensional Kondo-Box

Dissertation

zur
Erlangung des Doktorgrades (Dr. rer. nat)
der
Mathematisch-Naturwissenschaftlichen Fakultät
der
Rheinischen Friedrich-Wilhelms Universität Bonn

vorgelegt von
Thomas Hand
aus Bonn
Februar 2006

Tag der Abgabe: 16. Februar 2006

Tag der Prüfung 16. Mai 2006

Diese Dissertation ist auf dem Hochschulschriftenserver der ULB Bonn http://hss.ulb.uni-bonn.de/diss_online elektronisch publiziert.

Ich versichere, dass ich diese Arbeit selbständig verfasst und keine anderen als die angegebenen Quellen und Hilfsmittel benutzt sowie die Zitate kenntlich gemacht habe.

Bonn, den 14. Februar 2006

Referent:	Prof. Dr. H. Monien
Korreferent:	Prof. Dr. H. Dreiner

Finite-Size Effects in a One-Dimensional Kondo-Box

Thomas Hand

14. 02. 2006

Abstract

We study the correlation effects induced by a Kondo impurity embedded in a quantum box, using as a model a one-dimensional tight-binding band with a finite number of lattice sites which is coupled to an Anderson impurity. The model is solved by means of the density-matrix renormalization-group (DMRG) including the Lanczos method as well as the correction vector method. We examine systems with more than 500 sites retaining up to 2600 states. We define the Kondo temperature T_K for the case of a discrete conduction electron density of states (level spacing ΔE). The strength of the correlations, indicated by the weight of the Kondo resonance, W, is determined by the local conduction density of states at the impurity site, x_0. W depends both on the symmetry of the conduction electron wave function at the Fermi edge, $\Psi_0(x)$, and on the impurity position x_0. We explain why the size of the Kondo peak fluctuates by changing the particle number N between even and odd. We calculate the spin-correlations of the impurity spin and the spin of the conduction band and define a correlation length for a finite system, $l_k^{\rm num}$. We examine systems where the Kondo cloud — measured by $l_k^{\rm num}$ — is fully developed within the finite system. We show how the size of the Kondo peak corresponds to the size of the Kondo cloud.

Contents

Introduction

In the 1930s it was known that the resistivity of metals can show different behavior when cooling down to low temperatures: For some metals, like copper and gold, the resistivity decreases until a finite constant value is approached and then saturates at a constant value. For other metals, like niobium or aluminum, the resistivity vanishes at a critical temperature T_C and the material becomes a superconductor. This behavior changes dramatically when single magnetic atoms, such as cobalt, are added.

The resistivity decreases for low temperatures until a finite temperature is reached and then increases again. This is called the Kondo-Effect [1, 2, 3], and it could not be explained for decades.

In 1964 it was Jun Kondo [4] who solved the problem by investigating the scattering of conduction electrons with a single magnetic impurity. The Kondo Hamiltonian describes the interaction of free conduction electrons with a fixed spin. By expanding it up to second order of perturbation theory in the coupling J, he found that the second term could be larger than the first term. A $\ln(T)$ term arises, which raises the resistivity for low temperatures if the coupling is antiferromagnetic and if the term is included with the phonon contribution to the resistivity.

A few years earlier, in 1961, P. W. Anderson had suggested another model, the so-called Anderson model or SIAM (Single Impurity Anderson Model) [5]. It describes the interaction of conduction electrons with an additional site via superexchange. One site on a free tight-binding chain is coupled to a site with a negative level ε_d and a Coulomb repulsion term. Since this describes the scattering off an impurity that has an internal degree of freedom, namely the spin, this problem is a real many-body problem and cannot be reduced to a simple single-electron scattering problem.

In the ground state the impurity site is occupied by one electron on average, due to the low-lying level. This electron builds a singlet with a conduction electron at the Fermi level. This spin exchange changes the spectrum of the system and a so-called Kondo peak is generated at the Fermi level.

In 1974 D. Haldane proved that the Kondo temperature is determined

by the parameters of the Anderson Hamiltonian only. Therefore, all physical quantities can be expressed in units of T_K instead of the parameters of the Hamiltonian.

The problem of Kondo's perturbative approach is that the term diverges for $T \to 0$, and resistivity would be infinite at $T = 0$, which is unphysical. The key idea of the remedy for this problem is *scaling*, which was also introduced by Anderson [6]. By integrating out higher excitations, the effective coupling between the impurity site and the conduction electrons is increased. The approach failed at low energies, too, but the idea of *scaling* was picked up by K. Wilson. In 1974 he developed the Numerical Renormalization Group, a powerful tool containing ideas of the renormalization group from field theory as well as scaling ideas from condensed matter explaining the Kondo phenomena.

In the last few years Kondo physics became more interesting for physicists again, because nanotechnology is offering new experiments [7, 8, 9]. By means of scanning tunneling microscopy (STM) it is now possible to manipulate, investigate and create small Kondo boxes, a device consisting of a few hundred atoms and one single impurity. One might expect that in the near future it will be possible to build Kondo boxes consisting of only a few atoms. In these samples the conduction electron spectrum becomes discrete with a nonzero mean level spacing. This results in many new effects, e. g. the splitting of the Kondo peak into many sub-peaks.

The main part of this thesis deals with the examination of a Kondo box, a tight-binding chain with a finite number of lattice sites coupled to a single Anderson impurity, by means of the density-matrix renormalization-group (DMRG). This powerful numerical tool was developed by S. R. White [10, 11, 12] and is, roughly speaking, an extension of Wilson's Numerical Renormalization Group to realspace systems. The DMRG makes it possible to examine one-dimensional systems with a very high accuracy. We will explain the method in detail.

One focus of interest are dynamical properties, especially the spectral density on the impurity. We will show that — although we do not use the *standard* SIAM — we can find a peak at the Fermi edge, resulting from the interaction on the impurity, which can be interpreted as a Kondo peak. We explain the behaviour of this peak for different setups: Even and odd number of particles in the system, different system sizes, and other various parameters. We explain how the calculation of the Kondo temperature can be applied to our system.
The other focus of interest is the *holy grail* of Kondo physics: The Kondo screening cloud. We will show results for the correlation function of the im-

purity spin and the spins on the conduction band. We define a *numerical* correlation length l_k^{num} and show that it decreases with increasing T_K. For large systems and large T_K, the spin-spin correlations do not change for small distances.

The thesis is organized as follows: In chapter 1 we will give a brief introduction in the Anderson and Kondo model. We will also give some insight and motivation of experiments. Since the Green's function and the spectral density play a fundamental role in this thesis, both concepts are explained in detail. Chapter 2 deals with various numerical methods: We start from exact diagonalization, introduce the Lanczos algorithm and show how it can be used to calculate dynamical properties. After the Bethe Ansatz for a Hubbard chain with open boundary conditions and the NRG, we will explain the DMRG in detail: Infinite and finite system algorithm, handling of operators, transformation of the wave function, measurements of expectation values and correlation functions, and dynamical properties with the Lanczos vector and the correction vector method.
We will present our results of the dynamical properties and the spin-spin correlations of a Kondo box in chapter 3. Chapter 4 shows results for a Hubbard ring and a t-J ladder with long range Coulomb interaction with DMRG. We will show what has to be done to keep the number of operations at a feasible level.
In chapter 5 we present the dynamical mean-field theory (DMFT) and its extension, the cellular DMFT (CDMFT). We show the self-consistent loop and try to clarify all technical terms used in these methods.
We offer a conclusion and a discussion of further research at the end of this thesis.

Chapter 1

Theory and Experiments

In this chapter I will give a brief introduction in the Anderson and Kondo model. We will also give some insight and motivation of experiments.

1.1 Introduction and Models

The theory of magnetic impurities in metals is a field that has attracted a lot of attention in the last 40 years. A Hamiltonian for this problem can be written like this:

$$H = \sum_i \left(\frac{p_i^2}{2m} + U(r_i) + V_{imp}(r_i) \right) + \frac{1}{2} \sum_{i \neq j} \frac{e^2}{|r_i - r_j} + \sum_i \lambda(r_i) \cdot \sigma_i \qquad (1.1)$$

The first two terms describe the kinetic and the potential energy of the electrons in the host metal. The third term describes the interaction with the magnetic impurity. The fourth and fifth term represent the Coulomb repulsion and the spin-orbit interaction. When we only concentrate on simple metals which have a broad conduction band, the electrons can be assumed to move freely and independently in a periodic potential. The long Coulomb repulsion is screened and the electrons can be described as quasi-particles. By neglecting the quasi-particle interaction the conduction electrons in the host metal can be described by a single-electron Hamiltonian

$$H = \sum_{k,\sigma} \varepsilon_k c_{k,\sigma}^\dagger c_{k,\sigma}. \qquad (1.2)$$

$c_{k,\sigma}^\dagger$ and $c_{k,\sigma}$ are creation and annihilation operators, where k represents the wave vector and σ the spin. Another approximation is that one is not concerned about the energies ε_k, but characterizes the conduction electrons by

a density of states given by[1]

$$\rho_0 = \sum_k \delta(\varepsilon - \varepsilon_k). \tag{1.3}$$

By introducing an effective impurity potential $V_{\text{imp}}^{\text{eff}}(r)$ one can write the Hamiltonian of the conduction band electrons and the impurity as

$$H = \sum_{k,\sigma} \varepsilon_k c_{k,\sigma}^\dagger c_{k,\sigma} + \sum_{k,k',\sigma} V_{k,k'} c_{k,\sigma}^\dagger c_{k',\sigma}, \tag{1.4}$$

where $V_{k,k'}(r) = \langle k|V_{\text{imp}}^{\text{eff}}(r)|k'\rangle$. A local impurity can be sufficiently attractive to bind a conduction electron. An electron in this bound state will be localized in the vicinity of the impurity and its wavefunction will fall off exponentially with increasing distance r from the impurity. But even if the potential is not strong enough to bind an electron, it may still be attractive enough to localize a conduction electron due to resonant scattering for some time in the vicinity of the impurity. These virtual bound states occur for rare earth or transition metal impurities when the d or f level lie within the conduction band of the host metal. The Anderson model uses the atomic d functions of the isolated impurity as starting point, which are modified due to the presence of the ions of the host metal. The Hamiltonian is given by

$$\begin{aligned} H &= \sum_{k,\sigma} \varepsilon_k c_{k,\sigma}^\dagger c_{k,\sigma} \\ &+ \sum_{\sigma} \varepsilon_d n_{d,\sigma} + U n_{d,\uparrow} n_{d,\downarrow} \\ &+ \sum_{k,\sigma} \left(V_k c_{d,\sigma}^\dagger c_{k,\sigma} + V_k^* c_{k,\sigma}^\dagger c_{d,\sigma} \right), \end{aligned} \tag{1.5}$$

where the first term describes the conduction electrons in the host metal. The second term describes the physics of the isolated impurity, which inhibits a chemical potential ε_d as well as a Coulomb repulsion U. The third term represents the interaction or connection of the impurity and the conduction band of the host metal. To exhibit a local moment, it is necessary that the impurity is single occupied. This requires that $\varepsilon_d < \varepsilon_F$ and $2\varepsilon_d + U > \varepsilon_F$ (atomic limit). By performing the Schrieffer-Wolff transformation, the Anderson model is mapped onto the Kondo model. The transformation projects out states where the impurity is occupied by 0 or 2 electrons. The Kondo Hamiltonian is given by

$$H = \sum_k \varepsilon_k c_k^\dagger c_k + \sum_{k,k'} J_{k,k'} \left(S^+ c_{k,\downarrow}^\dagger c_{k',\uparrow} + S^- c_{k,\uparrow}^\dagger c_{k',\downarrow} + S_z \left(c_{k,\uparrow}^\dagger c_{k',\uparrow} - c_{k,\downarrow}^\dagger c_{k',\downarrow} \right) \right) \tag{1.6}$$

[1]This will be one of the main differences from our model that is presented later. We will show that this assumption is useless in a finite system.

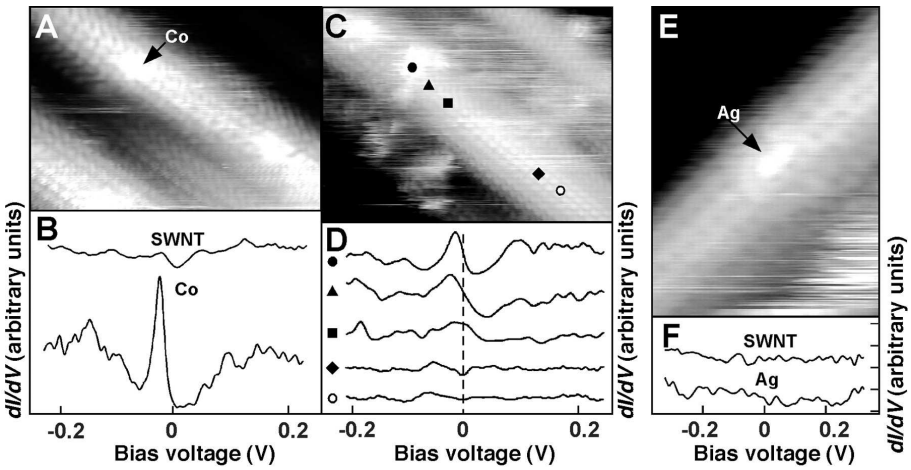

Figure 1.1: STM topographic images and spectroscopic measurements n small clusters situated on single-wall carbon nanotubes

where $\vec{S}$ denotes the spin operator on the impurity, and describes the spin-spin interaction of a the conduction band and the local moment. The spin coupling J is given by

$$J_{k,k'} = V_k^* V_{k'} \left(\frac{1}{U + \varepsilon_d - \varepsilon_k} + \frac{1}{\varepsilon_k - \varepsilon_d} \right). \tag{1.7}$$

One can easily see that the coupling is anti-ferromagnetic in the local moment regime.

1.2 Experiments

The goal of nanotechnology is to manipulate and control matter of the atomic scale. One of the main tools is the scanning tunneling microscope (STM). It allows the measurement of the energy spectrum at particular positions on a surface, move single atoms, and can image a surface with atomic resolution. The first application in Kondo physics was achieved in 1998 [13]: The STM has been used to image and move magnetic impurities on a metal surface, and to measure the Kondo resonance as a function of the applied voltage.
Besides putting magnetic atoms on metallic surfaces, it is also possible to study magnetic clusters on carbon nanotubes [9]. Single-walled carbon nanotubes are ideal systems for investigating properties of one-dimensional electronic systems. Lieber et al. used the STM to spatially resolve the electron density of states of cobalt cluster on metallic nanotubes at low temperature.

Spectroscopic measurements on or near these clusters exhibit a narrow peak that has been identified as a Kondo resonance. By reducing the size of the carbon nanotube and the cobalt cluster, it was possible to measure features characteristic of the bulk Kondo resonance, but also new features due to the finite size. The last point is a great motivation for our theoretical work, because we (as we will show later) see a lot of effects due to the finite size of the Kondo box.

1.3 The Green's Function and Spectral Densities

Green's functions [14, 15, 16] play a fundamental role in many-particle physics. On the one hand, they are defined as ground state averages of time-ordered products of operators, which can be calculated directly. On the other hand they may be easily related to experimental observables. The single-particle Green's function contains information about the ground state expectation value of any single-particle operator. Also the ground state energy itself and the whole excitation spectrum of the system may be extracted from the Green's function. Furthermore, the Green's function is directly related to correlation functions, which make it possible to compare theoretical predictions with experimental results. The causal single-particle Green's function at $T = 0$ is defined as

$$\begin{aligned} iG_{\alpha\beta}(xt, x't') &= \langle\psi_0|\ T[\Psi_{\alpha H}(x,t), \Psi^\dagger_{\beta H}(x't')]\ |\psi_0\rangle \\ &= \theta(t-t')\langle\psi_0|\Psi_{\alpha H}(x,t)\Psi^\dagger_{\beta H}(x't')|\psi_0\rangle \pm \\ &\quad \theta(t'-t)\langle\psi_0|\Psi^\dagger_{\beta H}(x',t')\Psi_{\alpha H}(xt)|\psi_0\rangle \end{aligned} \tag{1.8}$$

where ψ_0 is the ground state of the system, and

$$\Psi_{\alpha H}(t) = e^{iHt}\Psi_\alpha e^{-iHt} \tag{1.9}$$

($\hbar = 1$) is the field operator in Heisenberg representation. For simplicity, the indices α and β labeling the components of the field operators (two possible values for spin-$\frac{1}{2}$ particles) are dropped, because $G_{\alpha\beta}$ equals $G\delta_{\alpha\beta}$ in the absence of an external magnetic field and ferromagnetism. In the absence of any external field and in a homogeneous system, G is a function of the time difference $\tilde{t} = t - t'$ only instead of t and t', $G(t,t') = G(t-t')$. For fermionic systems (considered in this thesis) the time ordered product yields a minus

sign. The Green's function becomes

$$\begin{aligned} iG\left(xt,x't'\right) &= \theta\left(\tilde{t}\right)\langle\psi_0|e^{iHt}\Psi e^{-iHt}e^{iHt'}\Psi^\dagger e^{-iHt}|\psi_0\rangle \qquad (1.10)\\ &- \theta\left(-\tilde{t}\right)\langle\psi_0|e^{iHt'}\Psi^\dagger e^{-iHt'}e^{iHt}\Psi e^{-iHt}|\psi_0\rangle \\ iG\left(x,x',\tilde{t}\right) &= \theta\left(\tilde{t}\right)e^{iE_0\tilde{t}}\langle\psi_0|\Psi(x)e^{-iH\tilde{t}}\Psi^\dagger(x')|\psi_0\rangle \qquad (1.11)\\ &- \theta\left(-\tilde{t}\right)e^{-iE_0\tilde{t}}\langle\psi_0|\Psi^\dagger(x')e^{iH\tilde{t}}\Psi(x)|\psi_0\rangle \end{aligned}$$

Using

$$iG(\omega) = i\int_{-\infty}^{\infty}\mathrm{d}t\, e^{i\omega t}G(t) \qquad (1.12)$$

we obtain

$$\begin{aligned} iG(x,x',\omega) = \int_{-\infty}^{\infty} e^{i\omega\tilde{t}}\ &\Big[\theta\left(\tilde{t}\right)e^{iE_0\tilde{t}}\langle\psi_0|\Psi(x)e^{-iH\tilde{t}}\Psi^\dagger(x')|\psi_0\rangle - \qquad (1.13)\\ &\theta\left(-\tilde{t}\right)e^{-iE_0\tilde{t}}\langle\psi_0|\Psi^\dagger(x')e^{iH\tilde{t}}\Psi(x)|\psi_0\rangle\Big]\,\mathrm{d}\tilde{t}, \end{aligned}$$

and finally

$$\begin{aligned} iG(x,x',\omega) = \int_{-\infty}^{\infty}\ &\Big[\langle\psi_0|\Psi(x)\ \left(\theta\left(\tilde{t}\right)e^{iE_0\tilde{t}}e^{-iH\tilde{t}}e^{i\omega\tilde{t}}\ \right)\Psi^\dagger(x')|\psi_0\rangle - \qquad (1.14)\\ &\langle\psi_0|\Psi^\dagger(x')\ \left(\theta\left(-\tilde{t}\right)e^{-iE_0\tilde{t}}e^{iH\tilde{t}}e^{i\omega\tilde{t}}\ \right)\Psi(x)|\psi_0\rangle\Big]\,\mathrm{d}\tilde{t}. \end{aligned}$$

Using the representation of the θ function and its inverse

$$\pm e^{i\epsilon t}\theta(\pm t) = \frac{1}{2\pi}\int_{-\infty}^{\infty}\mathrm{d}\omega\frac{ie^{i\omega t}}{\omega-\epsilon\pm i\eta} \qquad (1.15)$$

$$\int_{-\infty}^{\infty}\mathrm{d}t\, e^{i\omega t}e^{-i\epsilon t}\theta(\pm t) = \pm\frac{i}{\omega-\epsilon\pm i\eta}, \qquad (1.16)$$

the Green's function can be written as

$$\begin{aligned} G(x,x',\omega) &= \langle\psi_0|\Psi(x)\frac{1}{\omega-(H-E_0)+i\eta}\Psi^\dagger(x')|\psi_0\rangle + \qquad (1.17)\\ &\langle\psi_0|\Psi^\dagger(x')\frac{1}{\omega+(H-E_0)-i\eta}\Psi(x)|\psi_0\rangle. \end{aligned}$$

Introducing a complete set of basis states, the Green's function becomes

$$\begin{aligned} G(x,x',\omega) &= \sum_n\langle\psi_0|\Psi(x)|\psi_n\rangle\frac{1}{\omega-(E_n-E_0)+i\eta}\langle\psi_n|\Psi^\dagger(x')|\psi_0\rangle + \\ &\langle\psi_0|\Psi^\dagger(x')|\psi_n\rangle\frac{1}{\omega+(E_n-E_0)-i\eta}\langle\psi_n|\Psi(x)|\psi_0\rangle \qquad (1.18) \end{aligned}$$

and for $x = x'$

$$G(x,\omega) = \sum_n |\langle\psi_0|\Psi(x)|\psi_n\rangle|^2 \left(\frac{1}{\omega - (E_n - E_0) + i\eta} + \frac{1}{\omega + (E_n - E_0) - i\eta}\right). \tag{1.19}$$

As mentioned above, the Green's function is related to the spectral density or correlation function, which can be measured experimentally by NMR, neutron scattering, photo emission etc. A correlation function is defined by

$$C_A(x, t - t') = \langle\psi_0|A^\dagger(x,t)A(x,t')|\psi_0\rangle, \tag{1.20}$$

where $A(x,t)$ again is a Heisenberg operator and $|\psi_0\rangle$ is the ground state. Again using that

$$A(x,t) = e^{iHt}A(x)e^{-iHt} \tag{1.21}$$

one gets

$$C_A(x, t - t') = \langle\psi_0|e^{iHt'}A^\dagger(x)e^{-iHt'}e^{iHt}A(x)e^{-iHt}|\psi_0\rangle \tag{1.22}$$

After inserting an identity operator and performing a Fourier transformation, this becomes

$$C_A(x,\omega) = \int e^{i\omega\tilde{t}} \sum_\alpha e^{i(E_\alpha - E_0)\tilde{t}} |\langle\alpha|A(x)|\psi_0\rangle|^2 \tag{1.23}$$

$$= \sum_\alpha |\langle\alpha|A(x)|\psi_0\rangle|^2 \delta(\omega - (E_\alpha - E_0)). \tag{1.24}$$

The imaginary part of the *on-site* Green's function is

$$\mathrm{Im}[G(x,\omega)] = \mathrm{Im}\left[\sum_n |\langle\psi_0|\Psi(x)|\psi_n\rangle|^2 \left(\frac{1}{\omega - (E_n - E_0) + i\eta} + \frac{1}{\omega + (E_n - E_0) - i\eta}\right)\right]. \tag{1.25, 1.26}$$

We use the relation

$$\frac{1}{x + i\eta} = P\left[\frac{1}{x}\right] - i\pi\delta(x), \tag{1.27}$$

where P denotes the principal part. In the case of $x + i\eta = \omega \mp (E_n - E_0) \pm i\eta$, this yields

$$\mathrm{Im}[G(x,\omega)] = \sum_n |\langle\psi_0|\Psi(x)|\psi_n\rangle|^2 \left\{P\left[\frac{1}{\omega - (E_n - E_0) + i\eta}\right] - i\pi\delta(\omega - (E_n - E_0)) + P\left[\frac{1}{\omega + (E_n - E_0) - i\eta}\right] + i\pi\delta(\omega + (E_n - E_0))\right\}$$

which can be simplified to

$$\mathrm{Im}[G(x,\omega) = \mp i\pi \sum_n |\langle\psi_0|\Psi(x)|\psi_n\rangle|^2(\delta(\omega - (E_n - E_0)) + \delta(\omega + (E_n - E_0))$$

and finally,

$$C(x,\omega) = -\frac{1}{\pi}\mathrm{Im}G(x,\omega)\,, \tag{1.28}$$

where G is the Green's function of the operator A.

1.3.1 The Green's Function for a Finite Lattice

Considering a finite lattice with n sites and N particles, the Green's function is given by

$$\begin{aligned} G(i,j,\omega) &= \langle\psi_0|c_i\frac{1}{\omega - (H - E_0) + i\eta}c_j^\dagger|\psi_0\rangle + \\ &\quad \langle\psi_0|c_j^\dagger\frac{1}{\omega + (H - E_0) - i\eta}c_i|\psi_0\rangle \end{aligned} \tag{1.29}$$

with the ground state $|\psi_0\rangle$ and c_i is the annihilation operator on site i. Inserting a complete set $|\alpha\rangle$ (for the Hamiltonian with $N+1$ particles) and $|\beta\rangle$ (for the Hamiltonian with $N-1$ particles) of eigenstates of H,

$$H|\alpha\rangle = E_\alpha|\alpha\rangle \tag{1.30}$$

$$H|\beta\rangle = E_\beta|\beta\rangle \tag{1.31}$$

with $c_i^\dagger|\psi_0\rangle = |i^+\rangle$ and $c_i|\psi_0\rangle = |i^-\rangle$, one gets

$$\begin{aligned} G(i,j,\omega) &= \sum_{\alpha,\alpha'}\langle i^+|\alpha\rangle\langle\alpha|\frac{1}{\omega - (H - E_0) + i\eta}|\alpha'\rangle\langle\alpha'|j^+\rangle + \\ &\quad \sum_{\beta,\beta'}\langle j^-|\beta\rangle\langle\beta|\frac{1}{\omega + (H - E_0) - i\eta}|\beta'\rangle\langle\beta'|i^-\rangle \end{aligned} \tag{1.32}$$

$$\begin{aligned} &= \sum_{\alpha,\alpha'}\langle i^+|\alpha\rangle\frac{\delta_{\alpha,\alpha'}}{\omega - (E_\alpha - E_0) + i\eta}\langle\alpha'|j^+\rangle + \\ &\quad \sum_{\beta,\beta'}\langle j^-|\beta\rangle\frac{\delta_{\beta,\beta'}}{\omega + (E_\beta - E_0) - i\eta}\langle\beta'|i^-\rangle \end{aligned} \tag{1.33}$$

$$\begin{aligned} &= \sum_\alpha \frac{\langle i^+|\alpha\rangle\langle\alpha|j^+\rangle}{\omega - (E_\alpha - E_0) + i\eta} + \\ &\quad \sum_\beta \frac{\langle j^-|\beta\rangle\langle\beta|i^-\rangle}{\omega + (E_\beta - E_0) - i\eta} \end{aligned} \tag{1.34}$$

The *on-site* Green's function is then given by

$$G(i,\omega) = \sum_{\alpha} \frac{|\langle i^{+}|\alpha\rangle|^2}{\omega - (E_\alpha - E_0) + i\eta} + \sum_{\beta} \frac{|\langle i^{-}|\beta\rangle|^2}{\omega + (E_\beta - E_0) - i\eta} \tag{1.35}$$

To sum up, one has to the following to calculate the spectral density for a finite lattice:

1. calculate the ground state $|\psi_0\rangle$ for the N-particle Hamiltonian
2. calculate $|i\rangle = c_i^{\dagger}|\psi_0\rangle$
3. diagonalize the $(N+1)$-particle Hamiltonian to get the eigenstates $|\alpha\rangle$ and the eigenvalues E_α
4. calculate the weights $w(\alpha) = |\langle i|\alpha\rangle|^2$
5. It is common to visualize each peak with a Gaussian, thus the right-hand side of the spectrum is then given by

$$A_r(\omega) = \sum_{\alpha} w(\alpha) \frac{1}{\sqrt{2\pi\sigma^2}} \exp\left(-\frac{\left(\omega - \left(E_\alpha - E_0^N\right)\right)^2}{2\sigma^2} \right). \tag{1.36}$$

The left part of the spectrum is obtained by applying the annihilation operator on $|\psi_0\rangle$, so that $|i\rangle = c_i|\psi_0\rangle$. Then, of course, it is the $(N-1)$-particle Hamiltonian which must be diagonalized. The weights are calculated in the same way, and the left-hand side is given by

$$A_l(\omega) = \sum_{\alpha} w(\alpha) \frac{1}{\sqrt{2\pi\sigma^2}} \exp\left(-\frac{\left(\omega + \left(E_\alpha - E_0^N\right)\right)^2}{2\sigma^2} \right). \tag{1.37}$$

Chapter 2

Numerical Methods

We will present various numerical methods in this chapter. We start with the *exact diagonalization*, a method that is limited to small systems, and continue with the *Lanczos* method, which makes it possible to treat Hubbard systems of up to about lattice sites. We then briefly describe the numerical *Bethe Ansatz* for a Hubbard chain with open boundary conditions, because it is used to compare ground state energies with non-exact methods. After the description of the *numerical renormalization-group* (NRG), we will present the main part of this chapter: The *density-matrix renormalization-group* (DMRG).

2.1 Exact Diagonalization

The numerical method of *exact diagonalization* is a method limited to small systems, that is, systems with a small basis of the Hilbert space. The corresponding Hamiltonian can be diagonalized exactly without any approximations except for numerical errors. The full spectrum of eigenstates can then be used to calculate dynamical properties, correlation functions etc. If the system is built up of single sites with a basis of b states per site, the Hilbert space grows exponentially. Therefore, the basis of a system of N_s sites contains b^{N_s} states. A computer with 1GB = 2^{30}byte `RAM` can be used to diagonalize a matrix of 2^{27} doubles (size of double = 8byte). With $b = 4$ (e.g. Hubbard Model), the maximum number of sites in the system is $N_s \leq 7$. This can be reduced by exploiting symmetries. As an example, the Hubbard Hamiltonian conserves particle number p and the z-component of the total spin, S_z^{total}. The dimension of the Hilbert space then equals

$$\left(\begin{array}{c} N_s \\ p_\uparrow \end{array} \right) \cdot \left(\begin{array}{c} N_s \\ p_\downarrow \end{array} \right), \tag{2.1}$$

with $p_\uparrow$ ($p_\downarrow$) being the number of particles with spin up (spin down). One way to treat bigger systems are iterative methods [17] where the Hamiltonian is not needed explicitly, but *only* the product of the Hamiltonian and a wave function, $H|\psi\rangle$, is needed. The price one has to pay is that most often not the full spectrum can be calculated to a sufficient degree of accuracy. If one is only interested in the eigenstates with the lowest lying eigenvalues, the Lanczos algorithm offers a technique to calculate them.

2.1.1 Lanczos method

The Lanczos method [18, 19] is applicable to large, sparse, and symmetric matrices. The algorithm tridiagonalizes a matrix by projecting it onto a Krylov subspace, that is

$$\mathcal{K}_m(H, v) = \text{span}\{v, Hv, H^2v, \ldots, H^{m-1}v\}. \tag{2.2}$$

One advantage is that the extremal eigenvalues are approximated very well a long time before the tridiagonalization is complete [20, 21]. Using the recursion equation

$$|f_{n+1}\rangle = H|f_n\rangle - a_n|f_n\rangle - b_n|f_{n-1}\rangle \tag{2.3}$$

where $|f_0\rangle$ is a random start vector and

$$a_n = \frac{\langle f_n|H|f_n\rangle}{\langle f_n|f_n\rangle}, \tag{2.4}$$

$$b_n = \frac{\||f_n\rangle\|_2}{\||f_{n-1}\rangle\|_2}, b_0 = 0, \tag{2.5}$$

one obtains

$$H = \begin{pmatrix} a_0 & b_1 & & 0 \\ b_1 & a_2 & \ddots & \\ & \ddots & \ddots & b_n \\ 0 & & b_n & a_n \end{pmatrix}. \tag{2.6}$$

This tridiagonal matrix can be diagonalized easily and fast by standard routines (e.g. from `LAPACK`) to obtain the eigenvalues and eigenvectors.
The Lanczos algorithm can also be used to calculate spectral densities

$$\begin{aligned} A(t-t') &= \langle\psi_0|O(t)O^\dagger(t')|\psi_0\rangle \\ &= \langle\psi_0|e^{iHt}Oe^{-iHt}e^{iHt'}O^\dagger e^{-iHt'}|\psi_0\rangle \\ &= e^{-iE_0(t-t')}\langle\psi_0|Oe^{-iH(t-t')}O^\dagger|\psi_0\rangle \end{aligned} \tag{2.7}$$

in the following way [22]: First, one calculates the ground state ψ_0 of the system, and then starts the Lanczos procedure with the starting vector

$$|f_0\rangle = \frac{O|\psi_0\rangle}{\sqrt{\langle\psi_0|O^\dagger O|\psi_0\rangle}} \tag{2.8}$$

for a reason that will become obvious soon. Then, the tridiagonal matrix is diagonalized to obtain the eigenvectors ϕ_n of the system. This nearly complete set is inserted into equation (2.7) and gives

$$A(t-t') \approx \sum_{\alpha,\beta} e^{-iE_0(t-t')}\langle\psi_0|O(t)^\dagger|\phi_\alpha\rangle\langle\phi_\alpha|e^{iH(t-t')}|\phi_\beta\rangle\langle\phi_\beta|O(t')|\psi_0\rangle, \tag{2.9}$$

and via a Fourier transformation one obtains the well known equation

$$A(\omega) = \sum_\alpha |\langle\phi_\alpha|O|\psi_0\rangle|^2\delta(\omega - (E_\alpha - E_0)). \tag{2.10}$$

The eigenvectors $|\phi_\alpha\rangle$ can be expanded in terms of the Lanczos vectors $|f_\alpha\rangle$ we obtained during the tridiagonalization, with $|f_0\rangle = \frac{O|\psi_0\rangle}{\sqrt{\langle\psi_0|O^\dagger O|\psi_0\rangle}}$:

$$|\phi_\alpha\rangle = \sum_m c_m^\alpha |f_m\rangle \tag{2.11}$$

Now, the term $|\langle\phi_\alpha|O|\psi_0\rangle|^2$ can be rewritten as follows:

$$\begin{aligned} |\langle\phi_\alpha|O|\psi_0\rangle|^2 &= |\langle\phi_\alpha|\sqrt{\langle\psi_0|O^\dagger O|\psi_0\rangle}|f_0\rangle|^2 \\ &= |\sum_m (c_m^\alpha)^* \langle f_m|\sqrt{\langle\psi_0|O^\dagger|\psi_0\rangle} f_0\rangle|^2 \end{aligned} \tag{2.12}$$

and since the $|f_m\rangle$ are orthonormal, this can be simplified to

$$|\langle\phi_\alpha|O|\psi_0\rangle|^2 = |c_0^\alpha|^2 \langle\psi_0|O^\dagger O|\psi_0\rangle. \tag{2.13}$$

Therefore, the weight of the peaks in $A(\omega)$ corresponding to the eigenvalue E_α is identified with the 0^{th} entry of the α^{th} eigenvector ϕ_α in the expansion in terms of the $|f_m\rangle$. For visual representation it is common practice to draw a Gaussian or Lorentzian curve with a fixed broadening and the given weight w_i at the matching position E_i of the peak. For the Gaussian, the spectral density can be written as

$$A(\omega) = \sum_i \frac{w_i}{\sqrt{2\pi}\sigma} \exp - \frac{(\omega - E_i)^2}{2\sigma^2}$$

and the Lorentz curve is given by

$$A(\omega) = \sum_i \frac{1}{\pi} \frac{w_i \sigma}{(w_i - \omega)^2 + \sigma^2}$$

One major source of errors is the identity in (2.9), since it is not complete. Providing only accurate results for low excitations near the ground state is a shortcoming of this method.

2.2 Bethe Ansatz

The Bethe Ansatz [23] is an exact method for the calculation of eigenvalues and eigenvectors of a limited class of quantum many-body systems. Although the eigenvalues and eigenvectors for a finite system may be obtained from numerical diagonalization, the Bethe Ansatz is not limited in the system size. In addition, it has other advantages: All eigenstates are characterized by a set of quantum numbers which can be used to distinguish them according to specific physical properties, and the eigenvalues can be calculated in the thermodynamic limit. It was first used to calculate the one-dimensional Heisenberg model, but has been generalized to treat other one-dimensional systems. We will use some results from the Bethe Ansatz for a 1D Hubbard model as reference values. Thus, we will sketch the Bethe Ansatz equations for the 1D Hubbard model for open boundary conditions [24, 25, 26]. The energy of a 1D Hubbard chain with L sites, N electrons and M electrons with $\sigma = -1/2$ can be written as

$$E = N\mu - 2\sum_{j=1}^{N} \cos(k_j)$$

The momenta k_j and spin rapidities v_m for open boundary conditions are given by

$$\exp(2k_j(L+1)) = \prod_{m=1}^{M} \frac{(\sin(k_j) + iU/4)(\sin(k_j) + v_m + iU/4)}{(\sin(k_j) - v_m - iU/4)(\sin(k_j) + v_m - iU/4)}$$

and

$$\prod_{n \neq m}^{M} \frac{(v_m - v_n + iU/2)(v_m + v_n + iU/2)}{(v_m - v_n - iU/2)(v_m + v_n - iU/2)} = \tag{2.14}$$

$$\prod_{j=1}^{N} \frac{(v_m - \sin(k_j) + iU/4)(v_m + \sin(k_j) + iU/4)}{(v_m - \sin(k_j) - iU/4)(v_m + \sin(k_j) - iU/4)}. \tag{2.15}$$

By building the logarithm of these equations one gets

$$\begin{aligned} 0 = & - 2(L+1)k_j + 2\pi I_j \\ & - \sum_{m=1}^{M} \left(2\arctan\left(\frac{\sin(k_j) - v_m}{U/4}\right) + 2\arctan\left(\frac{\sin(k_j) + v_m}{U/4}\right)\right) \quad (2.16) \\ 0 = & \quad 2\pi J_m - \sum_{j=1}^{N} \left(2\arctan\left(\frac{v_m - \sin(k_j)}{U/4}\right) + 2\arctan\left(\frac{v_m + \sin(k_j)}{U/4}\right)\right) \\ & + \sum_{n\neq m}^{M} \left(2\arctan\left(\frac{v_m - v_n}{U/2}\right) + 2\arctan\left(\frac{v_m + v_n}{U/2}\right)\right) \quad (2.17) \end{aligned}$$

where $I_j, J_m \in \mathbf{Z}$. The set of equations can be easily solved by Newton iteration.

2.3 Numerical Renormalization Group

The first ideas of Renormalization Groups [27] in condensed matter theory occurred in the 1960s. It was Kenneth Wilson who transfered these methods from particle physics to condensed matter physics in order to solve the Kondo Problem [28]. The idea of the NRG is to iteratively integrate out higher energy states in order to get the spectrum for the Hamiltonian H_N for each step N, which corresponds to a different energy scale. The procedure in the case of the Single Impurity Anderson Model (SIAM) is briefly described:
The Hamiltonian is given by

$$\begin{aligned} H = & \sum_{k,\sigma} \varepsilon(k) c^{\dagger}_{k\sigma} c_{k\sigma} + V \sum_{\sigma} \left(f^{\dagger}_{\sigma} c_{\sigma} + c^{\dagger}_{\sigma} f_{\sigma} \right) \\ & + \varepsilon_f \sum_{\sigma} n_{f,\sigma} + U n_{f,\uparrow} n_{f,\downarrow} \end{aligned}$$

where $c^{(\dagger)}_{k,\sigma}$ and $f^{(\dagger)}_{k,\sigma}$ denote creation and annihilation operators on the conduction band and on the impurity, respectively. U is the Coulomb repulsion on the impurity, V is the hopping amplitude between impurity and chain, and ε_d denotes the chemical potential on the impurity. The first step is the logarithmic discretization of the conduction band into energy scales with

$$D\Lambda^{-(n+1)} < |\varepsilon_f - \varepsilon_F| < D\Lambda^{-n} \quad n = 1, 2 \ldots .$$

D is the width of the conduction band, and Λ is the discretization. The second step consists of the mapping of the model onto a semi-infinite chain

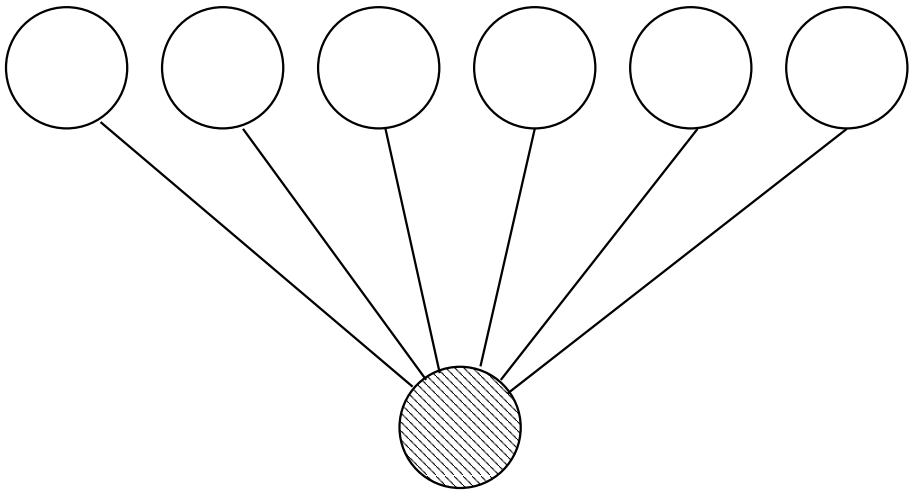

Figure 2.1: The impurity (patterned circle) is connected to all sites of the conduction band

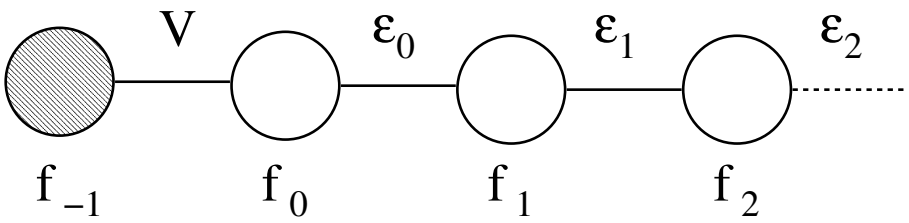

Figure 2.2: After the NRG transformation, one obtains a semi-infinite linear chain with the impurity at the first site

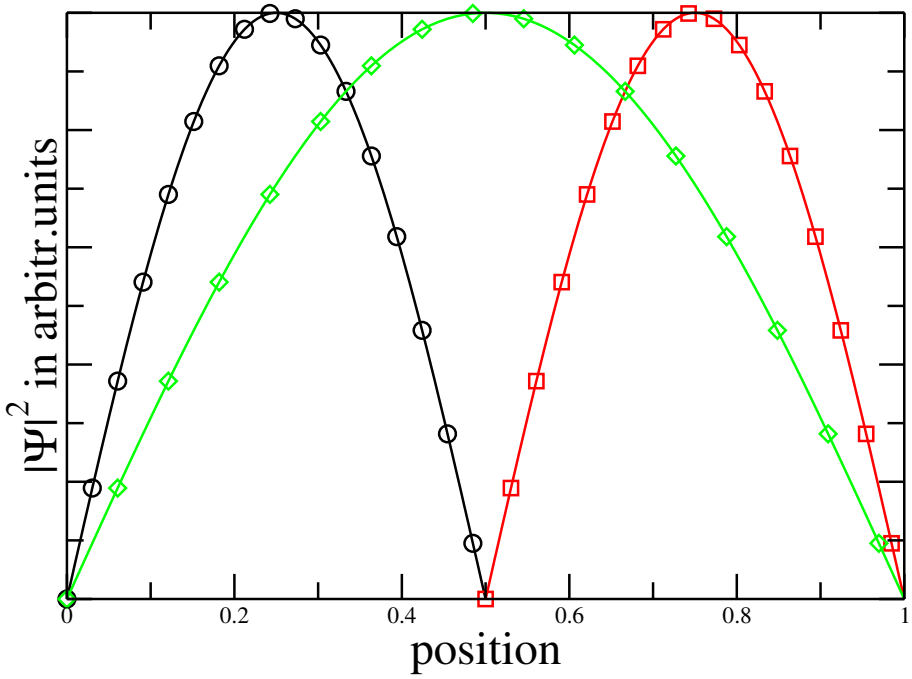

Figure 2.3: sketch of ground state wave functions of small tight-binding chains

which is depicted in Fig. 2.1 and Fig. 2.2. The new Hamiltonian is then given by

$$\begin{aligned} H &= \sum_{\sigma} \varepsilon_f f^{\dagger}_{-1,\sigma} f_{-1,\sigma} + U f^{\dagger}_{-1,\uparrow} f_{-1,\uparrow} f^{\dagger}_{-1,\downarrow} f_{-1\downarrow} \\ &\quad + \sum_{\sigma n=1}^{\infty} \varepsilon_n \left(f^{\dagger}_{n,\sigma} f_{n+1,\sigma} + f^{\dagger}_{n+1,\sigma} f_{n,\sigma} \right) \end{aligned}$$

Now, $f^{(\dagger)}_{-1,\sigma}$ acts on the impurity states and $f^{(\dagger)}_{n,\sigma}$ with $n = 0, 1, 2, \ldots$ on states of the conduction band. Due to the logarithmic discretization, the hopping matrix elements decrease exponentially. By going along the chain, the system evolves from high energy states to smaller energies. In each step of the iteration, a new site of the conduction band is added to the system, the new Hamiltonian is built and diagonalized, and the basis is truncated such that the m eigenstates with the smallest eigenvalues are kept. Unfortunately, this method cannot transferred to real-space problems, e.g. a linear Hubbard model, where sites do not represent energy shells, but lattice sites. Since the hopping matrix elements do not decrease exponentially and the conduction band is not discretized logarithmically, the method fails after a few steps. The problem is the choice of states that determine the new basis. We consider

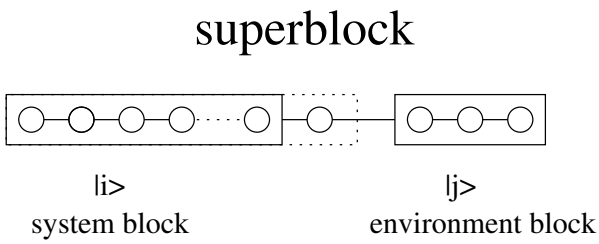

Figure 2.4: a new superblock is built by adding a single site to the system block and joining with an environment block

the wave function of the ground state of a small tight-binding chain: In Fig. 2.3 we have plotted three wave function of two small chains and one chain built up of the two chains. It is obvious that the two ground state wave functions of the small chains are not a good basis for the ground state wave function of the big chain: each wave function of the small chain has a node in the middle of the big chain, where its ground state wave function has a maximum. Another RG with a different way to truncate the basis will be described in the next chapter.

2.4 The Density-Matrix Renormalization-Group

In this section we present the method that is used for almost all calculations in this thesis — the density-matrix renormalization-group (DMRG). We will start by summing up the characteristics of density matrices and show why it is best to choose the m largest eigenstates of the density matrix to be the truncated basis. We will then introduce the infinite and finite system algorithm, along with all technical issues like building a product basis or performing a measurement. In the end, we show how the DMRG can be used to calculate dynamical properties.

2.4.1 The (Reduced) Density Matrix

The density operator contains all possible information about the state of the quantum system. Given that we know the density operator ρ for a system, we can use it to calculate the expectation value of any operator A of the system by

$$\langle A \rangle = \mathrm{Tr}(A\rho),$$

where Tr denotes the trace. The density operator is normalized such that $\mathrm{Tr}(\rho) = 1$. The density matrix is hermitean and can be diagonalized to

yield the eigenstates u_α with the corresponding eigenvalues $w_\alpha \geq 0$. Since $\mathrm{Tr}(\rho) = 1$, $\sum_\alpha w_\alpha = 1$. By writing A and ρ in the eigenbasis of ρ, one gets

$$\langle A \rangle = \sum_\alpha w_\alpha \langle u^\alpha | A | u^\alpha \rangle.$$

Supposing one has to discard basis states from the system, it is obvious that no error in $\langle A \rangle$ would occur if these states are eigenstates u^α of ρ with $w_\alpha = 0$. Now we consider a system coupled to an environment. The full system consists of two blocks — the system block and the environment block — and is now called the superblock (Fig. 2.4). The basis of the superblock is a product of the basis states of the system block $|i\rangle$ and the basis states of the environment block $|j\rangle$. A wave function on the superblock can therefore be written as

$$|\Psi\rangle = \sum_{i,j} \Psi_{i,j} |i\rangle |j\rangle$$

The reduced density matrix for the system block is defined as

$$\rho_{i,i'} = \sum_j \Psi^*_{i,j} \Psi_{i',j}$$

The expectation value of an operator that acts only on the system block is given by

$$\langle A \rangle = \mathrm{Tr}(A\rho) = \sum_{i,i'} A_{i,i'} \rho_{i,i'} = \sum_\alpha w_\alpha \langle u^\alpha | A | u^\alpha \rangle$$

where again u^α are the eigenstates of ρ with eigenvalues w_α. If the basis of the system block has to be truncated, then the same arguments as above hold. We will show that not only the error in $\langle A \rangle$ is as small as possible by keeping the most probable states of the reduced density matrix, but also that a state $|\Psi\rangle$ is also represented in the best way possible. One wants to represent

$$|\psi\rangle = \sum_{i,j} \psi_{i,j} |i\rangle |j\rangle \tag{2.18}$$

in a truncated basis

$$|u^\alpha\rangle, \alpha = 1, \ldots, m \tag{2.19}$$

for the system block. Since $l = m \cdot n$ is the number of system basis states $|i\rangle$ (n is the basis size of a single site), and $l > m$, $|\psi\rangle$ cannot be represented exactly in the truncated basis and has to be expanded in terms of $|u^\alpha\rangle$ and $|j\rangle$, that is

$$|\psi\rangle \approx |\tilde{\psi}\rangle = \sum_{\alpha,j} a_{\alpha,j} |u^\alpha\rangle |j\rangle \tag{2.20}$$

Therefore, the task is to minimize

$$S = \left| |\psi\rangle - |\tilde{\psi}\rangle \right|^2 \tag{2.21}$$

varying over all $a_{\alpha,j}$ and $|u^\alpha\rangle$. Using $v_j^\beta := \langle j|v^\beta\rangle = N_\beta a_{\beta,j}$ with N_β chosen such that $\sum_j v_j^\alpha v_j^\beta = \delta_{\alpha,\beta}$, one gets

$$|\tilde{\psi}\rangle = \sum_\alpha a_\alpha |u^\alpha\rangle |v^\alpha\rangle \tag{2.22}$$

and, in matrix notation

$$S = \sum_{i,j} \left(\psi_{ij} - \sum_{\alpha=1}^{m} a_\alpha |u_i^\alpha\rangle |v_j^\alpha\rangle \right)^2 \to \min . \tag{2.23}$$

This problem is known from linear algebra. Its solution is produced by single value decomposition (SDV) of $|\psi\rangle$, i. e. $|\psi\rangle = UDV^T$, where U and D are $l \times l$ matrices and V is an $l \times J$ matrix ($j = 1, \ldots, J$, and $J \geq l$). U is orthonormal, V is column-orthogonal and D contains the singular values of $|\psi\rangle$. To minimize S, the parameters are chosen as follows: The m largest-magnitude diagonal elements of D are the a_α, and the corresponding columns of U and V are the u^α and v^α. The reduced density matrix is defined as

$$\rho_{ii'} = \sum_j \psi_{ij}\psi_{i'j} \tag{2.24}$$

$$= UD^2U^T \tag{2.25}$$

The eigenvalues of ρ are $w_\alpha = a_\alpha^2$ and the optimal states u^α are the eigenstates of ρ with the largest eigenvalue. Since $\sum_\alpha w_\alpha = 1$, the deviation of $P_m = \sum_\alpha^m w_\alpha$ from unity, i. e. the discarded weight of the density matrix eigenvalues, measures the accuracy of the truncation to m states. If Ψ is the ground state of the system, this shows that it is better to use the density matrix to determine the states kept instead of retaining the eigenstates with the lowest-lying eigenvalues as done in the NRG. Knowing how to reduce the basis of a system that is coupled to an environment in order to represent a given state of the full system leads to:

2.4.2 The Infinite System Algorithm

1. Start with a block with L sites and m states that can be solved numerically exactly. This is the first system block.

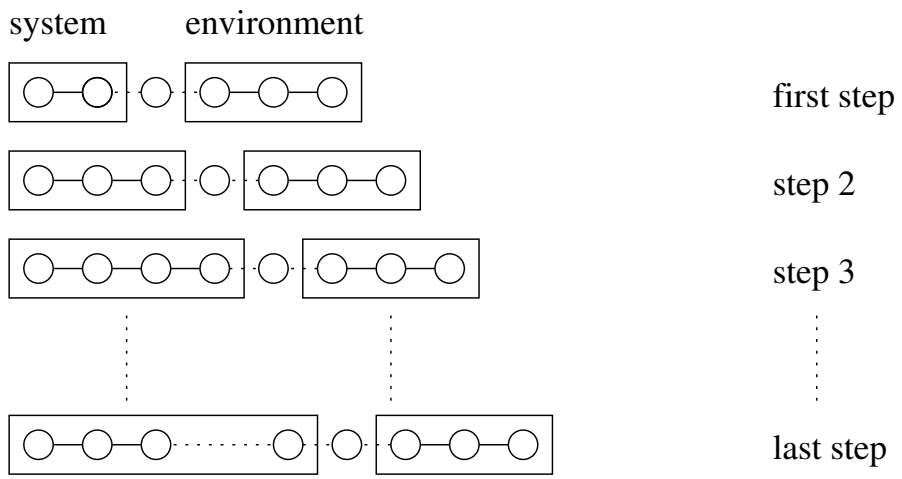

Figure 2.5: The infinite system algorithm

2. Add a single site with n states to the system block, yielding a new system block with $l = m \times n$ states.

3. Build a superblock, consisting of the system block and an environment block, a block of a few sites.

4. Calculate the ground state of the superblock using the Lanczos or Davidson algorithm. The ground state is chosen to be the *target state*. The *target state* does not have to be the ground state, and for some applications multiple target states are chosen. The *target state* is the state that is used to build the density matrix.

5. Calculate the reduced density matrix of the system block by evaluating the partial trace over the environment block. Diagonalize the density matrix.

6. The m eigenvectors of the density matrix with the highest lying eigenvalues are the new basis of the system block. Truncate the basis and transform the operators accordingly.

7. Go back to step 2 until the desired length is reached.

Using the infinite system algorithm, a system is built up iteratively with the basis truncated after each step in a way which is optimal to represent the states in the new basis. The problem is that it is optimal to represent the basis for the current size, not for the final size. That means, if the system

block has s sites and your environment has e sites, the operators on the system are truncated to optimally represent a system of $s+e$ sites. However, one is interested in a method to truncate the basis in a way that is optimal to represent the states of the *final* size. The solution to this problem is the *finite size algorithm*.

2.4.3 The Finite Size Algorithm

The environment is now chosen such that the superblock has a fixed size.

1. Use the infinite system algorithm to build up the system to the desired length L. Store all Hamiltonians and operators of the left block in each step. At the last step, the system block has l sites and the environment block has r sites, where $l+r = L$. The environment block is now called the right block, the system block the left block.

2. Add a single site to the right block, which then has $r' = r + 1$ sites. Add a single site to the left block with $l = L - r' - 1$ sites, and build a superblock of the two new blocks.

3. Carry out the steps 4–6 of the infinite system algorithm, interchanging the roles for left and right block (e.g. building the density matrix for the right block)

4. Rename $r = r'$. Go back to step 2 until $l = 2$. This is called the right to left sweep.

5. Add a single site to the left block, which now has $l' = l + 1$ sites. Add a single site to the right block with $r = L - l' - 1$ sites, and build a superblock out of the two new blocks.

6. Carry out the points 4–6 from the infinite system algorithm.

7. Rename $l = l'$. Go back to step 5 until $L - l' = 2$. This is called the left to right sweep.

8. Go back to point 2 until convergence is reached.

The algorithm is depicted in Fig. 2.6. What one actually does is sweeping from one end to the other (one can think of this like running a zipper), always putting two single sites between the two blocks, which gives enough new information to the system so that the ground state energy converges rapidly after just a few sweeps as can be seen in Fig. 2.8.

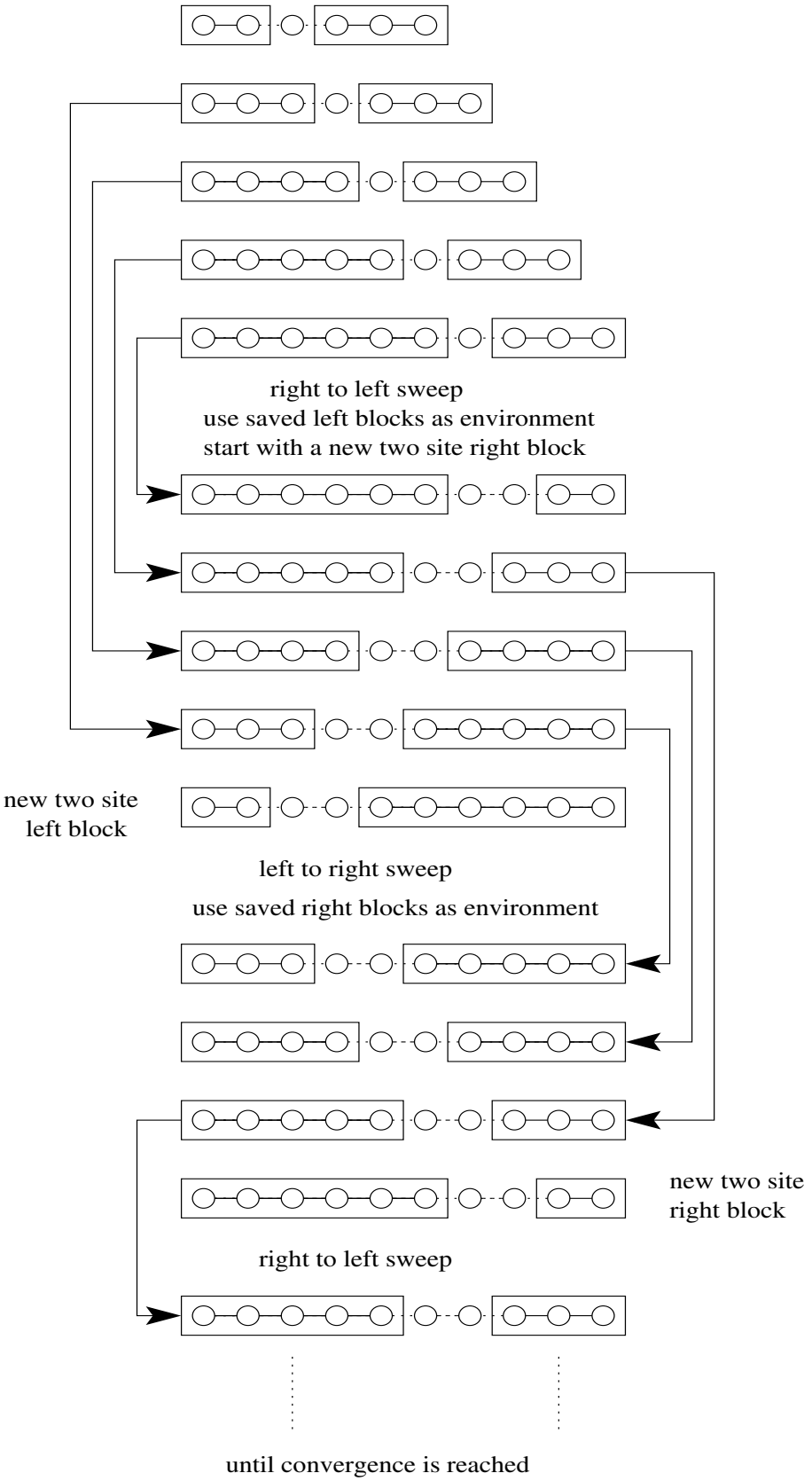

Figure 2.6: The finite size algorithm

2.4.4 Operators, Measurements, Wave Functions, Multiple Target States

We will describe how to handle operators, perform measurements of observables and how to get a good starting vector for the Lanczos algorithm.

Operators An operator that only acts on one block is just written in the basis of that specific block. The action of a block operator on the wave function of the superblock can therefore be written as (supposing that A acts only on the left block)

$$|\Phi\rangle = \sum_{i,j} \Phi_{i,j}|i\rangle|j\rangle = A\sum_{i,j} \Psi_{i,j}|i\rangle|j\rangle \tag{2.26}$$

with

$$\Phi_{i,j} = \sum_{i'} A_{i,i'}\Psi_{i',j}. \tag{2.27}$$

If operator B acts only on the right block, then

$$\Phi_{i,j} = \sum_{j'} B_{j,j'}\Psi_{i,j'} \tag{2.28}$$

Both operations can be written as matrix products, $A \cdot \Psi$ and $\Psi \cdot B^\top$.
The ground state of the superblock has to be calculated in each step. The Lanczos algorithm does not need to have the full matrix of the superblock Hamiltonian explicitly, but only has to perform a multiplication of the Hamiltonian and a wave function. The matrix representing the Hamiltonian in the case of the Hubbard Hamiltonian is given by

$$\begin{aligned} H_{ij,i'j'} &= H^l_{i,i'}\delta_{jj'} + H^r_{j,j'}\delta_{ii'} \\ &+ \sum_\sigma \left[c^\dagger_\sigma(L)\right]_{i,i'} \left[c_\sigma(L+1)\right]_{j,j'} + \left[c^\dagger_\sigma(L+1)\right]_{j,j'} \left[c_\sigma(L)\right]_{i,i'} \end{aligned}$$

where $c^{(\dagger)}_\sigma(L)$ is the operator on the rightmost site of the left block (site L) and $c^{(\dagger)}_\sigma(L+1)$ is the operator on the leftmost site of the right block (site $L+1$).
If a site is added to a block or two blocks are joined as new block, the new Hamiltonian and the operators connecting the new block to the rest of the superblock have to be built. Since operators from the left (right) block $O^l_{i,i'}$ ($O^r_{j,j'}$) act only on states from the left (right) block, the matrix elements of an operator of the new block equals

$$O_{ij,i'j'} = O^l_{i,i'}\delta_{jj'} + O^r_{j,j'}\delta_{ii'}$$

The basis of the current system block (either the left or right block, depending on the direction of the current sweep) has to be truncated in each step. The new basis is given by the m eigenstates u^α of the reduced density matrix with the lowest eigenvalues. These eigenstates can be written in columns in a transformation matrix $D_{\alpha,\beta} = u^\alpha_\beta$. An operator A of the system block is transformed to the new basis by

$$\tilde{A} = D^\top \cdot A \cdot D$$

$$\tilde{A}_{i,i'} = \sum_{a,c} D_{a,i} A_{a,c} D_{c,i'}.$$

The dimension of the matrices are given by (assuming that the size of the old basis is b):

$$(m \times m) = (b \times m)^\top (b \times b)(b \times m)$$

Measurements The DMRG can not only be used to calculate ground-state energies, but also to measure ground-state expectation values of operators, that is

$$\langle A \rangle = \langle \psi | A | \psi \rangle \tag{2.29}$$

with ψ being the ground state of the superblock. In order to do so, one must keep track of the operator A (or the components of A). Thus, at each DMRG step, A has to be transformed to the new basis corresponding to one single site being added to the system block. The operator A has to be truncated in the same way as the Hamiltonian and other operators. The expectation value is exact in the given basis, and, for an operator acting on the left block, looks like

$$\langle \psi | A | \psi \rangle = \sum_{i,i',j} \psi^*_{ij} A_{ii'} \psi_{i'j}. \tag{2.30}$$

To calculate correlation functions, e. g. $\langle \psi | AB | \psi \rangle$, it has to be taken into account whether the two operators act on the same block. If they do, the expectation value is *not* given by

$$\langle \psi | AB | \psi \rangle \neq \sum_{i,i',i'',j} \psi^*_{ij} A_{ii'} B_{i'i''} \psi_{i''j}, \tag{2.31}$$

because the sum over i' is not complete. In this case, you have to keep track of the product of the two operators, $C = AB$, and then calculate the expectation value in the way explained above. If the two operators act on different blocks, the calculation is easy and the expectation value is given by

$$\langle \psi | AB | \psi \rangle = \sum_{i,i',j,j'} \psi^*_{ij} A_{ii'} B_{jj'} \psi_{i'j'}. \tag{2.32}$$

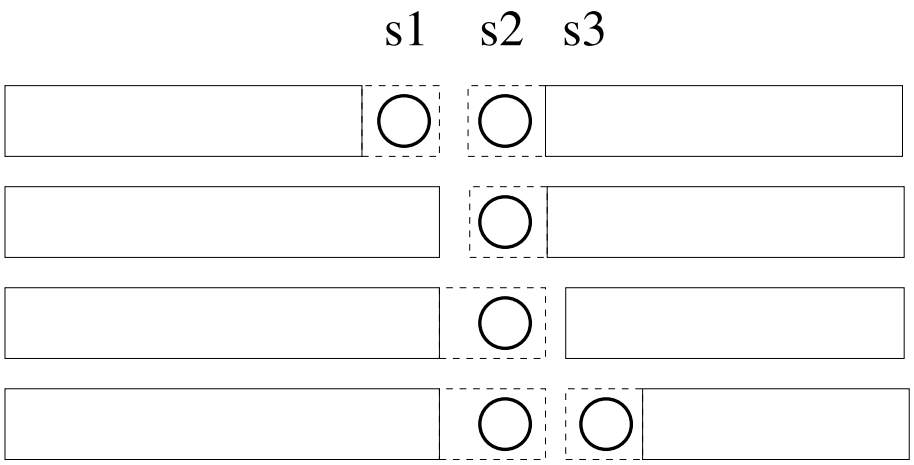

Figure 2.7: The transformation of the wave function

If one wants to measure the density on site i for each step, it is wrong to calculate $\langle\psi|c_i^\dagger c_i|\psi\rangle$. One has to build $n_i = c_i^\dagger c_i$ in an exact, non-truncated basis, and keep track of it.

Wave unction transformation As mentioned before, the Lanczos procedure can be sped up rapidly by starting with a vector which is nearly the ground state of the system. Since the ground state of the superblock has to be calculated in each step, it is a good idea to use the ground state of the previous step as starting vector of the Lanczos routine. This reduces the number of Lanczos steps from about 100 to 2—3 per DMRG step. We will just sketch the procedure to transform the old ground state to the new basis, because a detailed description can be found in [29]. A wave function can be truncated in a similar way as an operator. Let us assume that the system block is the left block and all operators have been truncated. The ground state of the superblock with the truncated left block is now given by

$$|\tilde{\Psi}\rangle = D_{s1}^\top |\Psi\rangle.$$

The next task is one of the most complicated in a DMRG program: one has to shift the states of site $s2$ from the product basis of the right block to the new product basis of the new left block. The new wave function is now the (exact) ground state of the new superblock, with $s2$ belonging to the left block. The final step is an *inverse truncation* of the right block. The

transformation matrix that was used to truncate the right block at position $s3$ had to been stored in the previous sweep and is now used to *blow up* the wave function regarding the states of the right block: $|\Psi'\rangle = |\tilde{\Psi}\rangle D_{s3}$. The last step is not an exact transformation, because D is not unitary, and $D^\top \cdot D \approx 1$. The transformed wave function is just a good approximation for the exact wave function of the new DMRG step. The procedure is depicted in Fig. 2.7.

Multiple target states The DMRG algorithm can also be performed with multiple target states. This is done by separately building the density matrix for each state and then adding up the matrices, each weighted with a factor, so the final matrix has the properties of a density matrix.

$$\rho = \sum_\alpha w[\alpha]\rho_\alpha \tag{2.33}$$

with

$$\rho_{i,i',\alpha} = \sum_j \psi_{i,j,\alpha}\psi_{i',j,\alpha} \tag{2.34}$$

and

$$\sum_\alpha w[\alpha] = 1 \tag{2.35}$$

This can be useful for applying the DMRG to a system which is not at zero temperature. In this case, the weights $w[\alpha]$ are Boltzmann weights $w[\alpha] = \exp(\frac{-E_\alpha}{k_B T})$ and the state $\psi_{i,j,\alpha}$ is the state with energy E_α. Multiple target states are usually used when one calculates dynamical properties of the system. We will describe the different choice of target states later.

2.4.5 Implementation

The program is written in `C++` [30]. It is very important to exploit symmetries of the system. Operators usually change the quantum numbers of a given state by a fixed value. Assuming we use the number of particles N and the z-component of the spin S_z as quantum numbers of the system, $c^\dagger_\uparrow$ changes the quantum numbers from N, S_z to $N+1, S_z+1/2$. Each operator connects states from one quantum number to another quantum number. The matrices for operators in a basis of all quantum numbers are usually sparse and are not stored completely. But due to the fixed change of quantum numbers of a state, the matrix has block form, and only the blocks have to be stored. As an example, we look at the creation operator $c^\dagger_\uparrow$ for a single site of a Hubbard chain. The site has four states: no particle ($|-\rangle$), one particle (with spin up or down, $|\uparrow\rangle$, $|\downarrow\rangle$) and double occupied ($|\uparrow\downarrow\rangle$). The full matrix for $c^\dagger_\uparrow$

would therefore be a (4×4) matrix with 16 entries. But only 2 out of the 16 elements are non-zero (from $|-\rangle$ to $|\uparrow\rangle$, and $|\downarrow\rangle$ to $|\uparrow\downarrow\rangle$). Instead of storing one (4×4) matrix, two (1×1) sub matrices are stored. An operator is therefore represented by a set (usually a `std::vector`) of dense matrices. Matrices are allocated in Fortran scheme, so `Lapack` and `blas` routines are used wherever possible. The numerical representation of a wave function is similar. Usually, one thinks of a wave function as a vector. But due to the product basis of the two blocks, the wave function is stored as a matrix — or a set of matrices. Even if the total number of particles and spin is fixed, the number of particles on the left and right block is not constant.

Numerical Testing After the program is written, one has to check whether it is implemented correctly. This can be achieved by applying the method to a (numerically) exactly solvable problem, e.g. the one-dimensional tight-binding chain (non-interacting system), a 1D Hubbard or Heisenberg chain (Bethe Ansatz). We compare the ground state energy from our DMRG calculation of a one-dimensional Hubbard chain at half filling, $U = 4t$, with the exact solution obtained from the Bethe Ansatz equations [24, 25].

For the calculation of the finite-size chain, one can see that the ground state energy converges very fast. We only keep a small number of states for the warm-up sweep ($m = 100$) and then increase m for each iteration by 100. When $m = 1000$ at sweep 10, we do another 5 sweeps with constant m. But even if the the number of states m is kept constant, one can see small wiggles in the ground state energy plotted versus the position in the superblock. This is the effect of the different truncation errors. If we consider a homogeneous system (as the 1D Hubbard chain in the example), the truncation error and the ground state energy reach their respective minimum in the middle of the system, when both blocks are of about the same size. The DMRG is a variational method and the ground state energy is approached from above, $E^0_{\mathrm{DMRG}} \geq E^0_{\mathrm{exact}}$. Therefore, measurements are best carried out at the position, where E_0 reaches its minimum — this does not have to be the middle of the chain, and is somewhere near the impurity for the SIAM. What has to be done to measure the local density on each site? It is tempting to measure n_i for each site when site i is connected to the system block. The operator can be built on the single site and then be transformed in the product basis. Unfortunately, this results in a larger error than the following procedure: After the convergence of the system, the position of minimum truncation is known. Next, several sweeps to that position are performed, where in each sweep, a set of several n_i is kept track of. When the final position is reached, all expectation values are measured, and another sweep

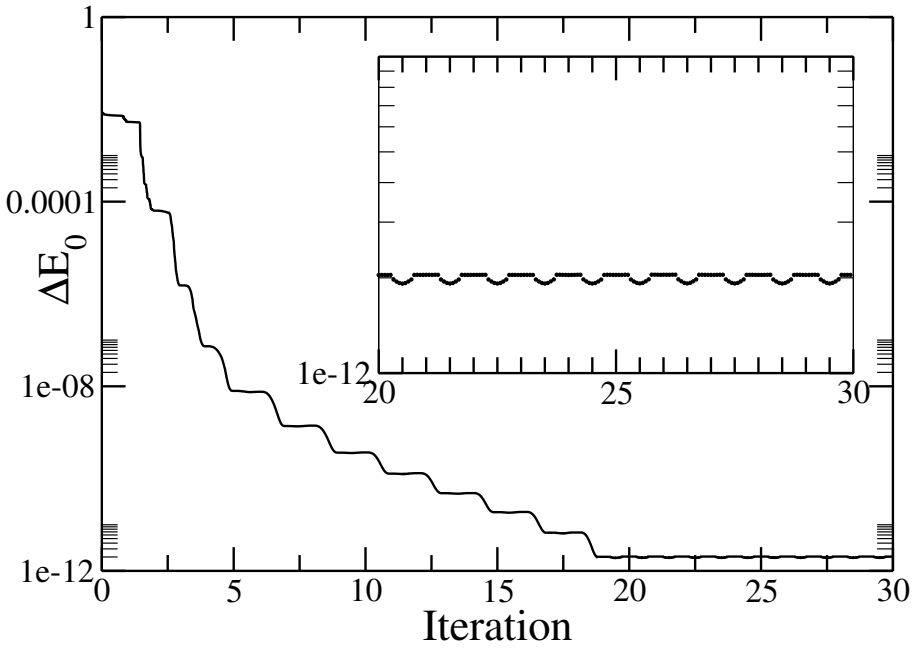

Figure 2.8: ΔE_0 for each step for a 1D Hubbard chain with length $L = 100$, filling $\langle n \rangle = 1$ and $U = 4t$. The number of states kept, m, is increased by 100 within each sweep, starting from $m = 100$ up to $m = 1000$ in sweep 10. 15 full sweeps — or 30 half sweeps (from one end of the chain to the other end) — are performed. The inset shows the sweeps 10 to 15, where is $m = 1000$ is kept constant. The error in the ground state energy gets smaller when both blocks have about the same size.

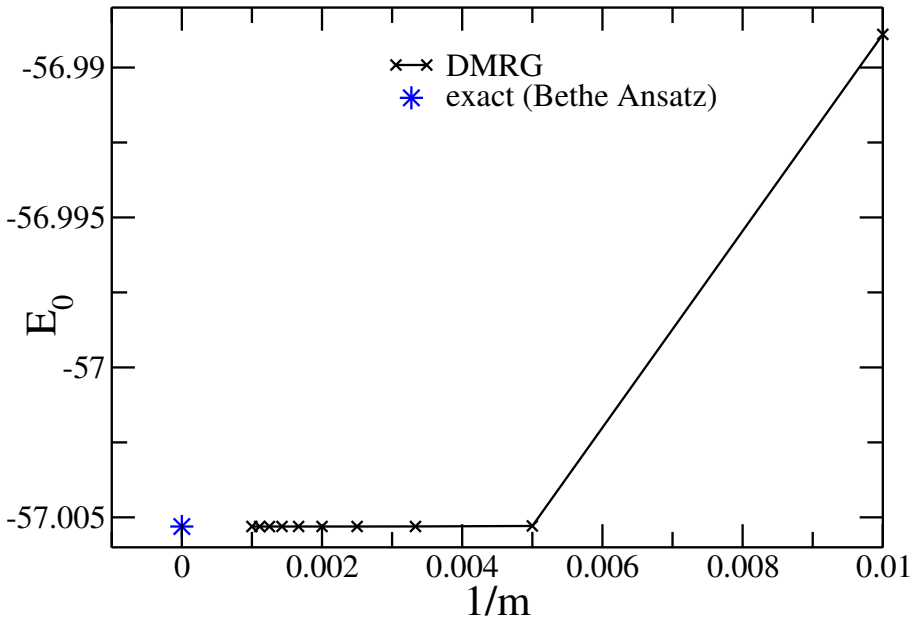

Figure 2.9: E_0 for each sweep with a different number of states retained m for a 1D Hubbard chain with length $L = 100$, filling $\langle n \rangle = 1$ and $U = 4t$. E_0 decreases for increasing m

with a different set of n_i is performed, until all n_i are measured. The size of the group depends on the number of states kept m and the size of the computer memory. The same procedure should also be performed for measuring correlation functions, although it is a lot of bookkeeping. An example: For the SIAM, we measured the correlation function of the z-component of the impurity spin and the z-component of the electrons in the conduction band

$$C(r) = \langle S_z^d S_z(r) \rangle - \langle S_z^d \rangle \langle S_z(r) \rangle$$

where S_z^d is the z-component of the impurity spin and $S_z(r)$ is the z-component of the electron on site r on the chain. The site of minimum truncation is near the position of the impurity. There is one additional point of importance to the procedure described above: if at some point of the final sweeps S_z^d and $S_z(r)$ act one the same block, one has to keep track of the product $S_z^d \cdot S_z(r)$ in addition to the single operators.

2.4.6 Calculating Dynamical Properties with DMRG

It has been demonstrated that the DMRG yields good results for ground state energies (and likewise for ground state properties in general). What physicists are really interested in are not only ground state properties, but also excited states and spectral densities, as they permit comparison of theoretical results with experimental ones. We show that the DMRG can also be used to calculate Green's functions and hence "all points of interest". The main issues in calculating dynamical properties with the DMRG are how to represent the basis at the region of interest (a specific ω) and how to calculate $A(\omega)$. Where for the second problem one can fall back on standard methods (e. g. [22]), the choice of the target states is more complicated. With just the ground states used as target states, the basis is inappropriate to describe excitations away from the Fermi edge. Currently, there are two different ways to calculate Green's functions with DMRG: the *Lanczos vector method* [31] and the *correction vector method* [32]. The *Lanczos vector method* is easy to implement and fast, but good results are only achieved for low-lying excited states. By contrast the *correction vector method* is more complicated and slower, but yields good results for the whole spectrum.

The Lanczos Vector Method

The idea of the *Lanczos vector method* is the following: build up the system to the desired size by means of the infinite system algorithm. Then finite size sweeps are carried out until convergence of the ground-state energy is achieved. Finally, calculate the spectral density in the way described in the

previous chapter. In order to represent the Krylov space more accurately, not only the ground state is used as target state, but also the first few Lanczos vectors. There are two problems of this method. First, the Lanczos tridiagonalization provides good results for low lying eigenvalues only. Second, the eigenvectors obtained from the Lanczos algorithm are not orthonormal. Since the density matrix is built not only from the ground-state but also from the first Lanczos vectors, you get more information about the Krylov space. However, due to the fact that only the low-lying eigenstates are represented properly in the Krylov space, this method is not sufficient to describe high excitations. We will explain this method by giving an example on how to apply the Lanczos vector method to a finite system.

Application of the Lanczos vector method to a finite system The Lanczos vector method is used to determine the spectral density at site i

$$A_i(\omega) = \langle\psi_0|c_i \frac{1}{\omega - H} c_i^\dagger|\psi_0\rangle \tag{2.36}$$

of a finite system. First, we calculate the Green's function and hence the spectral density. The Green's function is given by

$$G(i,\omega) = \sum_\alpha \left(\frac{|\langle i^+|\alpha\rangle|^2}{\omega - (E_\alpha - E_0) + i\eta} + \frac{|\langle i^-|\alpha\rangle|^2}{\omega + (E_\alpha - E_0) - i\eta} \right) \tag{2.37}$$

and the spectral density can be obtained from

$$A(\omega) = -\frac{1}{\pi}\mathrm{Im}\left(G(\omega)\right)$$

The program has to run two times for a given system size. The first part of the Green's function is calculated, which will then become the part with positive frequencies of the spectral density. The target states are now

$\|\psi_0\rangle$			the ground state
$c_i^\dagger\|\psi_0\rangle$	$=$	$\|f_0\rangle$	the first Lanczos vector
$\|f_i\rangle$			the first few Lanczos vectors

We usually use 3 target states: the ground state (50% of the weight) and the first two Lanczos vectors (each 25% of the weight). One has to keep track of the operator $c_i^\dagger$ for a given site i in each step, so not only the blocks have to be stored during the finite size algorithm, but possibly $c_i^\dagger$, too, if and only if the block to be saved contains the site i. After having reached convergence in the finite size algorithm, sweep back to the position where the

truncation errors of the two blocks are lowest. Then, proceed as described in the previous chapter: One calculates the first Lanczos vector $|f_0\rangle = c_i^\dagger|\psi_0\rangle$, then uses it to start the Lanczos routine. The peaks in the spectrum are obtained by shifting the eigenvalues by E_0. The weights are given by the first entry of the matching eigenvectors. This gives the right-hand side of the spectrum, i. e. the part with positive frequencies.

Next, calculate the left part of the spectrum. The whole calculation is the same with $c_i^\dagger$ and c_i interchanged, except for the representation of the peaks. In the Lanczos routine one calculates $\langle\psi_0|c_i^\dagger\frac{1}{\omega-H}c_i|\psi_0\rangle$. The peaks of the hole excitation have to be at $\omega = -(E_\alpha - E_0)$, so that the peaks have to be shifted and then reflected. Joining the two parts results in the full spectrum.

The correction vector method

The *correction vector method* offers a way to calculate the full spectrum even at regions of highly excited states. The target states that are no longer the first few Lanczos vectors are now given by:

$\|0\rangle$			the ground state
$\|A_0\rangle$	$=$	$A\|0\rangle$	the first Lanczos vector
$\|x(z)\rangle$	$=$	$\frac{1}{z-H}\|A_0\rangle$	the correction vector

with $z = \omega + i\eta$. The Hilbert space is truncated to optimally represent it in regions of a specific ω. The most complicated part in this method is the inversion of the Hamiltonian, needed to calculate $|x(z)\rangle$. Since $z = \omega + i\eta$, $|x(z)\rangle$ is complex and can be written as $|x(z)\rangle = |x^{\mathrm{re}}\rangle + i|x^{\mathrm{im}}\rangle$. The imaginary part of $|x(z)\rangle$ is therefore given by the following equation

$$\left((\omega - H)^2 + \eta^2\right)|x^{\mathrm{im}}\rangle = (-\eta)\,|A_0\rangle$$

This equation can be solved by standard methods, such as *conjugate gradient*. A restarted GMRES [17] has been proven to be stable and give accurate results. The real part of $|x(z)\rangle$ can be calculated directly from the imaginary part.

$$|x^{\mathrm{re}}\rangle = \frac{\omega - H}{(\omega - H)^2 + \eta^2}|A_0\rangle = \frac{H - \omega}{\eta}|x^{\mathrm{im}}\rangle$$

The correction vector method uses 4 target states in total: the ground state, the first Lanczos vector as well as the real and imaginary part of the correction vector. The downside of this method is that you have to run the program for every region you are interested in. In addition, the inversion of the Hamiltonian at each DMRG step takes a lot of time. The choice of η

plays a key role: The wider the broadening, the faster the calculation. A large η results in a large diagonal of the denominator, which speeds up the inversion. Unfortunately, the smaller the broadening, the better the resolution and the more information is accessible from the plot. Whereas the Lanczos vector method gives the peaks and corresponding weights of the excitation spectrum, the correction vector *just* gives a single point of the spectrum. Each peak is now represented by a Lorentzian with broadening η. Since the correction vector has to be calculated in each step, it is no effort to also calculate $A(\omega)$ in each step. But due to different truncation errors, $A(\omega)$ changes when we sweep through the superblock. One should therefore get the position where the ground state energy reaches its minimum, and use $A(\omega)$ obtained at the same position. We found that $A(\omega)$ also reaches its minimum value when E_0 does, but cannot explain why it is a minimum. As far as we know, it is not known that the correction vector method is a variational method with $A(\omega)_{cv} \geq A(\omega)_{exact}$. The variation of $A(\omega)$ is small when $\omega \approx 0$ and $\omega \approx D$, i. e. near the Fermi edge and the band edge. In between, the variation gets larger due to fluctuations from both sides of the spectrum. The method can be improved by using two correction vectors with $\omega_1 - \omega_2 \approx 2\eta$. After the system is converged, one can use the Lanczos method to calculate the spectrum. The basis is then optimized to represent states in the region between ω_1 and ω_2.

Comparison between Lanczos and Correction vector method In order to compare both methods we calculate the spectral density for a SIAM with 63 sites. We first set $U = 0$ to compare both methods with the exact results, then set U to a finite value to see if the methods show different results.

In Fig. 2.11 one can see that the correction vector method gives accurate results for the whole spectrum. The Lanczos vector method gives perfect results near the Fermi edge ($\omega = 0$) and at the band edge. The method fails to describe the spectrum in the middle of the band, between $\omega = -1$ and $\omega = -0.4$. To illustrate the fluctuation of A_d that is obtained from the correction vector method, we also show Fig. 2.12. The cross marks the mean value and all values obtained lie in between the *error bars*. The fluctuations become larger when moving away from the band edge. We now turn on the interaction by setting $U = 5$ without changing any of the other parameters. We cannot compare the results to an exact solution anymore. We also separate the spectrum in a left (hole excitations) and right (particle excitations) part.

It is easy to see that the spectrum obtained from the Lanczos vector

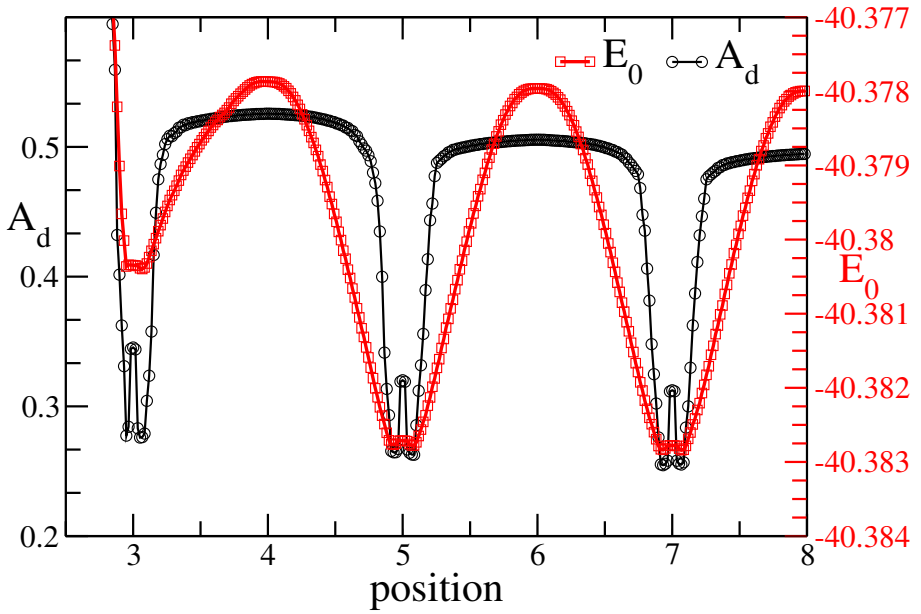

Figure 2.10: The spectral density $A_d(\omega)$ for a specific ω for a SIAM and the corresponding ground state energy. With impurity position $x_0 = 4$, one can see that both values have their minimum at the same position ($\approx 7 - 8$)

method matches the correction vector results in a region around the Fermi edge. If one is only interested in that specific region of the spectrum, the Lanczos vector method is the method of choice.

Conclusion

Methods to calculate spectral densities have been introduced. The *Lanczos vector method* is easy to implement and the calculations are fast. The disadvantage is that this method cannot describe high excitations and is useful for low lying excited states only. The *correction vector method* can give accurate results for the whole spectrum. Unfortunately, it is difficult to implement because of the matrix inversion it requires. It is also slow, because it has to run a lot of times due to the choice of the correction vector, which is specific for a given ω.

2.4.7 Improvements of the DMRG

A lot of work has been put into DMRG in the past years, which gave rise to the calculation of a lot of different quantities. We only used a small subset of DMRG, the *standard* DMRG (finite system algorithm and ground state

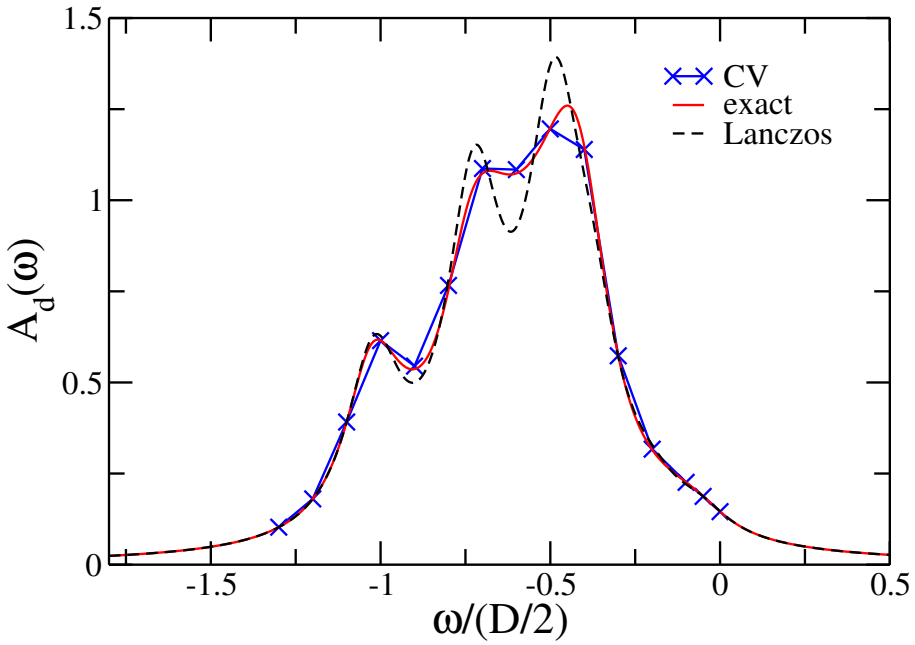

Figure 2.11: The spectral density $A_d(\omega)$ obtained by the Lanczos vector method and correction vector method compared to the exact results. The physical parameters of the SIAM are $U = 0$, $V = 0.35$, $\varepsilon_d = -0.35$ in units of the half bandwidth $D/2$, $L = 63$, $x_0 = 4$, $n = 64$; $\eta = 0.1$ for the CV as well as for the Lanczos vector method. We kept $m = 200$ states for the correction vector method and $m = 800$ for the Lanczos vector method.

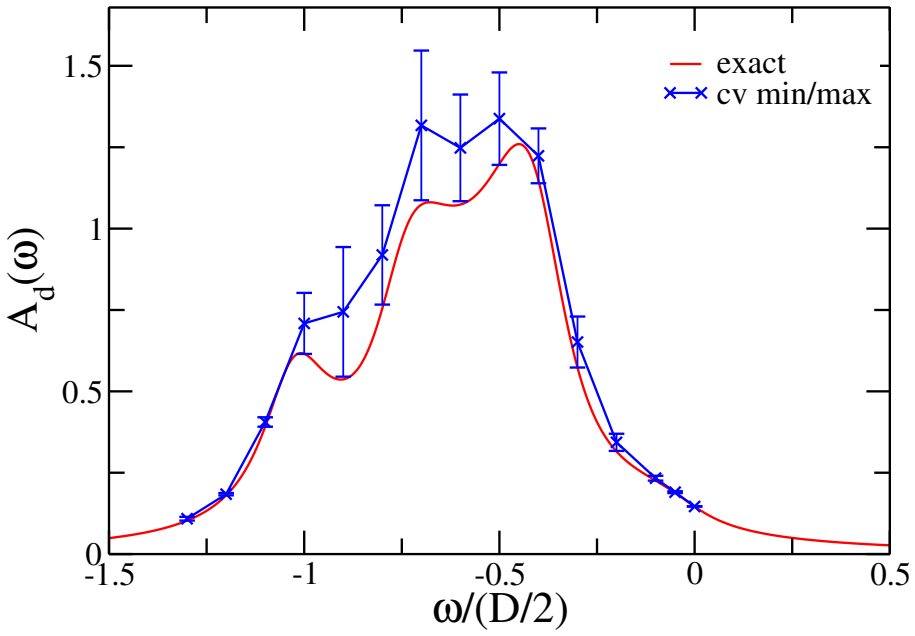

Figure 2.12: The spectral density $A_d(\omega)$ obtained by the correction vector method compared to the exact results. The physical parameters of the SIAM are $U = 0$, $V = 0.35$, $\varepsilon_d = -0.35$ in units of the half bandwidth $D/2$, $L = 63$, $x_0 = 4$, $n = 64$ and $\eta = 0.1$. We kept $m = 200$ states.

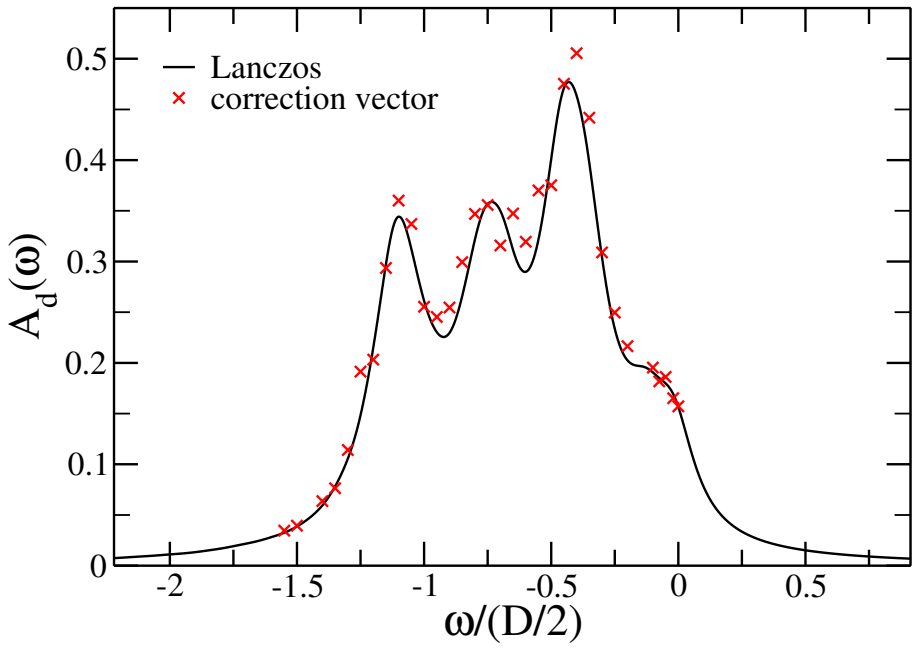

Figure 2.13: The spectral density $A_d(\omega)$ obtained by the Lanczos vector and correction vector method. The physical parameters of the SIAM are $U = 5$, $V = 0.35$, $\varepsilon_d = -0.35$ in units of the half bandwidth $D/2$, $L = 63$, $x_0 = 4$, $n = 64$; $\eta = 0.1$ for the CV as well as for the Lanczos vector method. We kept $m = 200$ states for the correction vector method and $m = 800$ for the Lanczos vector method.

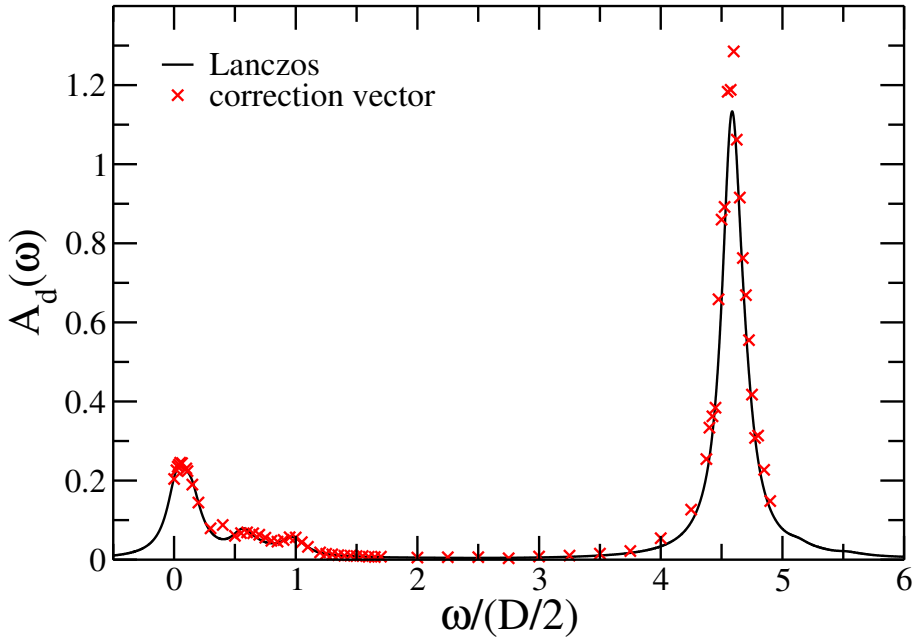

Figure 2.14: The spectral density $A_d(\omega)$ obtained by the Lanczos vector and correction vector method. The physical parameters of the SIAM are $U = 5$, $V = 0.35$, $\varepsilon_d = -0.35$ in units of the half bandwidth $D/2$, $L = 63$, $x_0 = 4$, $n = 64$; $\eta = 0.1$ for the CV as well as for the Lanczos vector method. We kept $m = 200$ states for the correction vector method and $m = 800$ for the Lanczos vector method.

properties/correlation functions) and dynamical properties with the Lanczos as well as the correction vector method. We will now mention other aspects of DMRG. [33] gives a good overview and insight in these improvements.
It is also possible to treat bosons with DMRG. On first sight, this might not be too strange, but one has to think of the single site basis for a system of bosons! For spin 1/2 fermions, the number of states for a single site in the Hubbard model is 4. For spin 0 bosons, the number of basis states for a single site is only limited to the total number of bosons in the system. The trick is to truncate the single site basis in the very beginning: This is done a setting a maximum number of bosons per site, usually about 5-8.
Two-dimensional quantum systems have also been calculated by DMRG. Although one can reorganize the lattice such that sweeping is still possible, one has to keep track of much more operators, because the number of edge sites is increased drastically. A 2D system can also be mapped onto a 1D system with long range interaction. But although this is a problem for DMRG, it has given interesting results for the 2D Heisenberg or $t - J$ model.
Momentum-space DMRG makes momentum a good quantum number, works naturally with periodic boundary conditions, and allows trivial manipulation of the single-particle dispersion.
DMRG has also made a contribution to the field of quantum chemistry.
Conventional DMRG is essentially restricted to $T = 0$ calculations. The DMRG idea can also be used for the decimation of transfer matrices, leading to the name of *transfer-matrix renormalization group* (TMRG). This opened the way to DMRG studies of classical statistical mechanics at finite temperature for systems on two-dimensional $L \times \infty$ strips. If one applies the generic mapping of d-dimensional quantum systems at finite temperature to $(d+1)$-dimensional classical systems, TMRG also permits study of thermodynamic properties of one-dimensional quantum systems at finite temperature.
For systems out of equilibrium, there is the transition matrix approach and the *time-dependent* DMRG.

Chapter 3

Results for the SIAM

3.1 Introduction

It is possible to create and investigate small Kondo boxes, a device consisting only of a few hundred atoms and a single impurity, by means of scanning tunneling microscopy (STM). One might expect that in the near future it will be possible to build Kondo boxes consisting of only a few atoms. In these samples the conduction electron spectrum becomes discrete with a non-zero mean level spacing. This is one of the most fundamental features of quantum mechanics. Due to the level spacing it is now possible that the density of states at the Fermi level at the site that is connected to the impurity is zero. But what happens to the Kondo peak in this case, since a fully developed resonance requires a finite density of states? A first investigation is presented by [34]. In further studies we found many new interesting properties presented in this section and in [35]. The results shown here are obtained by means of the density matrix renormalization group and the Lanczos vector method. We are especially interested in the Kondo peak. This resonance is located near the Fermi level, such that the Lanczos method is sufficient for our purpose. Spectral densities are calculated in the way described in the previous chapters. $A_d(\omega)$ denotes the spectral density on the impurity site and $A_c(\omega)$ is the spectral density on the site of the chain that is connected with the impurity (x_0). It is important to clarify that site x_0 is not fixed: it is neither the first site of the chain, nor the site in the middle of the chain. It can be chosen freely. In addition, the chain sites in our model represent sites in real space and not energy shells like NRG calculations.

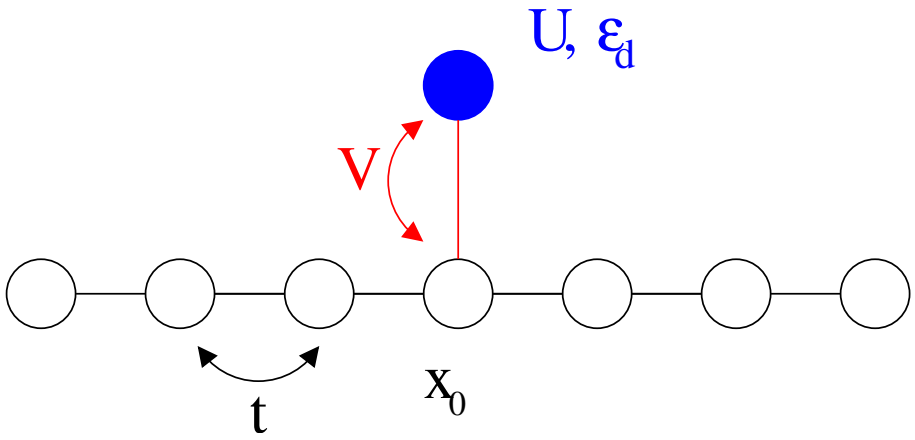

Figure 3.1: SIAM: a single Anderson impurity connected to a tight-binding chain

The model is depicted in Fig. 3.1 and the Hamiltonian is given by:

$$\begin{aligned} H &= -t\sum_{i,\sigma} c^\dagger_{i,\sigma}c_{i+1,\sigma} + \text{h. c.} \\ &+ V\sum_{\sigma}\left(d^\dagger_\sigma c_\sigma(x_0) + c^\dagger_\sigma(x_0)d_\sigma\right) \\ &+ \varepsilon_d\sum_{\sigma} n_{d,\sigma} + U n_{d,\uparrow}n_{d,\downarrow}. \end{aligned}$$

$c^\dagger_{i,\sigma}$ and $c_{i,\sigma}$ are creation and annihilation operators for conduction band electrons, respectively. $d^\dagger_\sigma$ and d_σ denote creation and annihilation operators on the impurity. n_d is the occupation number on the impurity. V is the coupling of the impurity and the chain, and U is the coulomb repulsion on the impurity. We have to emphasize that there are some differences to the standard SIAM:

- local coupling: The impurity in our model is only coupled to a single site of the tight binding chain.

- non-flat conduction band: The conduction band is not flat in our system. It is determined by the finite size and the position of the impurity. We will show that this has a strong effect on the physics.

- finite system and canonical ensemble: Our system is a finite system in a canonical ensemble. Thus, we have a fixed number of particles and

S_z^{total}. This results in the fact that the impurity spin is always fully compensated within the system, which makes it impossible to use the standard definition of the Kondo screening cloud.

This chapter is organized as follows: We will show that the position of the impurity — the site x_0 — has a strong effect on the spectral density $A_d(\omega)$ on the impurity. We will also show how $A_d(\omega)$ changes when the system size is increased. Systems with an even and odd number of particles are calculated. We will compare these results with previous works in [36]. We will also examine the *holy grail* of Kondo physics - the Kondo screening cloud [37]. The goal of this chapter is to show similarities as well as strong differences to the results that the theory of the standard model gives. We hope to present some insight in the problems and issues one has to cope with when experimenting with system (e.g. nanotubes) that are so small that finite size effects occur.

3.2 Parameters and T_K

There is a parameter regime in which the Anderson model exhibits a *local moment* and an anti-ferromagnetic exchange interaction with the conduction electrons. The conditions for this parameter regime are:

$$\begin{aligned} \varepsilon_d + U &\gg \varepsilon_F \\ \varepsilon_d &\ll \varepsilon_F \\ &\text{with} \\ |\varepsilon_d + U - \varepsilon_F| &\gg \Gamma \\ |\varepsilon_F - \varepsilon_d| &\gg \Gamma \end{aligned}$$

with hybridization $\Gamma = \pi V^2 \rho_0$, where ρ_0 is the local density of states at site x_0. We started our calculations with $U = 5.0$, $\varepsilon_d = -0.55$, $V = 0.35$[1], a set of parameters which *seems* to satisfy the above conditions. (The only value that can not be set directly is Γ.) The Kondo temperature for a SIAM is given by

$$T_K \sim D \left(\frac{\Gamma U}{|\varepsilon_d||\varepsilon_d + U|} \right)^{1/2} \exp\left(\frac{-\pi |\varepsilon_d||\varepsilon_d + U|}{2\Gamma U} \right) \tag{3.1}$$

One parameter of the system is the position of the impurity on the chain, that is the site labeled x_0, that is connected to the Anderson impurity. It

[1] all units in this chapter are expressed in units of the half bandwidth $D/2 = 2t$

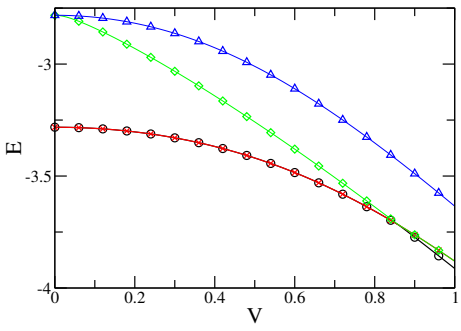

Figure 3.2: 4 lowest lying energies vs. V for $x_0 = 3$ (odd), $L = 5$, $N = 6$, $S_z^{tot} = 0$, $U = 5.0$, $\varepsilon_d = -0.55$. The ground state is twofold degenerate for $V < 0.8$

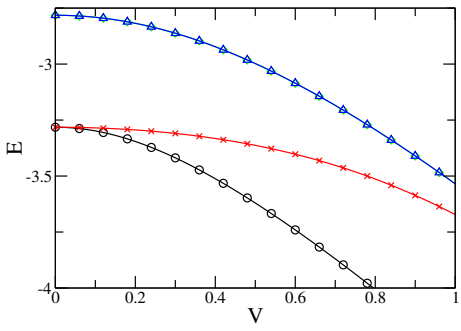

Figure 3.3: 4 lowest lying energies vs. V for $x_0 = 2$ (even), $L = 5$, $N = 6$, $S_z^{tot} = 0$, $U = 5.0$, $\varepsilon_d = -0.55$. The ground state is not degenerate for $V \neq 0$.

turns out that this has much more effect on the system than is expected: The problem is that the ground state is twofold degenerate for our typical set of physical parameters ($U = 5.0$, $\varepsilon_d = -0.55$, $V = 0.35$) if x_0 is an odd site (the chain starts with site number 0) and we have an odd number of sites on the chain. This is due to the single particle wave function of the electron on the Fermi edge, that has a node at all odd sites. We have plotted the 4 lowest lying energies for a SIAM with $L = 5$ (number of lattice sites), $N = 6$ (number of particles), $S_z^{total} = 0$ (z-component of total spin), $U = 5.0$, $\varepsilon_d = -0.55$ for different values of V in Fig. 3.2 and Fig. 3.3. For $V = 0$, the ground state of both system is two-fold degenerate, because the impurity is not connected to the chain, and the ground state of the impurity is two-fold degenerate. It is given by

$$|\Psi_0\rangle = \alpha|\uparrow\rangle + \beta|\downarrow\rangle \text{ , with } \alpha^2 + \beta^2 = 1.$$

By turning on V, the hybridization of the impurity and the chain, the degeneracy of the ground state is lifted if x_0 is even, whereas the system stays degenerate if x_0 is odd. The different behavior comes from the different density of states of site x_0. For $V = 0$, L odd and half filling, there is an odd number of electrons on the chain, with one electron sitting at the Fermi edge and one electron at the impurity site. By turning on V, this electron, with $\varepsilon_k = \varepsilon_F$, interacts with the impurity. But if x_0 is odd, the wave function of this electron has a node at each odd site of the chain. The electron *does not see* the impurity. The other electrons below the Fermi surface have a finite density probability at x_0, but their energy is too low. It is not favorable to interact with the impurity, because there would not be any gain in energy.

On the other side, the wave function of the electron at the Fermi edge has a maximum at each even site. Thus, the degeneracy is immediately lifted by turning on the connection to the impurity. To avoid degeneracy, we chose x_0 to be even. But also the choice of the even site has a strong effect on the physics. This comes from the local density of states ρ_0 on site x_0, which is strongly dependent on the position. The local density of states for a tight binding chain with 255 sites for two different x_0 and different broadening is depicted in Fig. 3.4 — 3.6. The value of $A(\omega \equiv 0)$ is independent of the position of x_0 if the broadening is turned off. As mentioned before, the wave function of the electron on the Fermi edge has a maximum and the same value at every even site. By decreasing the broadening σ, one can see that for $x_0 = 4$, much more weight is localized in the region around $\omega = 0$ than if $x_0 = 50$. The Kondo temperature is given by (3.1). The only parameters that depends directly on x_0 is ρ_0. It is calculated by summing over the density of all single particle wave functions within the region $\Delta\varepsilon$ around the Fermi level:

$$\rho_0(\Delta\varepsilon) = \sum_{k,|\varepsilon_k|<\Delta\varepsilon} \frac{|\Psi_k(x_0)|^2}{\varepsilon_k}. \tag{3.2}$$

Although (3.1) can not be applied to finite systems (the formula must be changed due to the fact that the density of states at the Fermi level can be zero), we expect the Kondo temperature to be larger if ρ_0 is increased. To get an estimate of the Kondo temperature, we compare the first order and second order term in J in a perturbative approach. Thus, T_K is defined by

$$-2J^2 \sum_k |\Psi_k(x_0)|^2/((\exp(\varepsilon_k/T_K)+1)\varepsilon_k) = J, \tag{3.3}$$

where $\Psi_k(x_0)$ is the probability density at site x_0 of the single particle wave functions. The Kondo coupling J is obtained through Schrieffer-Wolff transformation [38] from the parameters of the SIAM by:

$$J = \frac{V^2}{|\varepsilon_d|} + \frac{V^2}{|\varepsilon_d + U|}. \tag{3.4}$$

A solution for this equation — and therefore a valid value for T_K — does not exist for all parameters. We have plotted T_K for different values of x_0 in Fig. 3.7. The Kondo temperature is larger at the band edge due to the high local density of states ρ_0 at x_0. If x_0 moves to the middle of the band, ρ_0 decreases as well as T_K. For a critical x_0, ρ_0 gets too small, such that (3.3) does not have a solution, and T_K is not defined. This behavior can be found for larger as well as for smaller systems. The smaller the system, the smaller the region where T_K is defined. We emphasize that this method gives only

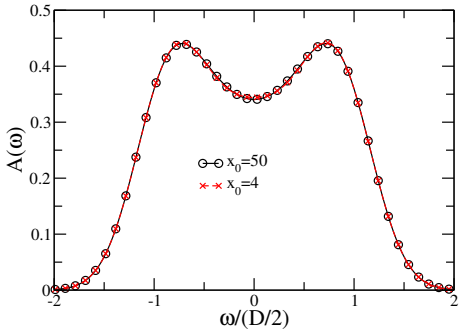

Figure 3.4: local DOS for a tight binding chain, $L = 255$, $\sigma = 0.1$

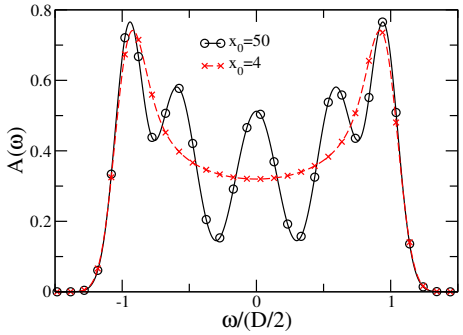

Figure 3.5: local DOS for a tight binding chain, $L = 255$, $\sigma = 0.01$

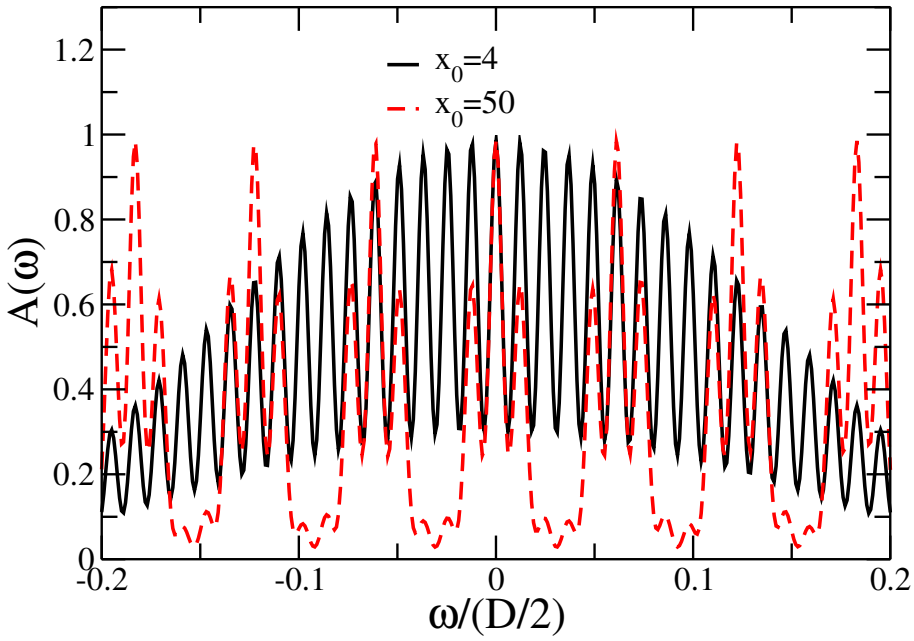

Figure 3.6: local DOS for a tight binding chain, $L = 255$, $\sigma = 10^{-5}$

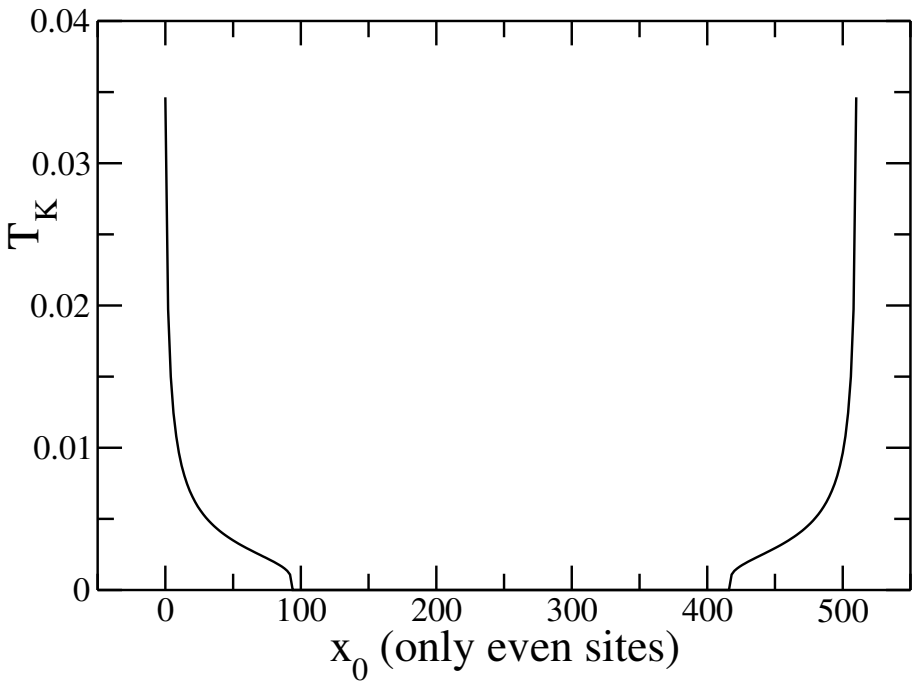

Figure 3.7: T_K vs x_0 with $U = 5.0$, $\varepsilon_d = -0.55$, $V = 0.35$, $L = 511$. T_K is obtained from (3.3), and x_0 is chosen to be even, because T_K is not defined for an odd x_0.

an estimate of the Kondo temperature.

3.3 Spectral Densities for the SIAM

We now calculate the spectral density A_d on the impurity with the same set of parameters for different x_0. In Fig. 3.8 we have plotted the full spectrum of a SIAM with $U = 5.0$, $\varepsilon_d = -0.55$, $V = 0.35$, $L = 127$ for $x_0 = 4$ and $x_0 = 50$. On the right hand side of the spectrum, we see a peak at $\omega \approx U + 2\varepsilon_d$. Since this peak is not our main point of interest, it will be cut out in the following plots, so we can focus on the region around the Kondo peak, at $\omega = 0$. In Fig. 3.9 we see a cut-out of the spectral density plot of the same system. At $\omega \approx 0$ we can see a peak in both plots, with the one for $x_0 = 4$ being substantially larger than for $x_0 = 50$. This is exactly what we expected: The higher local density of states at site $x_0 = 4$ allows more electrons to contribute to the Kondo peak. Or in other words: the larger local DOS at x_0 leads to a higher Kondo temperature. The Kondo temperature is connected to the height of the Kondo peak. (Height and weight is more or less the same in our problem. The DMRG program gives the position and the weight of the peaks. Due to the Gaussian broadening, the weight of the peak is connected to the height of the peak. The width of the peak is given by the fictitious broadening σ). To make sure that the peak at $\omega = 0$ is due to the interactions on the impurity we look at the spectral density of a non-interacting SIAM. We can see that for the non-interacting case, there is no peak at the Fermi edge, as can be seen in Fig. 3.10. We can see a non-zero DOS at the Fermi edge, but this is due to the large broadening. The peak at the left most side comes from the high local DOS at the band edge, and the other two peaks come from finite-size effects and the symmetry of the wave function. For the interacting case, we will most often see one peak at $U + 2\varepsilon_d$ and one at $\omega \approx -D/2$. In addition to this, we also see one peak at the Fermi edge ($\omega \approx 0$), the Kondo peak, and a few peaks in the middle of the band. As a matter of course the total number of peaks depends on the broadening, but we usually choose the broadening such that the plots do not look too obscure. We now compare the height of the Kondo peak for several positions of x_0 with the Kondo temperature. Unfortunately, (3.3) gives only valid values for just a few sites. Nevertheless, Fig. 3.11, where we plot the height of the Kondo peak for a set of different x_0, resembles Fig. 3.7, although this was calculated for a different system size. In Fig.3.12 we see that the shape of the curve is not dependent on the system size.

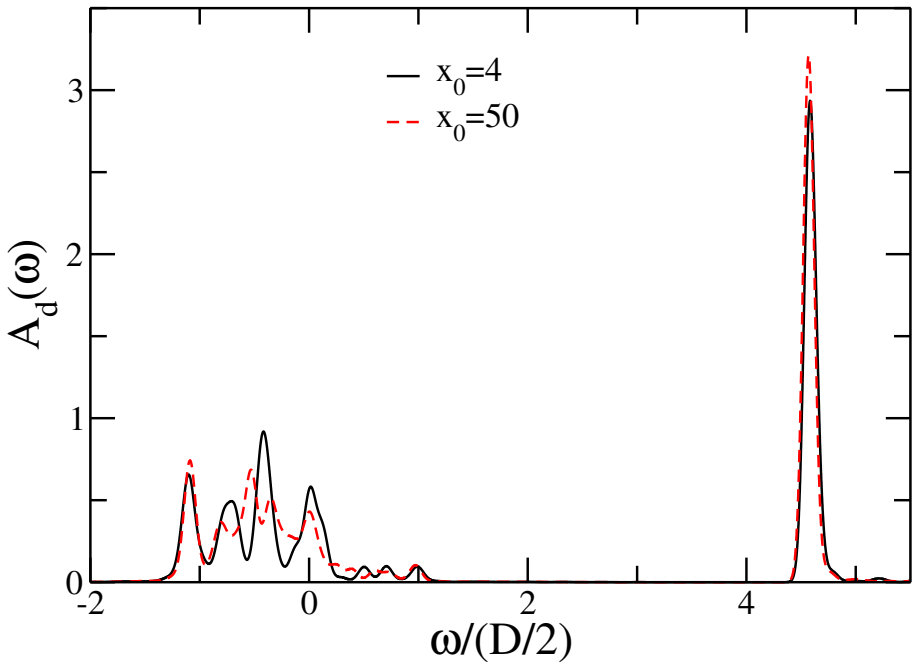

Figure 3.8: $A_d(\omega)$ with $U = 5.0$, $\varepsilon_d = -0.55$, $V = 0.35$, $L = 127$ and different x_0. We use Gaussian broadening with $\sigma = 0.05$ and kept $m = 1000$ states.

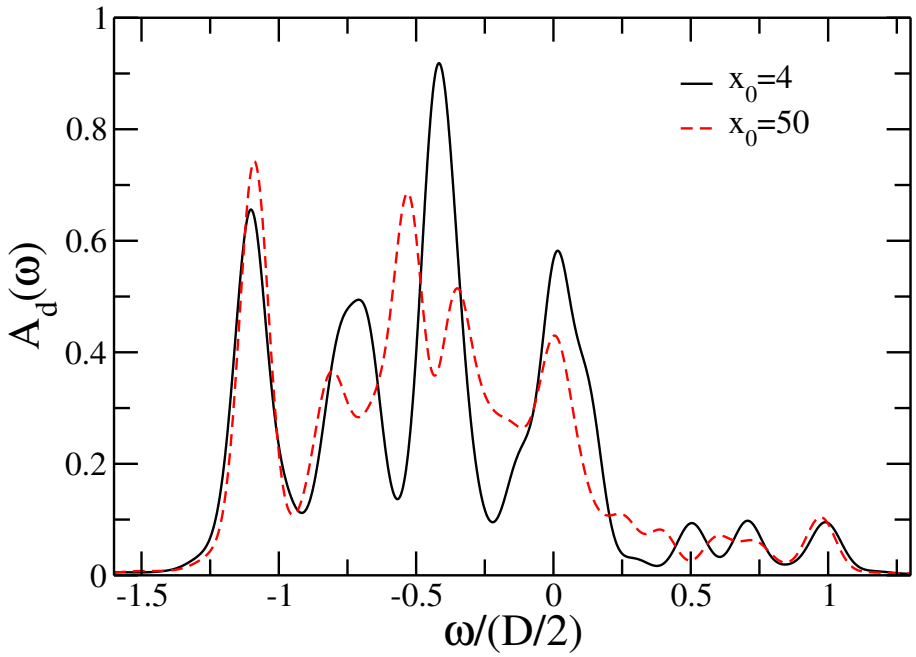

Figure 3.9: $A_d(\omega)$ with $U = 5.0$, $\varepsilon_d = -0.55$, $V = 0.35$, $L = 127$ and different x_0. We use Gaussian broadening with $\sigma = 0.05$ and kept $m = 1000$ states.

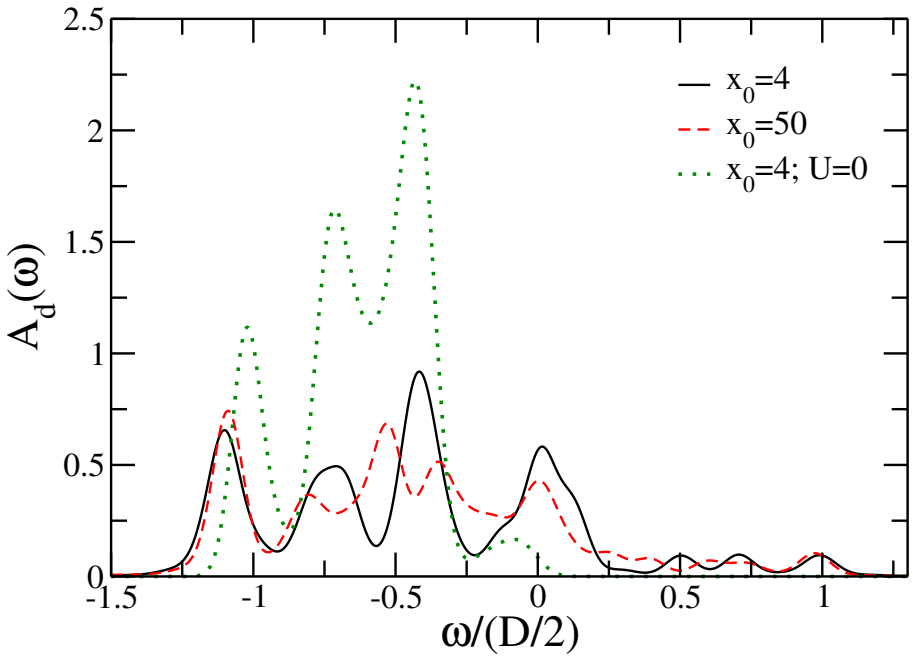

Figure 3.10: $A_d(\omega)$ with $U = 5.0$, $\varepsilon_d = -0.55$, $V = 0.35$, $L = 127$, $N = 128$ and different x_0 and the free solution. We use Gaussian broadening with $\sigma = 0.05$ and kept $m = 1000$ states.

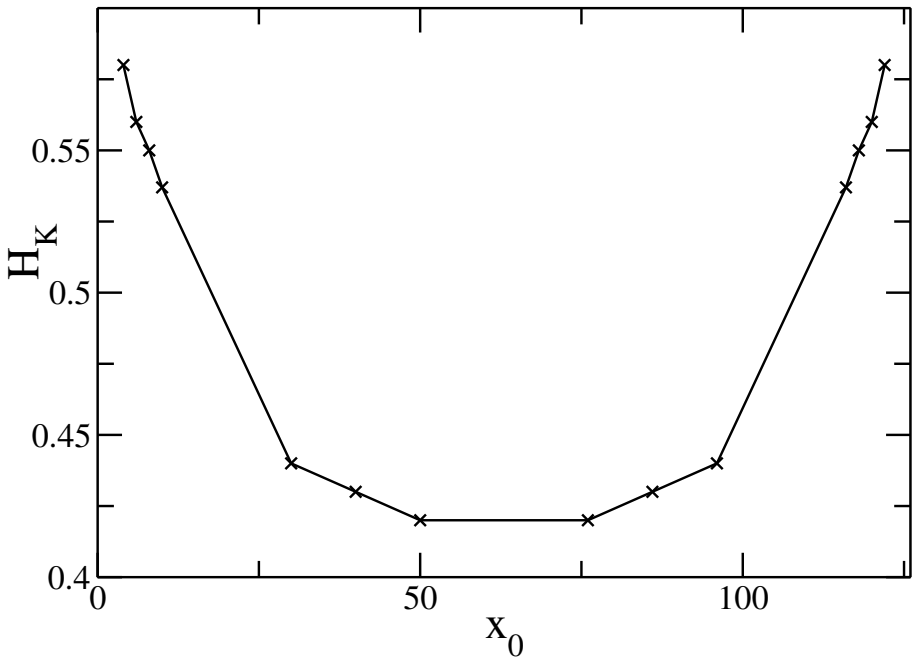

Figure 3.11: Height of the Kondo peak H_K with $U = 5.0$, $\varepsilon_d = -0.55$, $V = 0.35$, $L = 127$, $N = 128$ and different x_0. The value for the height is obtained by using Gaussian broadening with $\sigma = 0.05$. We kept $m = 1000$ states for the DMRG calculation.

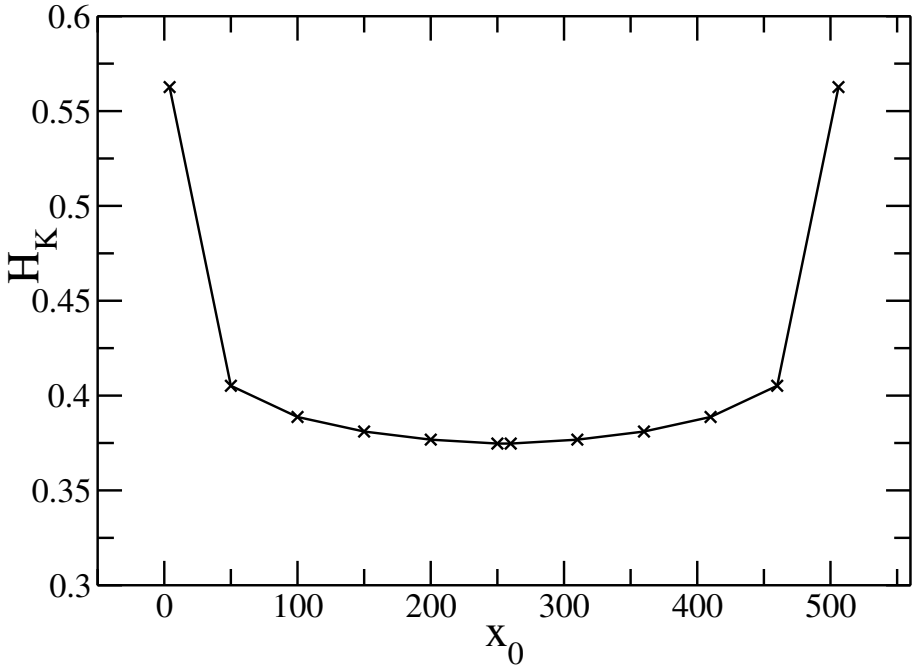

Figure 3.12: Height of the Kondo peak H_K with $U = 5.0$, $\varepsilon_d = -0.55$, $V = 0.35$, $L = 511$ and different x_0. The value for the height is obtained by using Gaussian broadening with $\sigma = 0.05$. We kept $m = 1000$ states for the DMRG calculation.

3.3.1 Larger Systems

An interesting issue is the behavior of the Kondo peak when the system size is increased. By increasing the system size, the local DOS will most likely change, too. $|\Psi_k(x_0)|^2$ is decreased, because the wave function is spread over more sites. But since the level spacing ΔE is decreased, this could even out such that the local DOS could change only slightly. This effect was first proposed by [34]. We calculated the spectral density on the impurity for chains of 63, 127, 255 and 511 chain sites. If the impurity is connected to a site with a high local DOS, the Kondo peak does change only slightly when the system size is increased. This effect is depicted in Fig. 3.13. Moving x_0 to the middle of the system, where ρ_0 and therefore T_K gets smaller, one expects a similar behavior. But the results differ: In Fig. 3.14 we can see that the Kondo peak gets smaller when we increase the system size. Why does the peak get smaller with x_0 in the middle of the system when the system size is increased and stays fixed when x_0 is at the edge of the chain (e. g. $x_0 = 4$)? ρ_0 is what the impurity *sees* of the chain and should therefore be responsible for this effect. By calculating ρ_0, one sums over all single electron states with energy $|\varepsilon_k| < \Delta\varepsilon$. But what is the value of $\Delta\varepsilon$? To calculate the matching ρ_0 for the Kondo peak one should sum over all states that lie within the Kondo peak, hence $\Delta\varepsilon \approx T_K$. This — as well as 3.3 — is only an estimate. It leads to a self-consistent loop:

1. choose T_K
2. calculate ρ_0
3. calculate T_K
4. go back to step 2 until T_K converges

We see that T_K is very sensitive to ρ_0. The Kondo resonance requires a finite density of states near the Fermi edge E_F. We assume that for systems with small ρ_0, the DOS is just too small for a fully developed Kondo resonance. In this case, only a few — or maybe even just one — electron contribute to the Kondo peak. ‘

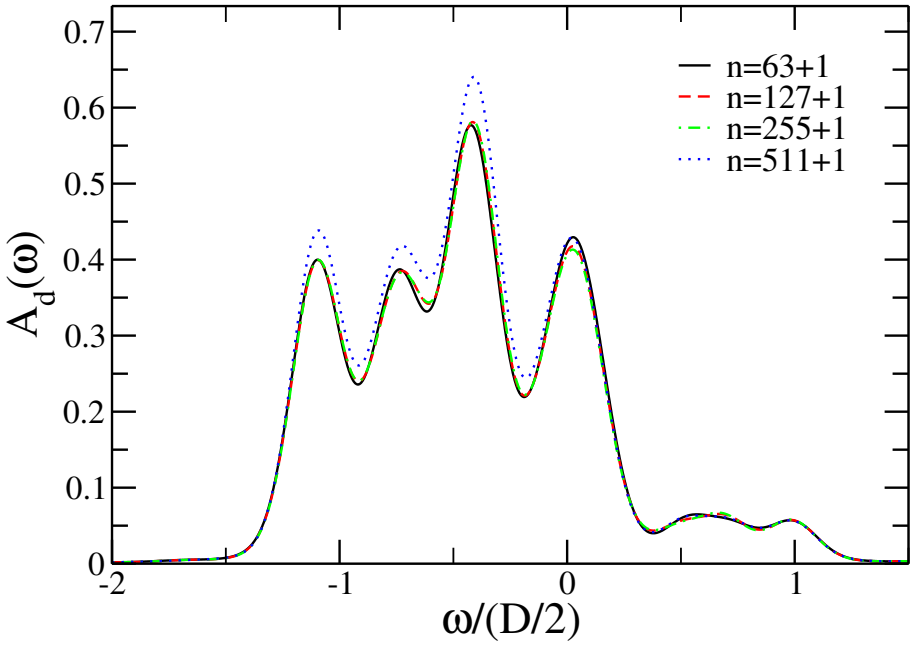

Figure 3.13: $A_d(\omega)$ with $U = 5.0$, $\varepsilon_d = -0.55$, $V = 0.35$, different L and $x_0 = 4$ at half filling. We kept up to $m = 2600$ states for the larger systems. The Gaussian broadening is $\sigma = 0.05$.

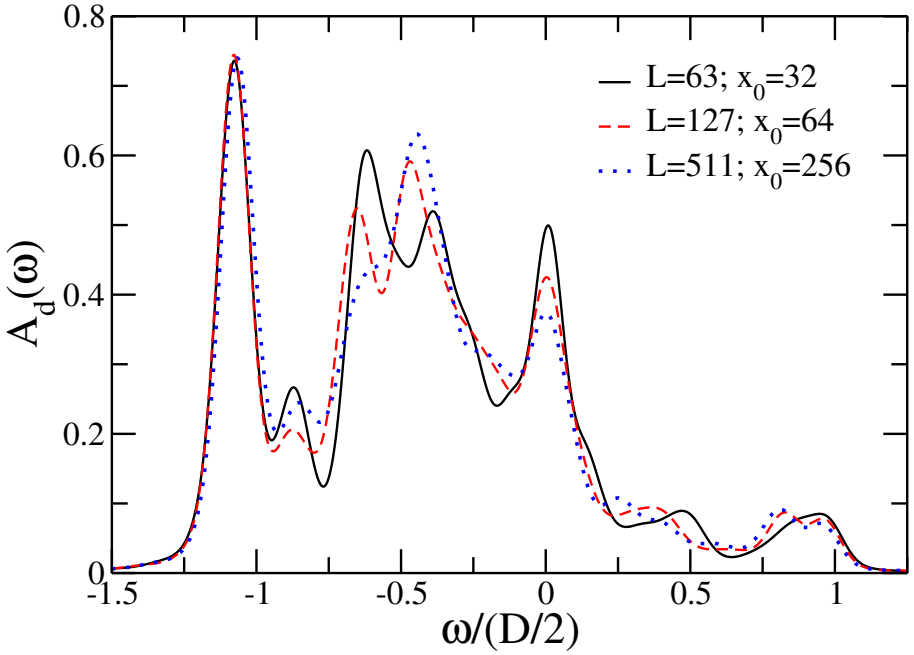

Figure 3.14: $A_d(\omega)$ with $U = 5.0$, $\varepsilon_d = -0.55$, $V = 0.35$, different L and x_0 in the middle of the system at half filling. We kept up to $m = 1700$ states for the larger systems. The Gaussian broadening is $\sigma = 0.05$

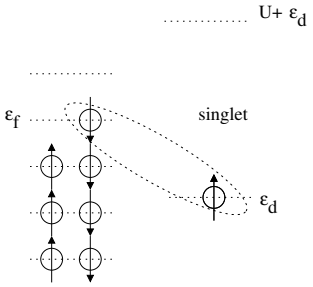

Figure 3.15: Spin flip with even number of particles

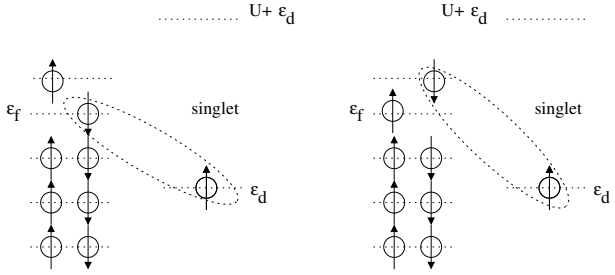

Figure 3.16: Spin flip with odd number of particles; one of the two electrons at the topmost level must move to the next-higher-lying level to allow spin flip

3.3.2 The Even-Odd Effect

In the previous section we only looked at systems with odd L at half filling, so that the total number of electrons N is even. We also examine the behavior of the Kondo peak when we have an even or odd number of particles in the system and look for the even-odd-effect described in [36]: They find that when the level spacing ΔE is much larger than T_K, the shape of the Kondo resonance differ strikingly for an even or odd number of particles. For an even number of particles in the system, spin-flip transitions lower the energy by roughly T_K by binding the d-electron and the conduction electrons into a singlet, in which the topmost, singly occupied level of the free Fermi sea carries the dominant weight, hence a single dominant peak in A_d. For an odd number of particles, the free Fermi sea's topmost level is doubly occupied, blocking energy-lowering spin-flip transitions. To allow the latter to occur, these topmost two electrons are redistributed with roughly the same weights between this and the next-higher-lying energy level, causing two main peaks and reducing the net gain from T_K by an amount of order of the level spacing ΔE. The spin flip transitions are depicted in Fig. 3.15 and Fig. 3.16. We do not observe this effect in our calculations. One main difference in both calculations is that we consider the system in a canonical ensemble with a fixed particle number N and S_z^{total}, whereas the system is in a the grand canonical ensemble in [36]. In addition to that, the impurity in our model does only couple to a single site of the tight-binding chain, whereas their impurity is equally coupled to all energy levels. Another difference is the way the spectral density is calculated: if N is even and $S_z^{total} = 0$, the system exhibits S_z symmetry, such that $A_d(\omega)$ is independent on the spin of the construction and annihilation operator that is used to calculate the spectrum, and therefore $A_{d,\sigma}(\omega) = A_{d,-\sigma}(\omega)$. If N is odd and $S_z^{total} = -1/2$,

the system does not exhibit this symmetry and $A_{d,\sigma}(\omega) \neq A_{d,-\sigma}(\omega)$. The problem might be that for the odd case, the two topmost electrons are not redistributed with the *same* weight between this and the next-higher-lying energy level. Although two energy levels are involved in spin flip transition, only one is supposedly carrying the dominant weight.
However, we can see a difference in the weight of the Kondo peak, when we consider an even or odd number of particles. The Kondo peak for the odd N has less weight than for the even N. We examined systems with $L = 127$ and $L = 128$ sites and $N = L+1$ (half filling) and $N = L$, $L+2$ (one particle above and below half filling). We summed over both spin configurations when calculating $A_d(\omega)$ for an odd N. The Kondo peaks for an even number of particles are always larger than the peaks with an odd number of particles. This can be explained by the even-odd effect described above. Spin flip transitions are less effective if N is odd, because one electron has to be lifted and the energy ΔE has to be paid. One can see that the height of the Kondo peak oscillates when the the number of particles changes between even and odd. This could be used as a signature for experiments.
What happens to the Kondo peak when the system size is increased and N is odd? If N is even, we found that H_K, the height of the Kondo resonance, does not change when the system changes size, if ρ_0 is sufficiently large. We looked at chains with $L = 100$ to $L = 500$ sites and put the impurity at site $x_0 = 4$. First, we chose $S_z^{total} = -1/2$ and looked at $A_{d,+1/2}(\omega)$. In Fig. 3.19 we plotted $A_d(\omega)$ for systems with $L = 100, 300, 500$ sites. One can see that the Kondo peak increases when the system gets larger. It also seems to converge for larger system sizes. This effect can be explained as follows: Spin-flip transitions for an odd N cost an additional ΔE. ΔE, the level spacing is decreased with $\sim 1/L$, such that spin flip transitions become more favorable when the system gets larger. In Fig. 3.20 we plotted the weight of the Kondo peak W_K versus the system size L with an odd number of particles N. One can see that the weight increases when the system gets larger. The weight also converges for larger system sizes. This is obvious, because the level spacing ΔE also converges for larger systems.

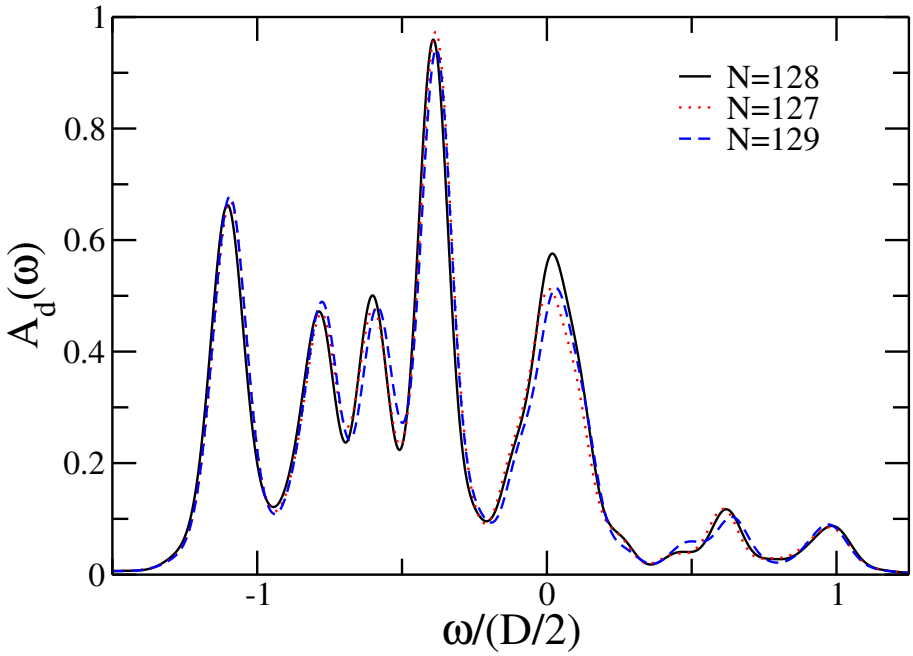

Figure 3.17: $A_d(\omega)$ with $L = 127$ and different N, with $U = 5.0$, $\varepsilon_d = -0.55$, $V = 0.35$. We kept up to $m = 1000$ states. The Gaussian broadening is $\sigma = 0.05$. The Kondo peak is smaller when N is odd.

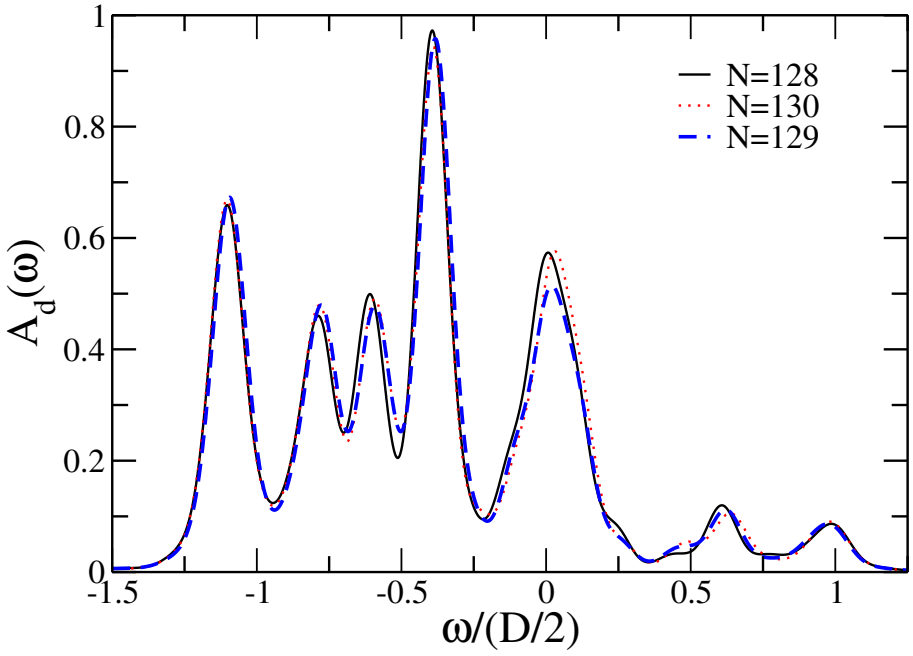

Figure 3.18: $A_d(\omega)$ with $L = 128$ and different N, with $U = 5.0$, $\varepsilon_d = -0.55$, $V = 0.35$. We kept up to $m = 1000$ states. The Gaussian broadening is $\sigma = 0.05$. The Kondo peak is smaller when N is odd.

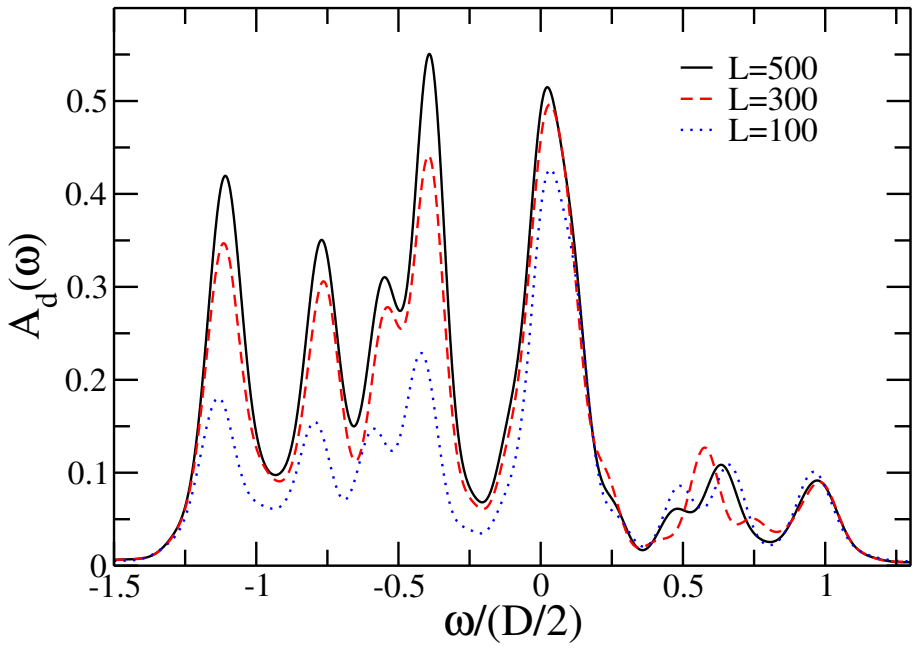

Figure 3.19: $A_d(\omega)$ with different L and odd N, with $U = 5.0$, $\varepsilon_d = -0.55$, $V = 0.35$. We kept up to $m = 1700$ states. The Gaussian broadening is $\sigma = 0.05$. The height of the Kondo peak, H_K, increases when the system gets larger and finally converges for large systems.

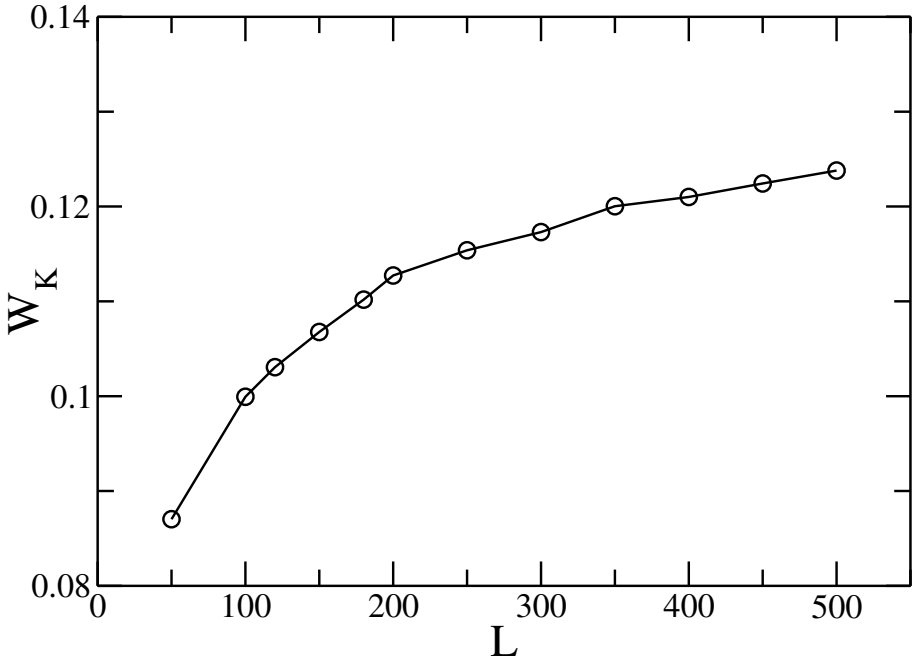

Figure 3.20: W_K vs L for odd N, with $U = 5.0$, $\varepsilon_d = -0.55$, $V = 0.35$. We kept up to $m = 1700$ states. W_K is obtained by summing over all weights in between $\omega \in [-0.2, 0.35]$.

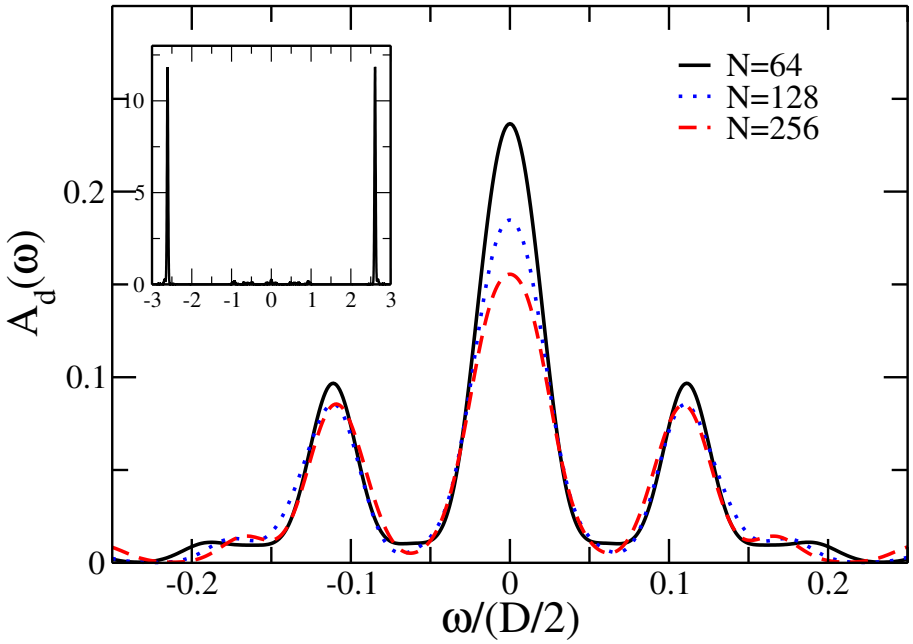

Figure 3.21: $A_d(\omega)$ for symmetric parameters, $U = 5$, $\varepsilon_d = -2.5$, $V = 0.35$ with $L = 63, 127, 255$ at half filling. The inset shows the full spectrum. Most of the spectral weight is located at the band edge. The broadening is $\sigma = 0.015$, such that the two central peaks merge.

3.3.3 Symmetric Parameters

By setting $U = -2\varepsilon_d$ the system becomes particle-hole symmetric, which results in a symmetric spectrum. We examined symmetric systems with even and odd number of particles. For an even as well as an odd number of particles, we get two peaks at distance 2μ around the Fermi edge. Since the chemical potential $\mu = E(N+1) - E(N) \neq 0$ in our finite system, there can be no peak at $\omega = 0$. The first peak in the spectral density left and right of the Fermi energy (chosen to be at $\omega = 0$) appears at $\omega = E(N+1) - E(N)$ and $\omega = -(E(N+1) - E(N))$, respectively. For half filling, $\mu_{even} < \mu_{odd}$, and the distance between the peaks is smaller for an even number of particles. The broadening of the peaks can be chosen such that the two peaks for the even case merge, and the peaks for the odd case are still separated. Although this might look like the even-odd effect predicted in [36], we consider this as fake. The only reason that there is one peak for an even number of particles and two symmetric peaks for an odd number of particles is that $\mu_{even} < \mu_{odd}$ and that the broadening σ is chosen such that the two peaks for an even N merge, and the two peaks for an odd N are still separated. We examined systems

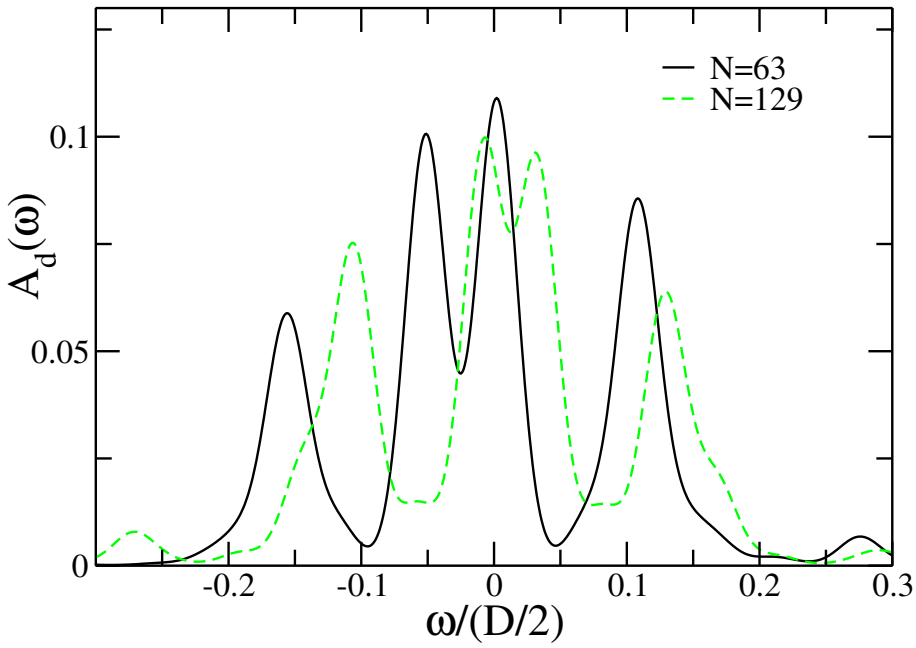

Figure 3.22: $A_d(\omega)$ for symmetric parameters, $U = 5$, $\varepsilon_d = -2.5$, $V = 0.35$ with $L = 63, 127$ with $N = 63$ and $N = 129$ respectively. We summed over both spin configurations. The broadening is $\sigma = 0.015$, such that the two central peaks merge are still separated.

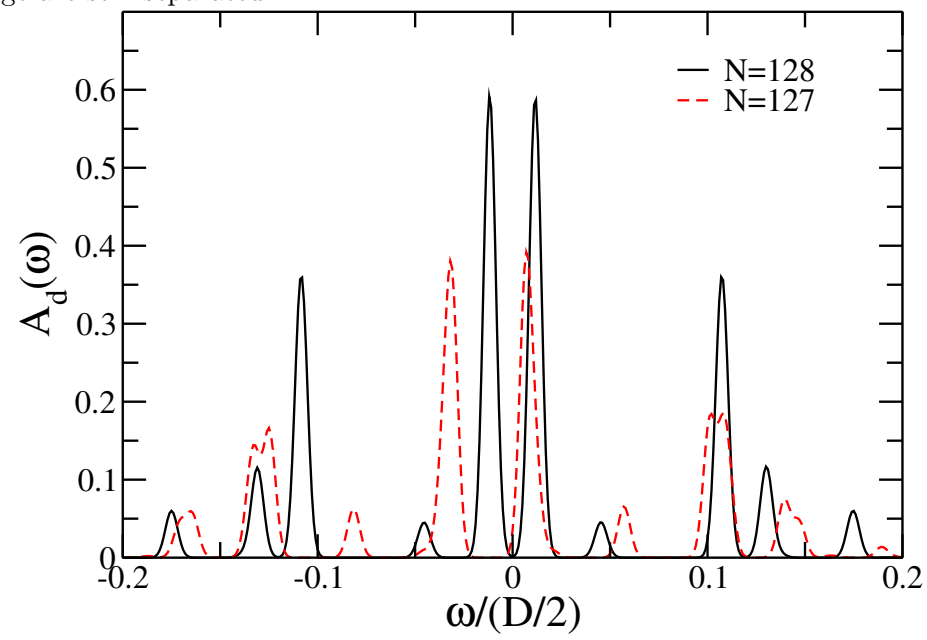

Figure 3.23: $A_d(\omega)$ for symmetric parameters, $U = 5$, $\varepsilon_d = -2.5$, $V = 0.35$ with $L = 127$ and $N = 127, 128$. We summed over both spin configurations. The broadening is $\sigma = 10^{-4}$, such that the two central peaks are still separated in both cases.

with $L = 63, 127, 255$. $N = L + 1$ (half filling) for N even which results in a symmetric spectrum and $N = L(+2)$ for N odd. The spectrums for the latter case are not symmetric. We summed over both spin configurations and chose the broadening $\sigma = 0.015$. To show that there are two central peaks even for the case when N is even, we reduced the broadening to $\sigma = 10^{-4}$ in Fig. 3.23.

3.4 Spin-Spin Correlations

3.4.1 Introduction and Measurements

One of the most interesting issues in the Kondo physics is the existence and behavior of the so-called Kondo screening cloud [37, 39]. One expects an electron in an extended wave function with a size

$$\xi = v_F/T_K \tag{3.5}$$

(the Kondo length scale) to surround the impurity and build a singlet with the impurity spin. The other electrons in the system do not see the impurity spin at low energies. We are especially interested in the size of the Kondo screening cloud in a finite system, the Kondo box. What happens, when the screening cloud is larger than the system size, $\xi > L$? To get an estimate of the Kondo screening cloud, we measure the Spin-Spin correlation function

$$K(x) = \langle S^z_{imp} S^z_x \rangle - \langle S^z_{imp} \rangle \langle S^z_x \rangle, \tag{3.6}$$

where S^z_{imp} denotes the z-component of the spin on the impurity and S^z_x the z-component of the spin at site x.
Since we work within a finite system with a fixed number of particles N and fixed S_z^{total}, we can use the following relation to see if the results obtained from the DMRG are accurate.

$$\begin{aligned}
& \sum_x \langle S^z_{imp} S^z_x \rangle - \langle S^z_{imp} \rangle \langle S^z_x \rangle + \langle S^z_{imp} S^z_{imp} \rangle - \langle S^z_{imp} \rangle \langle S^z_{imp} \rangle \qquad (3.7) \\
= & \sum_x \langle S^z_{imp} (S^z_x + S^z_{imp}) \rangle + \langle S^z_{imp} \rangle \langle S^z_x + S^z_{imp} \rangle \\
= & \sum_x \langle S^z_{imp} S^z_{total} \rangle - \langle S^z_{imp} \rangle \langle S^z_{total} \rangle \\
= & \sum_x S^z_{total} \langle S^z_{imp} \rangle - S^z_{total} \langle S^z_{imp} \rangle \\
= & \; 0
\end{aligned} \tag{3.8}$$

We kept enough states such that

$$\sum_x \langle S^z_{imp} S^z_x \rangle - \langle S^z_{imp} \rangle \langle S^z_x \rangle + \langle S^z_{imp} S^z_{imp} \rangle - \langle S^z_{imp} \rangle \langle S^z_{imp} \rangle \leq 10^{-6}. \quad (3.9)$$

Another problem in the DMRG calculation can be the following issue: If V gets too small, the spin symmetry on the impurity gets broken, and $S^z_{imp} \neq 0$ (even if $S^z_{total} = 0$) and the system runs into a non-physical state. It is a common problem that symmetries get broken in DMRG. One can keep track of spin-flip symmetry explicitly, and that will fix it, but it is not recommended. The easiest thing is just to average at the end over the measurements with their spin flip. One can then check the accuracy of this as a function of m, the number of states kept. In the large m limit, it doesn't do anything, but for small m it should converge faster. Why does it happen? The energy is lower in the system by breaking the symmetry, for finite m. So it is unstable with respect to the broken symmetry, and small numerical errors will drive it to the broken symmetry state [40]. We kept enough states in our calculation such that $S^z_{imp} < 0.002$.
We have seen in the previous section that we can not apply the standard formulas of Kondo physics to our problem. Another main difference is the following: Since we work within the canonical ensemble with fixed particle number and spin, the impurity spin is *always* fully compensated in the system. Thus, we cannot measure ξ by determining the site at which the impurity spin is fully compensated. For a finite system, $\xi = L - x_0$. Thus, we have to think of another way how to get an estimate of the size of the Kondo screening cloud.

3.4.2 First Insight for Different System Sizes

We first looked at a SIAM with $L = 111$ chain sites, $U = 5$, $\varepsilon_d = -0.55$, $N = 112$, $S^z_{total} = 0$, tuned the Kondo temperature by varying over different V and measured $K(x)$. We have plotted the results in Fig. 3.24 and Fig. 3.25. We can see the typical oscillations with frequency $2k_F$. The amplitude of the oscillations decreases when the distance to the impurity increases. In addition, the amplitudes are unequal for different V. One can see that for larger V the correlations are stronger in the nearest region around the impurity, and much more of the impurity spin is compensated locally. The amplitude decays faster for increasing distance to the impurity, too. This is a first sign of the expected behavior. In (3.5) we see that the size of the Kondo cloud ξ is reduced when the Kondo temperature is increased. By increasing V, the Kondo temperature is increased, too, and is therefore leading to a

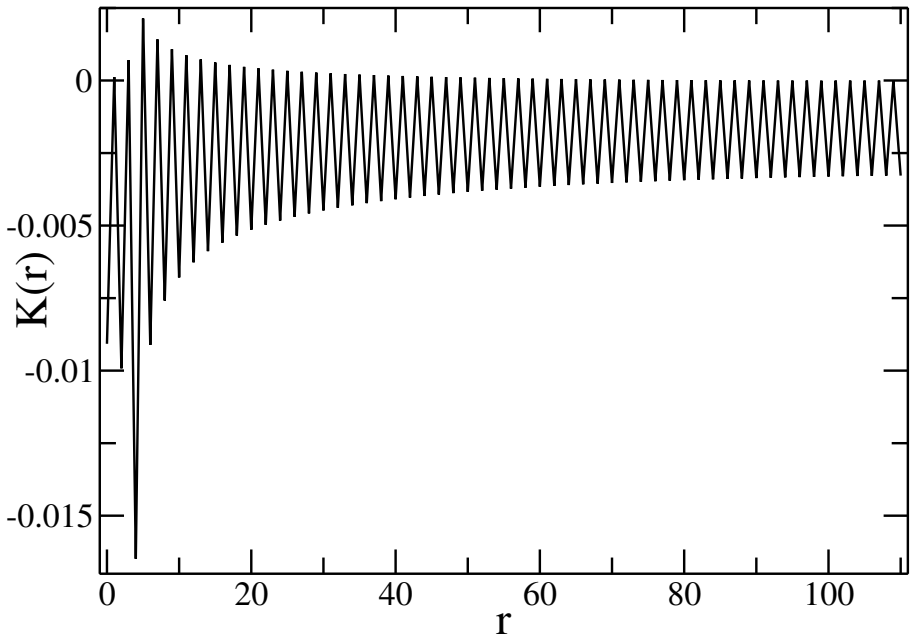

Figure 3.24: $K(x)$ for a system with $L = 111$, $U = 5$, $\varepsilon_d = -0.55$, $V = 0.2$, $N = 112$, $S^z_{total} = 0$, $x_0 = 4$.

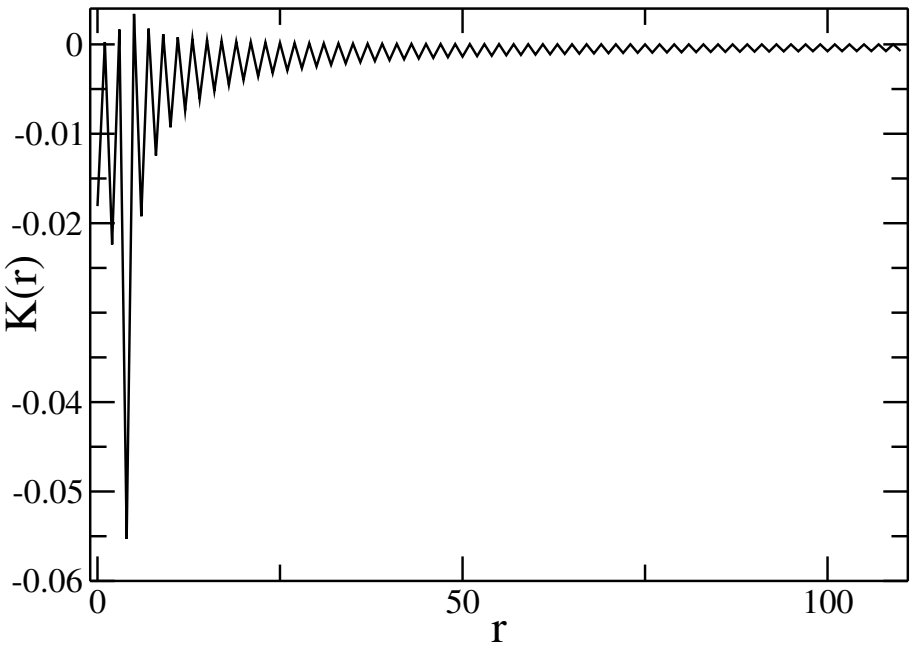

Figure 3.25: $K(x)$ for a system with $L = 111$, $U = 5$, $\varepsilon_d = -0.55$, $V = 0.4$, $N = 112$, $S^z_{total} = 0$, $x_0 = 4$.

smaller ξ. Actually, one has to distinguish between the size of the Kondo cloud ξ and the correlation length l_k. Since

$$l_k = \left(\frac{\xi}{k_F^{d-1}} \right)^{1/d}, \tag{3.10}$$

with the dimension d, $\xi = l_k$ in our 1D Kondo box. To get a better insight we now look at the average correlation function of two neighboring sites as a function of the distance to the impurity:

$$C(r) = \left(K(x) + K(x+1) \right) /2, \tag{3.11}$$

with $r = |x - x_0|$. In the standard SIAM, one can show that the correlations are given by the following equation:

$$C(r) = D \cdot (A/r + B) \exp(-r/l_k). \tag{3.12}$$

Although we can not apply this formula to our problem, we can look at the behavior of the the spin-spin correlation. $C(r)$ is supposed to show a linear decrease for $r < l_k$ and to decrease exponentially for $r > l_k$. Hence, we look if we can find a region where $C(r) \sim 1/r$ or $C(r) \sim \exp(-\alpha r)$. In Fig. 3.26 we can see $C(r)$ for different Kondo temperatures. One can see one main difference: The curves with $V < 0.4$ unlike the curves with $V \geq 0.4$ inhibit an inflection point for large r (small $1/r$). It is not easy to add a linear fit to each curve. We know that the curve should show linear behavior for small r (large $1/r$), so we tried to fit for $1/r = 0.1$ down to $1/r = 0.02$ and looked how the fit behaves for larger r. One can see that a linear function is a good approximation for $V = 0.4$ up to large distances, hence we expect the correlation length l_k to be of the same order as the system size L, and therefore $l_k \sim L$. By increasing V, l_k is supposed to decrease. We can see that the curve for $V = 0.5$ leaves the linear behavior much sooner as for $V = 0.4$, exactly as we expected. Actually, the linear fit for $V = 0.5$ is a poor approximation. But what happens for $V = 0.3$? We think that for this case, $L < l_k$, such that the Kondo cloud can not be build. The switch to an exponential decay for large r is purely a finite size effect: Since we work within a canonical ensemble, the impurity spin is always fully compensated. Trying to fit a curve like (3.12) is possible, but gives unreasonable results for l_k, since all four parameters are tuned. In addition, we emphasize again that we can not apply most of the formulas of the standard Kondo cloud, because of the following differences: We have to cope with a non-flat conduction band, the impurity couples only to one site of the band, and we have finite size effects. The last point is probably the most influencing issue. Hence,

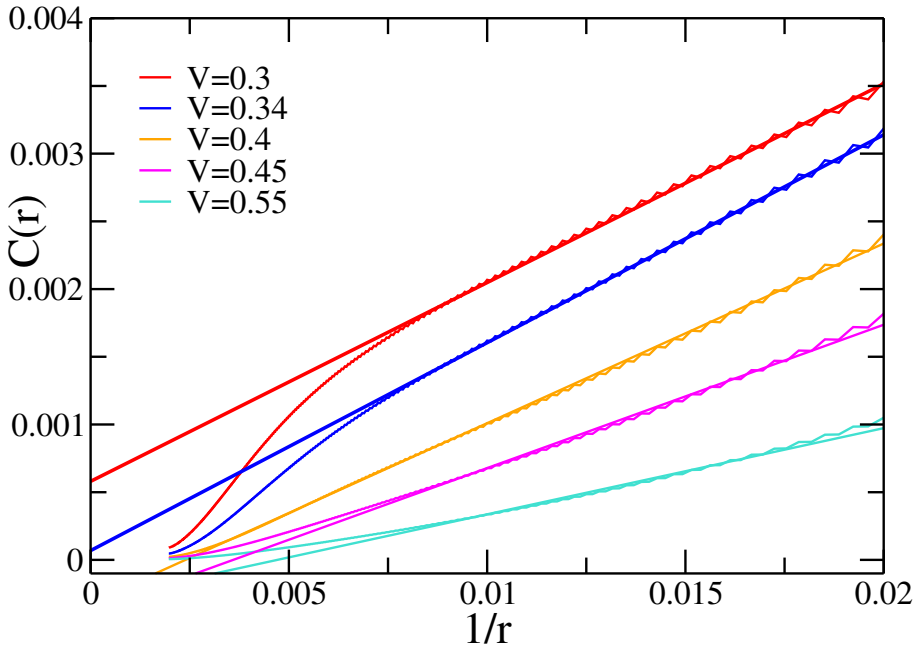

Figure 3.26: $C(r)$ vs. $1/r$ for a system with $L = 511$, $U = 5$, $\varepsilon_d = -.55$, $N = 512$, $S^z_{total} = 0$, $x_0 = 4$. The order of the legend matches the order of the graphs.

the only striking difference we can see in the spin-spin correlation function is the inflection point for small Kondo temperatures.
An interesting issue is the behavior of the Kondo cloud when the system size is increased. In the previous section we have seen that the spectral density does not change when there is an even number of particles N in the system and the Kondo temperature is sufficiently large. Another question is, what happens when $l_k > L$? If $l_k < L$, the Kondo cloud should not change if the system is increased. Theory predicts that electrons outside the Kondo cloud do not see the impurity spin at low energies. We looked at system with different L from 111 sites to 511 sites, half filling (N even), $U = 5$, $V = 0.4$, $\varepsilon_d = -0.55$ and $x_0 = 4$. We have plotted $C(r)$ for small and large r in Fig. 3.27 and Fig. 3.28. One can see that for small r, the correlation functions for the larger systems give the same results. One can see that for systems with $L = 211$ to 511 sites, $C(r)$ is almost identical for small r. By increasing r, $C(r)$ of the smaller systems *leaves* the main curve ($C(r)$ for $L = 511$) at a specific r_0. This is a finite size effect. The Kondo cloud cannot fully develop in the finite system, but the impurity spin has to be compensated. Thus, the correlations can not decrease that strong at the end of the system. The correlation functions for the two largest systems are almost identical for the

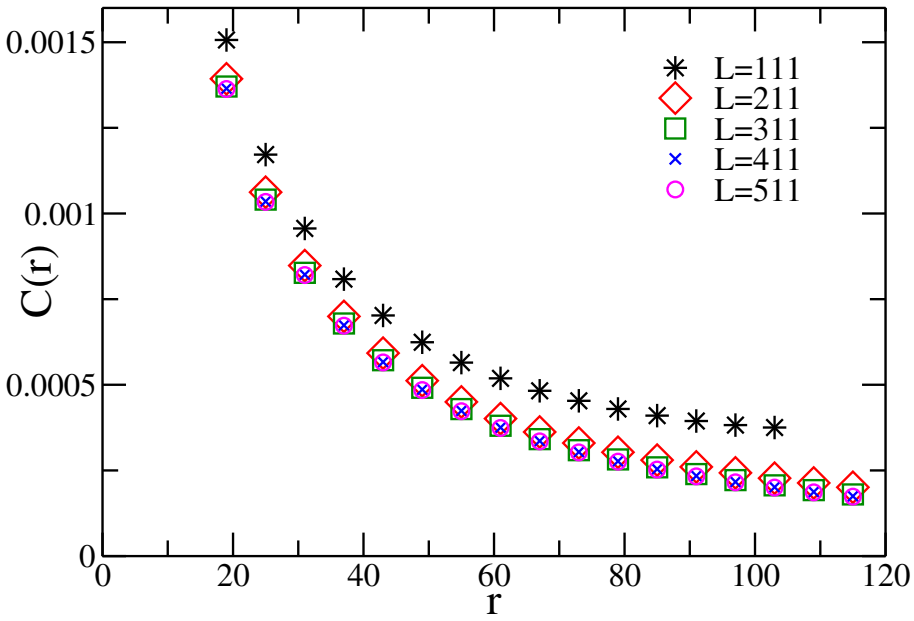

Figure 3.27: $C(r)$ for different L, $U = 5$, $V = 0.4$, $\varepsilon_d = -0.55$ and $x_0 = 4$. We kept $m = 1000$ states, such that $\langle S^z_{imp} \rangle \sim 10^{-5}$. For small r, $C(r)$ for larger systems are almost identical.

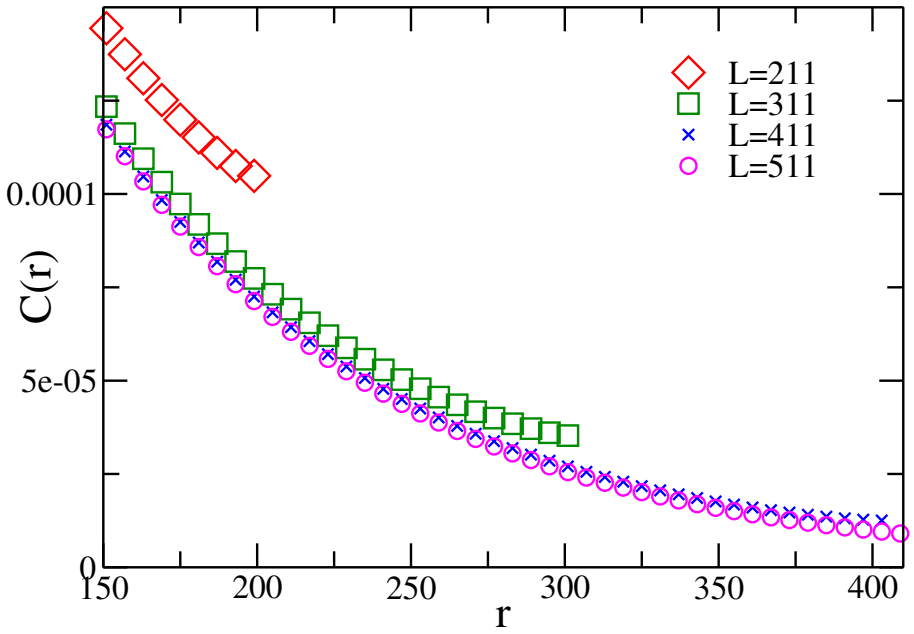

Figure 3.28: $C(r)$ for different L, $U = 5$, $V = 0.4$, $\varepsilon_d = -0.55$ and $x_0 = 4$. We kept $m = 1000$ states, such that $\langle S^z_{imp} \rangle \sim 10^{-5}$. Every 5^{th} data point is shown. $C(r)$ for $L = 411$ and $L = 511$ is almost identical until $r \sim 300$.

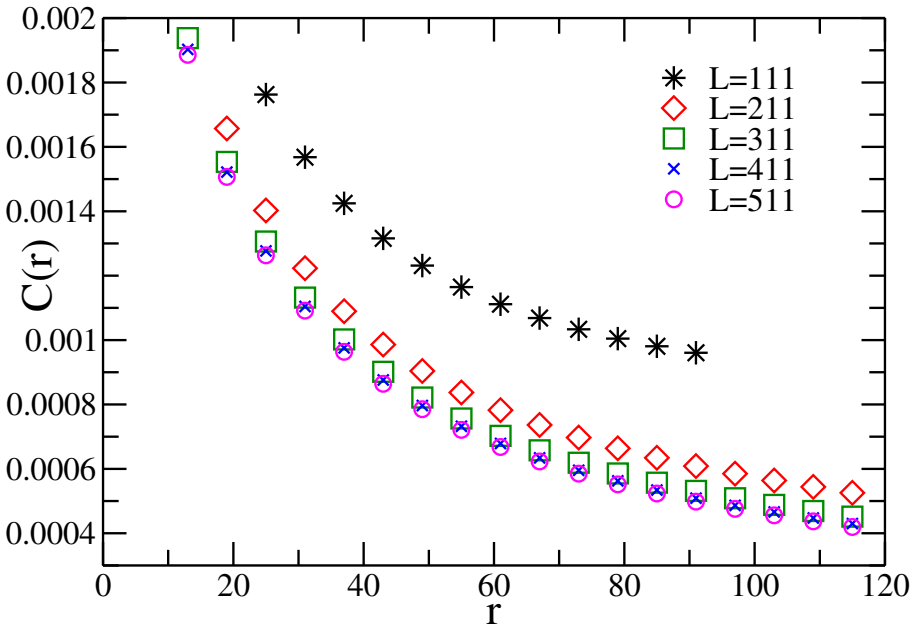

Figure 3.29: $C(r)$ for different L, $U = 5$, $V = 0.3$, $\varepsilon_d = -0.55$ and $x_0 = 4$. We kept $m = 1000$ states, such that $\langle S^z_{imp} \rangle \sim 10^{-5}$. For small r, $C(r)$ for larger systems are close, but not identical.

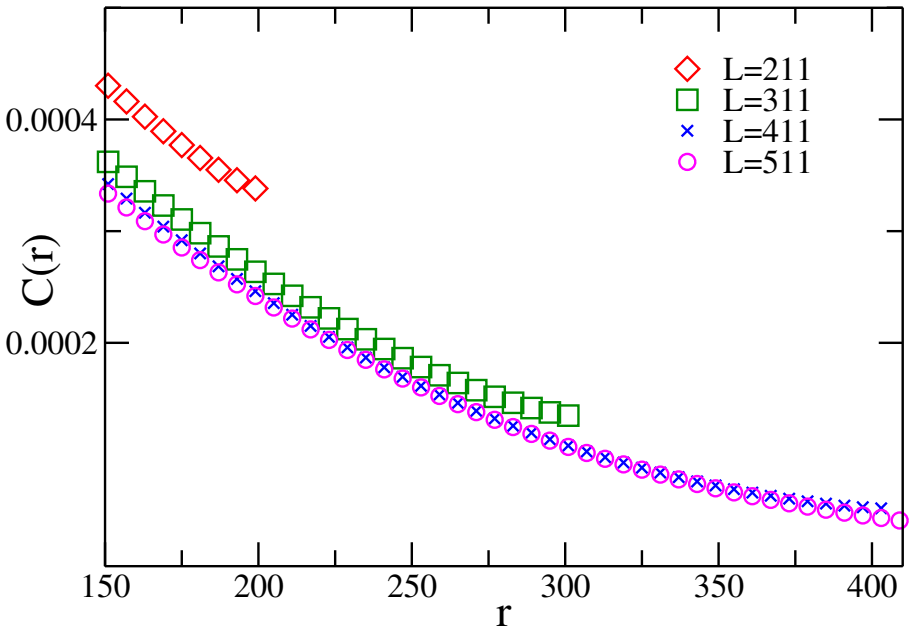

Figure 3.30: $C(r)$ for different L, $U = 5$, $V = 0.3$, $\varepsilon_d = -0.55$ and $x_0 = 4$. We kept $m = 1000$ states, such that $\langle S^z_{imp} \rangle \sim 10^{-5}$. Every 5^{th} data point is shown.

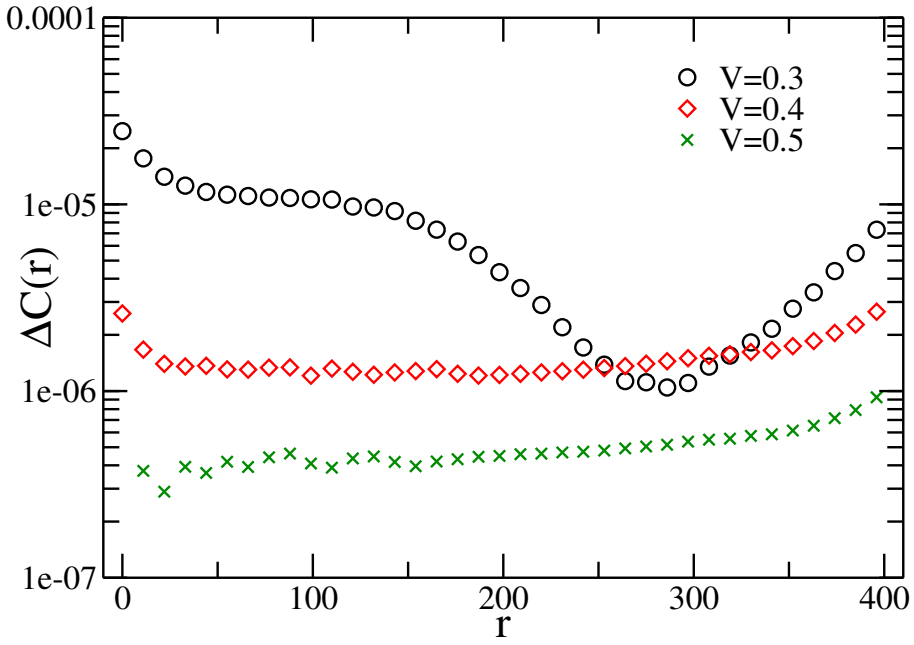

Figure 3.31: $C(r, L = 511) - C(r, L = 411)$ for different V, $U = 5$, $\varepsilon_d = -0.55$ and $x_0 = 4$. We kept $m = 1000$ states, such that $\langle S^z_{imp} \rangle \sim 10^{-5}$. Every 10^{th} data point is shown. The deviations increase by decreasing V.

whole system. This means that for $L \sim 411$, the Kondo cloud is already fully developed, and thus $l_k < L$.
Next, we decrease the Kondo temperature and thus increase l_k. In Fig. 3.29 and Fig. 3.30, we have set $V = 0.3$. For small r, one can see that the deviations between the correlation functions for different system sizes are larger for smaller V. For large r, both plots do not seem to differ much, but only due to the different scale chosen on the y-axis. To compare the long range behavior, it is good to look at the difference $|C(r, L = 511) - C(r, L = 411)|$ for different V. In Fig. 3.31 one can see that the deviations increase with increasing l_k, just as expected.

3.4.3 Determining l_k^{num}

We already know that we can not apply the usual formulas of Kondo physics. These formulas are derived for infinite systems with a flat conduction band a non-local impurity coupling. Nevertheless, we found similarities for the spectral densities and the Kondo screening cloud of the Kondo box and the standard systems. For a 1D system, the spin correlations are expected to decay $\sim 1/r$ until l_k and then decay exponentially. We have seen that there is a large region where $C(r) \sim 1/r$ for most plots, and we found that the curve enters an exponential behavior for large r for some sets of parameters. We now want to compare the correlation length that we got from our simulations, l_k^{num} with the analytical results. The question is: how do we obtain l_k^{num}? It doesn't make sense to fit the formula of the analytical approach to get l_k^{num}. Hence, we decided to choose l_k^{num} to be the distance r, where 3/4 of the impurity spin is compensated. This seemed reasonable: It's not good to choose the site where 1/2 of the impurity spin is compensated, because this is just a few sites for most of the systems. It would also not be clever to choose the site where ~ 0.95 of the impurity spin is compensated. In this case, one had to sum over too many spins with a very small correlation, thus increasing the numerical error. The main problem is that since the impurity spin is always fully compensated within the system, $l_k^{num} < L$ for all sets of parameters. In Fig. 3.32 we can see the numerical as well as the analytical correlation lengths. The results are obtained for a system with $L = 511$, $U = 5$, $\varepsilon_d = -0.55$ and $x_0 = 4$. One can see good agreement for large V and and overall similar behavior for $V \to 0.3$. For $V < 0.28$, the analytical Kondo temperature is 0 (or not defined anymore). For $V < 0.3$, the DMRG calculations run into a non-physical state with broken symmetry. The smallest V we can calculate for 511 sites is $V = 0.29$, where $\langle S^z_{imp} \rangle \leq 0.001$ and the sum over all spins ≤ 0.0003. In Fig. 3.33 we have plotted l_k^{num} versus the system size L for different V. For $V = 0.5$, l_k^{num} is the same for all system

sizes. After 12 sites, 3/4 of the impurity spin is compensated, independant of the system size. For $V = 0.4$, l_k^{num} for systems with $L \geq 211$ is identical. For smaller V, one can see that l_k^{num} increases with increasing system size and converges for large systems. The larger the hybridization V — and hence the larger T_K —, the sooner l_k^{num} converges.

3.4.4 The Even-Odd Effect for Spin-Spin Correlations

Up to now, we only looked at spin-spin correlations for systems with an even number of particles N. From the calculation of the spectral densities we know that there can be strong differences in the behavior of the system properties when the number of particles is even or odd. We start with looking at Fig. 3.34, where we have plotted $C(r)$ for systems with $L = 100$ up to $L = 500$ with an odd number N of particles. One can see two main differences between this and the plots where N is even. The spin correlations for an odd N decrease for smaller systems, whereas they increased when N is even. In addition, $V = 0.35$ is large enough that the spin correlations are almost equal for small distances when N is even, whereas they differ when N is odd. We already know that spin flip transitions are less favourable when N is odd. The additional energy that has to be paid to lift one electron to a next higher-lying level decreases for increasing system size. This affects the occupation number of the impurity. For $V = 0.35$, $n_d = 0.912$ when N is even for $L = 51$ up to $L = 511$. When N is odd, $n_d = 0.9026$ for $L = 500$ and $n_d = 0.717$ for $L = 100$. This leads directly to another impurity spin that has to be compensated. If N is even and $V = 0.35$, $\langle S_{imp}^z S_{imp}^z \rangle$ is about the same for all calculated systems (because n_d is equal for all systems). Hence, the same impurity spin has to be compensated in the whole system. Since the average impurity spin compensation per site is smaller for smaller systems, it makes perfect sense that the correlations are larger (or equal) for smaller systems. If N is odd, the smaller the system the less impurity spin has to be compensated. Thus, the spin correlations are small for small systems. We also saw that the weight (or height) of the Kondo peak increases with the system size and finally converges for large systems when N is odd. We seem to observe a similar effect for the spin correlations at small distances. The difference in $C(r)$ decrease for larger systems. Our final goal is to find a connection between the spectral density (which is easy to measure) and the spin-spin correlations. Therefore, we look at the numerical correlation length and compare the result with the weight of the Kondo peak. In Fig. 3.36 and Fig. 3.37 we have plotted the numerial l_k and the weight of the Kondo peak for different system sizes and $U = 5$, $V = 0.35$, $\varepsilon_d = -0.55$, $x_0 = 4$ and N at half filling (odd). We can see that the increase of the weight

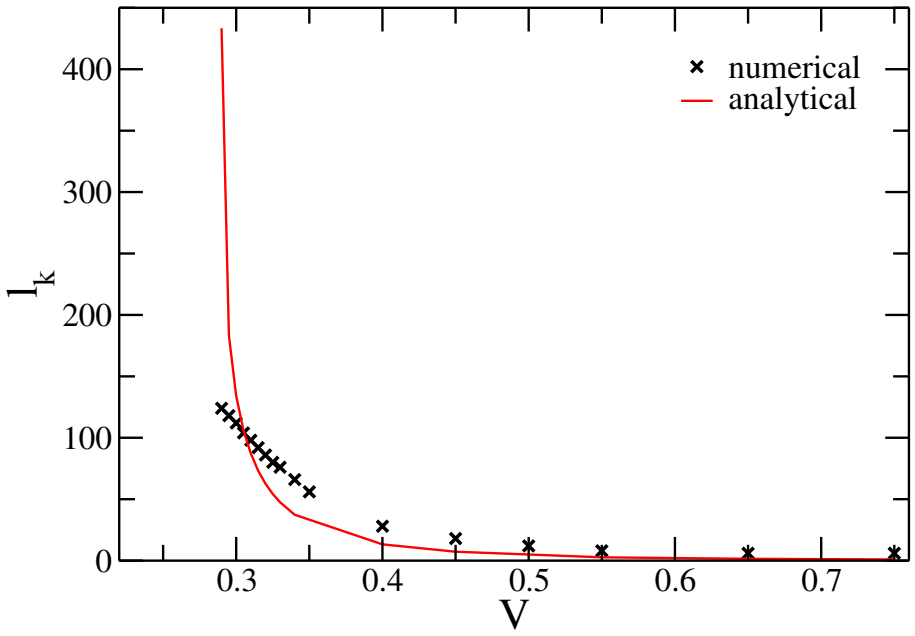

Figure 3.32: Comparison of the numerical and analytical l_k. The l_k^{num} is the site where 0.75 of the impurity spin is compensated. The system parameters are $L = 511$, $U = 5$, $\varepsilon_d = -0.55$ and $x_0 = 4$. We kept $m = 1000$ states, such that $\langle S^z_{imp} \rangle \sim 10^{-5}$. For $V < 0.28$, the anaytical Kondo temperature is 0 (or not defined anymore). For small V, the errors for the numerical calculation increase, because we run into a nonphysical state with broken symmetry.

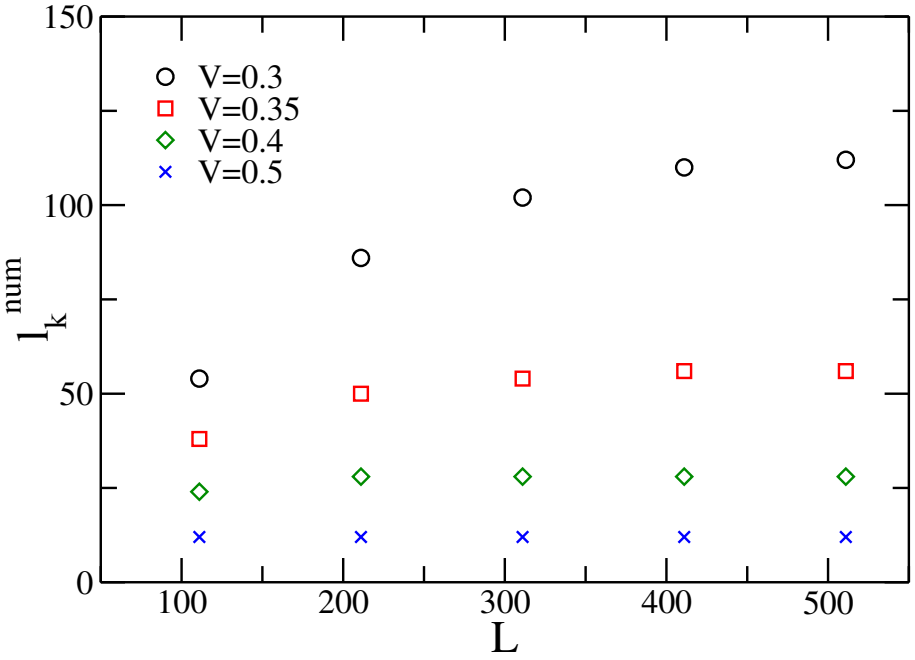

Figure 3.33: l_k^{num} versus L for different V. l_k^{num} is the site where 0.75 of the impurity spin is compensated. The system parameters are $U = 5$, $\varepsilon_d = -0.55$ and $x_0 = 4$, $S_z^{total} = 0$ and half filling (N even). We kept $m = 1000$ states, such that $\langle S^z_{imp} \rangle \sim 10^{-5}$.

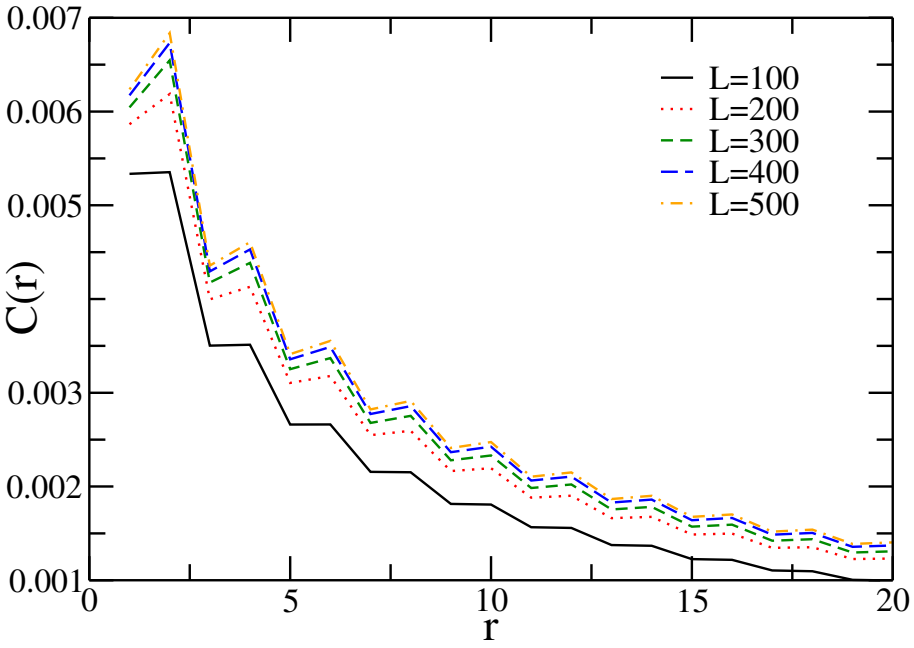

Figure 3.34: $C(r)$ for different L, $U = 5$, $V = 0.35$, $\varepsilon_d = -0.55$, $x_0 = 4$ and N at half filling (odd). We kept up to $m = 1500$ states.

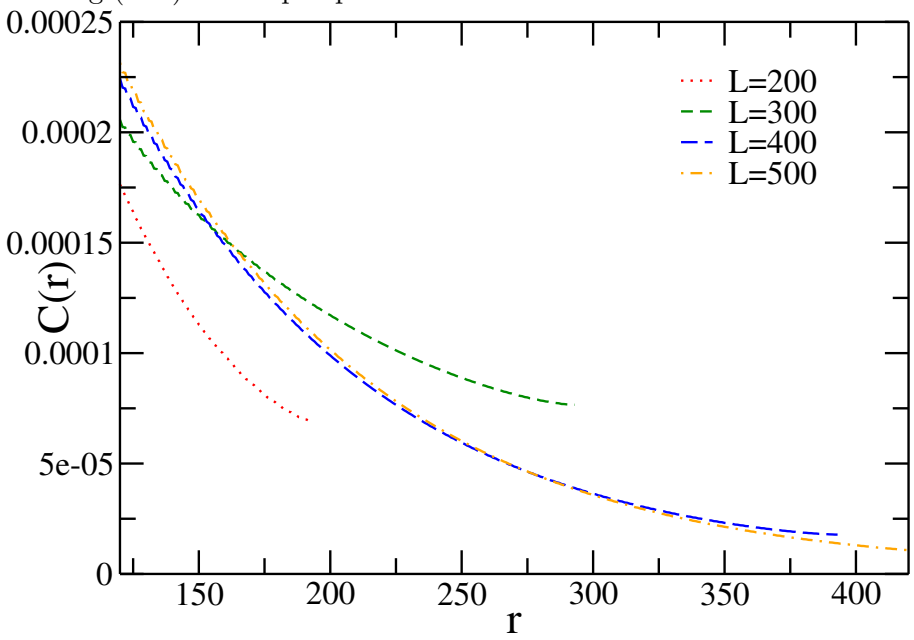

Figure 3.35: $C(r)$ for different L, $U = 5$, $V = 0.35$, $\varepsilon_d = -0.55$, $x_0 = 4$ and N at half filling (odd). We kept up to $m = 1500$ states.

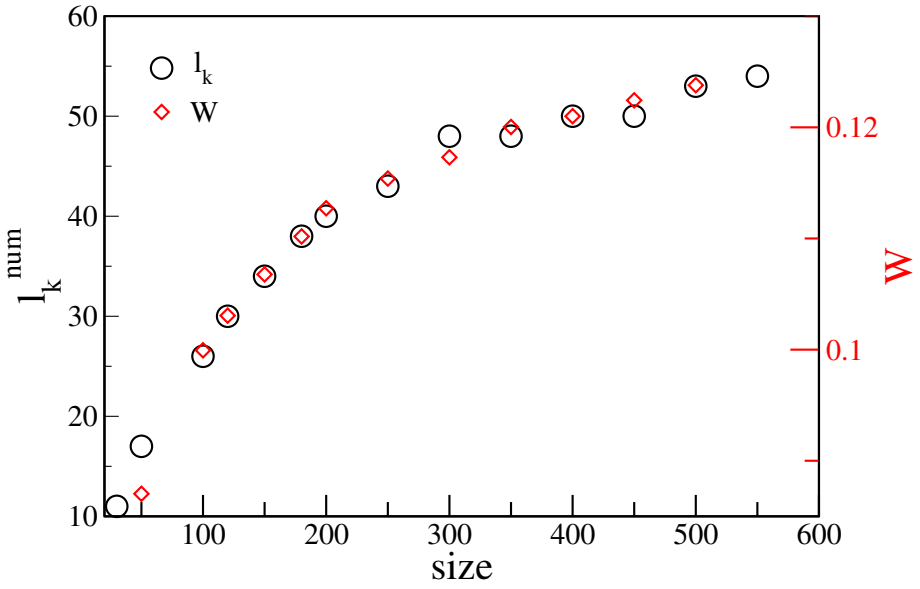

Figure 3.36: Comparison of l_k^{num} and W for N odd for different L. The other system parameters are $U = 5$, $V = 0.35$, $\varepsilon_d = -0.55$, $x_0 = 4$ and N at half filling (odd). We kept up to $m = 1500$ states. l_k is the site where 0.75 of the impurity spin is compensated.

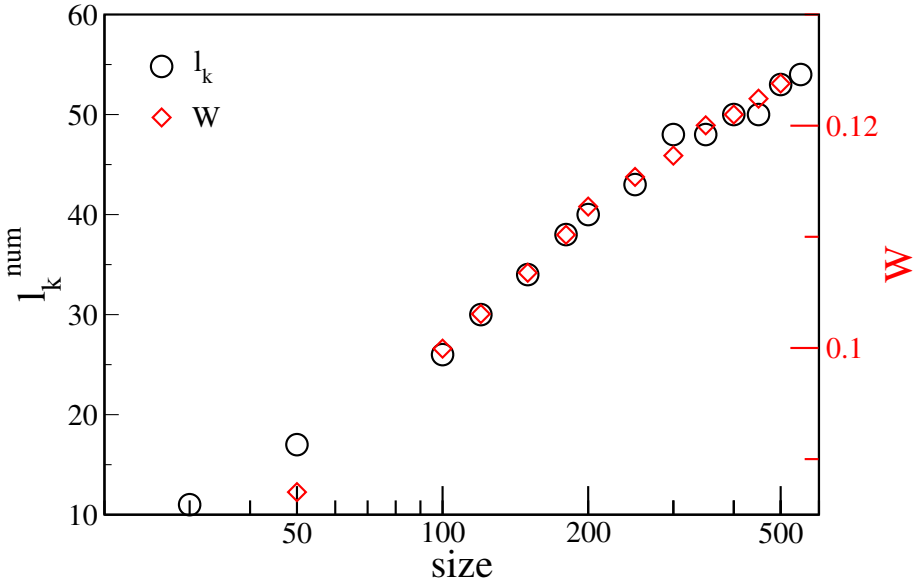

Figure 3.37: Comparison of l_k^{num} and W for N odd for different L. The other system parameters are $U = 5$, $V = 0.35$, $\varepsilon_d = -0.55$, $x_0 = 4$ and N at half filling (odd). We kept up to $m = 1500$ states. l_k is the site where 0.75 of the impurity spin is compensated.

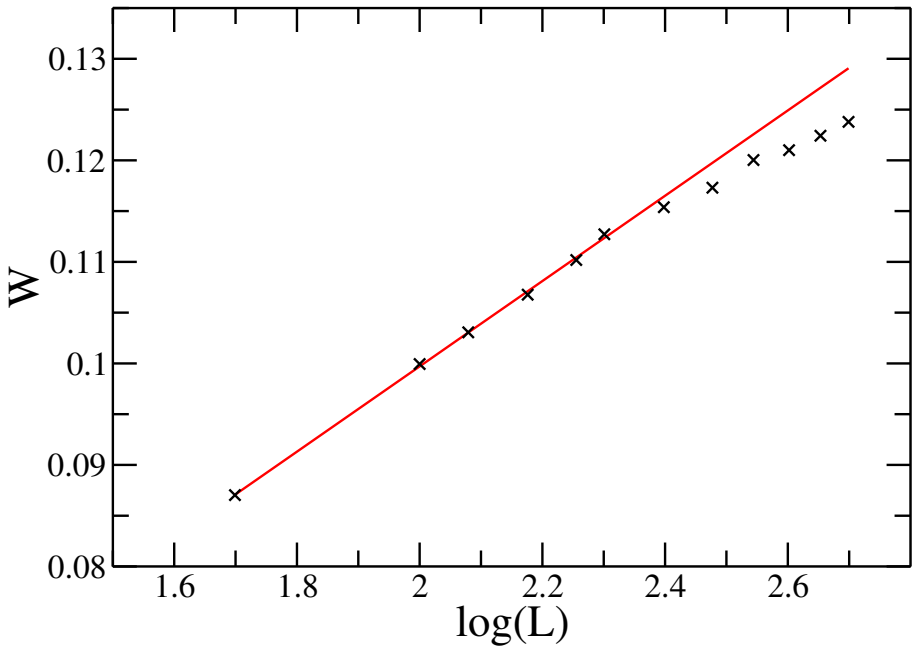

Figure 3.38: Weight of the Kondo peak W for N odd and different L with a linear fit function. The other system parameters are $U = 5$, $V = 0.35$, $\varepsilon_d = -0.55$, $x_0 = 4$ and N at half filling (odd). We kept up to $m = 1500$ states.

in the Kondo peak by increasing the system size matches the increase of the numerical l_k. In Fig. 3.36 we can see that both values increase and finally converge for larger systems. In Fig. 3.37, we have plotted the system size on a logarithmic scale. We can see that the increase is linear for W and for l_k^{num} when we neglect the region for very small systems ($L < 100$). To see if the increase of W and l_k^{num} is also logarithmic for large system sizes, we try to fit a linear function. This is done in Fig. 3.38. One can see that the increase of W is linear until $L \sim 200$ system sites. W seems to converge for larger systems size, but we can not calculate systems where it is finally converged.

3.4.5 Conclusion of the SIAM Results

We have presented DMRG calculations of the spectral density on the impurity and spin-spin correlations for a Single Impurity Anderson Model for systems of up to 511 lattice sites. We found that the spectral density is stronlgy dependent on the position of the impurity x_0. The higher the local density of states at site x_0, the more states can interact with the impurity and the higher the Kondo peak. Although we can not apply the standard formu-

las from Kondo physics to our problem due to differences in the Hamiltonian (local coupling of the impurity) and other assumptions (non-flat conduction band), we found good agreement between the estimated Kondo temperature and the height (or weight) of the Kondo peak. For an even number of particles in the system we also found that the shape of the Kondo peak does not depend on the size of the system as long as the local density of states at site x_0 is sufficiently large. If this is not given, the Kondo peak collapses for large systems. We could observe strong differences in the spectra when the number of particles in the system is even or odd. If N is odd, the double occupancy of the top most single particles level enforces one electron to move to the next higher lying energy state, thus reducing the energy gain from spin flip transition. Hence, the height of the Kondo peak is smaller when N is odd. One could see that the height of the Kondo peak oscillates when the number of particles changes between even and odd. This could be used as a signature for experiments. Unlike the spectra for even N, the height of the Kondo peak increases when the system size is increased for odd N. The energy that one has to pay to lift one electron to the next higher lying level decreases with the increasing system size and finally converges. Hence, the height of the Kondo peak also converges for large systems.
By measuring the spin-spin correlation function of the impurity spin and the spin on the conduction band we could get an insight in the Kondo screening cloud. We found differences in the behavior of the correlations when N is even or odd, too. When N is even, the higher the Kondo temperature, the more of the impurity spin is compensated in a smaller region near the impurity. We could find regions where the correlation function $C(r) \sim 1/r$ and where $C(r) \sim \exp(-r)$. When the Kondo temperature is high, the correlations do not change for a large region around the impurity. The higher T_K, the better the match of correlation functions of different system sizes. We defined the numerical correlation length by the site where 0.75 of the impurity spin is compensated. Although this means that l_k^{num} is always within the system, we could find resemblance to the theory. By increasing the system size, l_k^{num} increases and finally converges. The higher the Kondo temperature, the sooner l_k^{num} converges. If the numerical l_k does not change anymore by increasing the system size, the impurity spin is fully compensated within the system, and $l_k^{num} < L$.
If N is odd, we found that the correlation function decreases for smaller system. Since spin-flip transitions are reduced for smaller systems, n_d, the electron number on the impurity, is reduced, and a smaller impurity spin has to be compensated. For an even N, n_d is nearly constant for different L. In addition, we found that the correlation functions for an odd N and for different L do not match anymore, although they become more similar when

we reach system sizes of ~ 500 lattice sites. We found a connection of the height of the Kondo peak and the numerical l_k for an odd N and different system sizes. Both values increase logarithmically for intermediate system sizes ($L < 200$) and then finally start to converge. We could not measure systems that large that l_k^{num} nor W is finally fully converged. The most interesting results of this chapter are summarized in [35].

Chapter 4

Systems with Long Range Coulomb Interaction with DMRG

The Hamiltonian for a 1D Hubbard chain including long range Coulomb interactions can be written as:

$$\begin{aligned} H &= -t \sum_{i,\sigma} c^{\dagger}_{i,\sigma} c_{i,\sigma} + \text{h. c.} \\ &+ U \sum_{i} n_{i,\uparrow} n_{i,\downarrow} \\ &+ \sum_{i \neq j} V_{i,j} n_i n_j . \end{aligned} \tag{4.1}$$

The technical problem for including long range interaction in DMRG is that the number of operations increases with the square of the system size, L^2. For each application of the superblock Hamiltonian with a wavefunction, one has to apply $V_{i,j} n_{i,\uparrow} n_{j,\downarrow}$ for each site i, j of the system. In addition to this, each block has to store a lot more operators than usual. If we consider the same Hamiltonian without long range interaction, one has to keep track of only the operators on the edge of the system and the Hamiltonian of each block. In this example this is only 5 operators for each block, the Hamiltonian and $c^{(\dagger)}_{\uparrow,\downarrow}$. If we exploit that c is the hermitian conjugate of $c^{\dagger}$, then we need only 3 operators per block. In addition, the number of operations needed for $H \cdot \Psi$ is constant. For long range interaction, the usual strategy is to reduce the growth of operations from L^2 to L. The key trick is to build the operator

$$\hat{V}_r = \sum_{l} V_{l,r} \cdot n_l \tag{4.2}$$

for each site r on the right block and site l on the left block. Now, the long range part of the Hamiltonian can be rewritten as

$$\sum_{i \neq j} V_{i,j} n_i n_j = \sum_r \hat{V}_r n_r \tag{4.3}$$

and the number of operations grows linearly with L. This *trick* was first used by Xian [41] and is called concept of composite operators.

4.1 Hubbard Ring

Our goal was to calculate the particle and hole density on a t-J ladder with 16×2 sites and 2 to 6 holes. To check the implementation, we first compared results for a Hubbard ring with [42]. The Hamiltonian is given by:

$$H = -t \sum_{i,\sigma} \left(c^\dagger_{i,\sigma} c_{i+1,\sigma} + h.c. \right) + \frac{U}{2} \sum_{i,j} \frac{n_i n_j}{1 + \gamma d_{ij}}. \tag{4.4}$$

Since we consider a ring, the distance is defined as

$$d_{ij} = \frac{\sin(i-j)\frac{\pi}{L}}{\sin \frac{\pi}{L}}, \tag{4.5}$$

γ controls the strength of the Coulomb repulsion is set to $\gamma = 1.053907$, the other parameters are $U/t = 13.55$ and filling $\bar{n} = 3/4$. We are interested in the charge structure factor

$$R(q) = \frac{1}{L} \sum_{l,m} e^{iq(l-m)} \langle (n_l - \bar{n}) (n_m - \bar{n}) \rangle, \tag{4.6}$$

and the spin structure factor

$$S(q) = \frac{1}{L} \sum_{l,m} e^{iq(l-m)} \langle S^z_l S^z_m \rangle. \tag{4.7}$$

Both quantities are plotted in Fig. 4.1 and Fig. 4.2. Since we calculated this quantities only to compare with previous results, we will not comment or explain them.

4.2 $t - J$ Ladder

Much of the interesting physics of high T_C superconductors is local on a length scale of the superconducting coherence ξ_0, which is typically a few

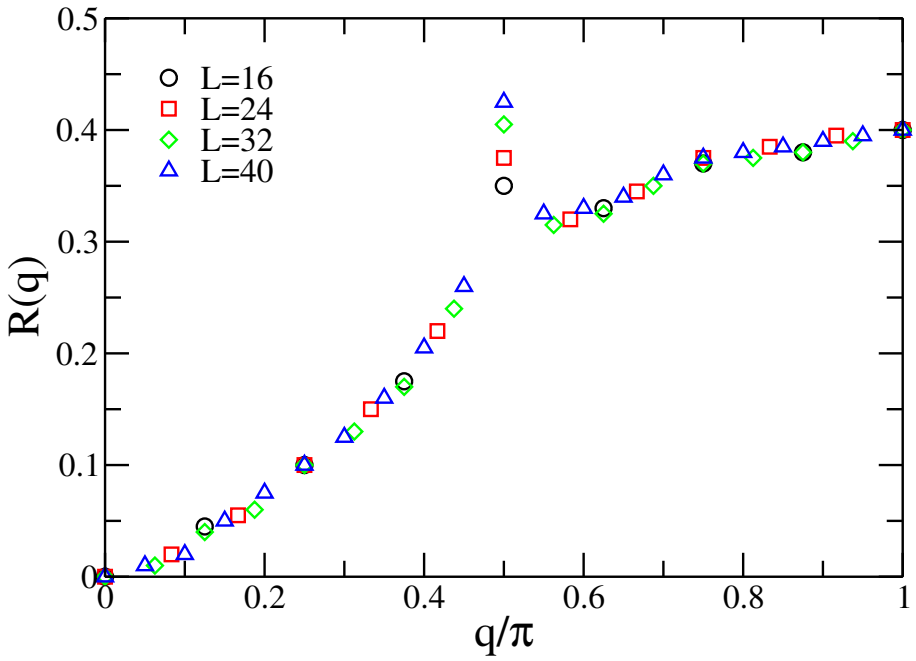

Figure 4.1: The charge structure factor for a Hubbard ring with different size L, filling $\bar{n} = 3/4$ and $U/t = 13.55$. We can see a peak $q = 0.5\pi$, which corresponds to $k_F = 3\pi/8$.

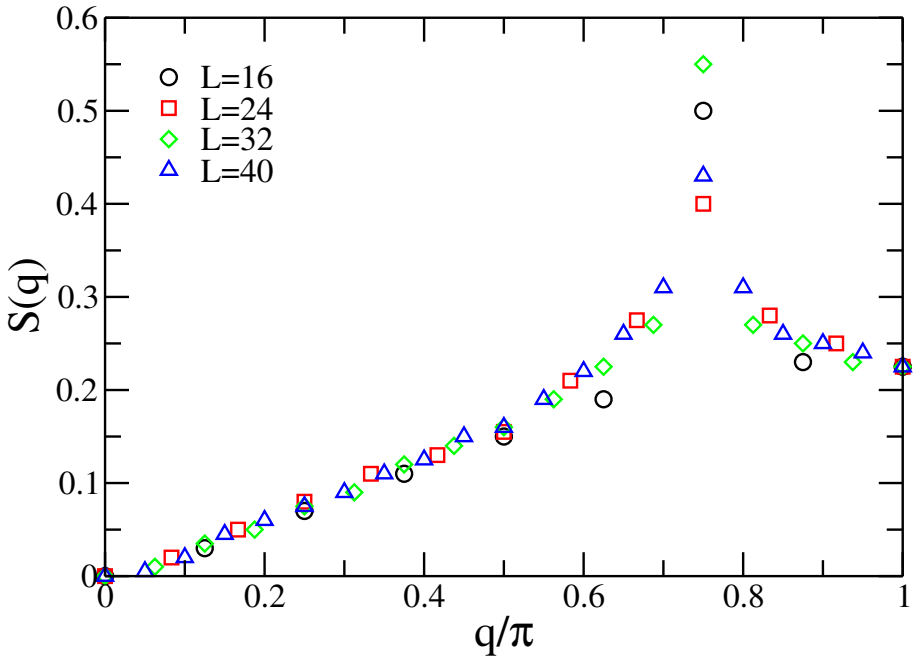

Figure 4.2: The spin structure factor for a Hubbard ring with different size L, filling $\bar{n} = 3/4$ and $U/t = 13.55$. We can see a peak $q = 0.5\pi$, which corresponds to $k_F = 3\pi/8$.

lattice constants. Studies of t-J systems have provided strong evidence of a robust d-wave character of local pairing correlations, and of a strong clustering tendency of holes which might lead to stripes or phase separation [43]. However, most studies for the t-J model have failed to find evidence of the strong superconducting correlations needed to understand high T_C superconductivity. All these calculations omit the long-range part of the Coulomb interaction. In [43], various t-J lattices are measured, where the DMRG is used to calculate the short range interaction, and the long-range interaction is taken into account within a Hartree approximation. Our goal was to proof the results, while including the long-range interaction into the DMRG. But first, we examine the hole density for a 16×2 t-J ladder. We use open boundary conditions, $J/t = 0.35$ and 2 - 6 holes. One problem in this setup is the boundary condition: Due to the long range coulomb repulsion, the electrons would move to the edge, and holes would not repel each other. Since this effect comes only from the open boundary conditions, we introduce a chemical potential on each site

$$\mu_i = \sum_{i \neq j} \frac{\bar{n} V}{|i - j|}.$$

This makes sites in the middle of the chain more favorable for the electrons and equalizes the effect, that sites at the end of the chain have a larger distance to the other sites in the system. We have plotted our results in Fig. 4.3 - 4.5.

2 holes: One can see that by turning off V, the holes are in a *particle-in-a-box*-like state. By turning on the Coulomb repulsion V, the holes start to repel each other. For $V = 0.6$, one can see that two stripes are generated. For larger V, both holes are located at rung 3-4 and rung 12-13.

4 holes: One can see two pairs of holes for $V = 0$. As before, the pairs break up by increasing V. It takes a stronger long range repulsion to break up to pairs. For two holes, the pairs brake up for $V \approx 0.6$, whereas for 4 holes, it takes $V \approx 0.8$ to break up both pairs. This effect increases when we look at 6 holes: Three pairs are located at even distances. It takes much more energy ($V \approx 3.0$) to break up all three pairs.

There are much more things one should measure, like the spin gap $E_{S=1} - E_{S=0}$. The pair binding energy $E_{N+2} + E_N - 2E_{N+1}$ would also give more insight how the pairs behave and break up. The pair-pair correlation could be used to probe superconductivity.

The work in this chapter was done in collaboration with Prof. S.R. White from the University of California, Irvine, and supported by the DAAD *Doktorandenstipendium*.

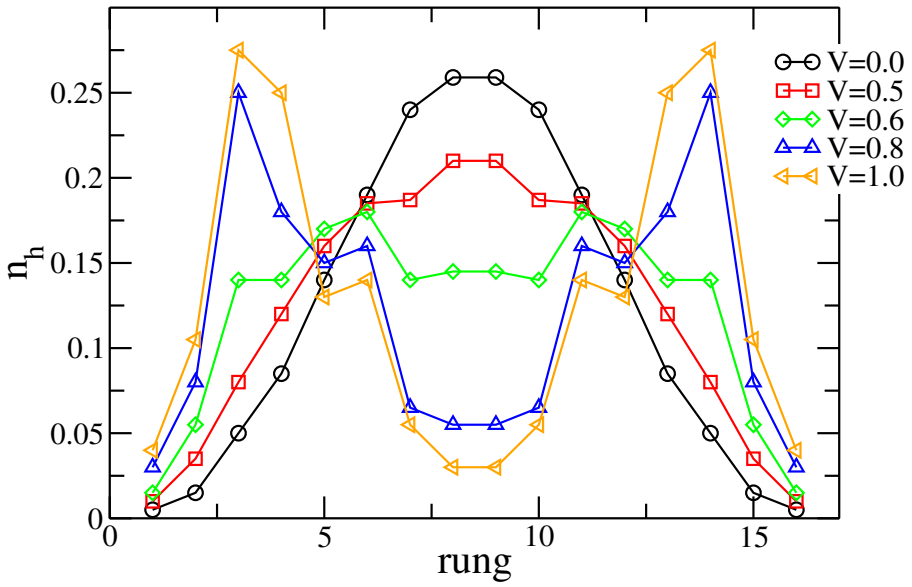

Figure 4.3: Hole density per rung for a 16×2 t-J ladder with 2 holes, $J/t = 0.35$, and different long range Coulomb repulsion V. The hole density evolves from a particle-in-a-box state to stripe formation by turning on the Coulomb repulsion.

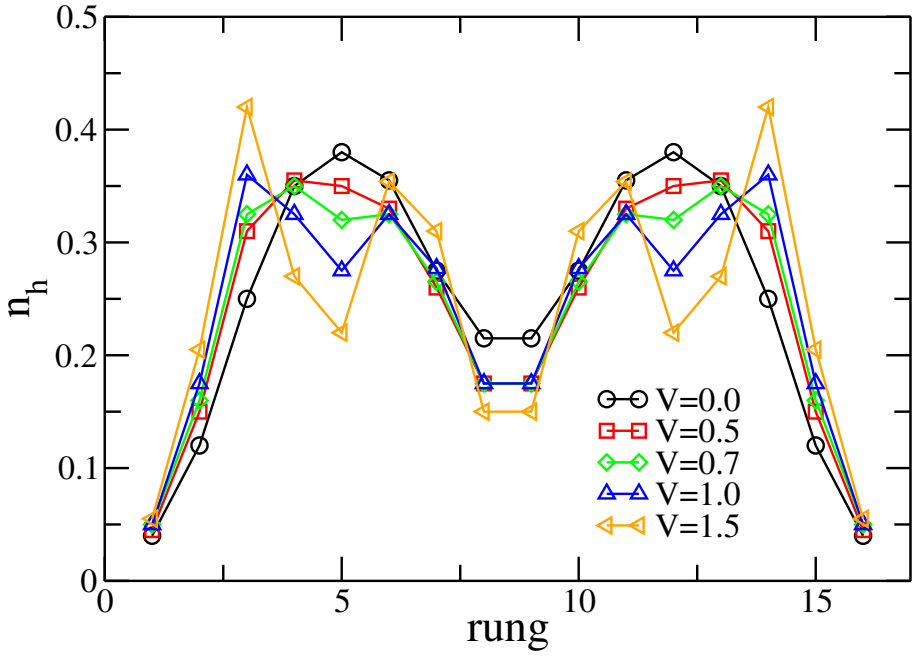

Figure 4.4: Hole density per rung for a 16×2 t-J ladder with 4 holes, $J/t = 0.35$, and different long range Coulomb repulsion V. The four holes build two pairs, which break up by turning on the Coulomb interaction. One can see four stripes for large repulsion.

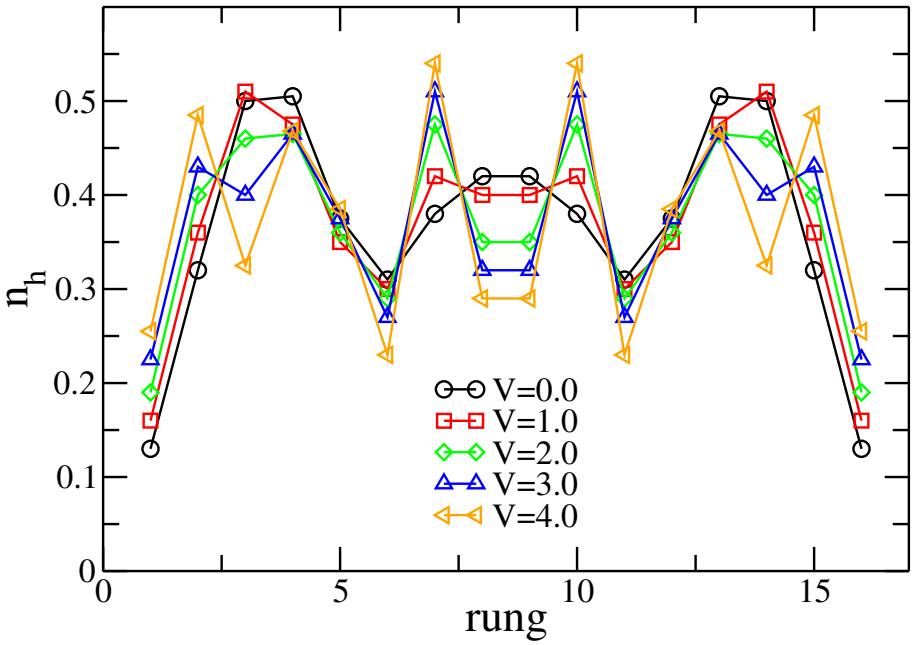

Figure 4.5: Hole density per rung for a 16×2 t-J ladder with 6 holes, $J/t = 0.35$, and different long range Coulomb repulsion V. Six holes build three pairs, which break up into six stripes by turning on V. The energy it takes to break up hole-pairs grows with the number of pairs.

Chapter 5

The (Cellular) Dynamical Mean-Field Theory ((C)DMFT)

Besides the DMRG, one of many other important methods used in condensed-matter physics is the dynamical mean-field theory. Both methods have more in common than just the two first letters (although they stand for different things, *density-matrix* on the one side, and *dynamical mean* on the other side). We have seen that the idea of the DMRG is to split the system in two blocks, a left block and a right block. All one needs to calculate properties of the left block is the density matrix of the right block. One could also say that the right block is some kind of *bath* for the left block. In DMFT, the physical system is transformed into a single site, or a cluster of special sites connected to a bath represented by a set of non-interacting sites. One can now easily see the similarities (and also the differences) in both methods. In both methods, the system is split up in two parts, where one part interacts with the rest of the system with either a density matrix or a dynamical Weiss field. Trying to combine the power of both methods, we first need to learn DMFT. One of the main numerical problems in the DMFT is the calculation of the Green's function for a finite system. All we need to do this is already implemented in the DMRG program. Hence, all we had to implement is the rest of the self-consistency loop. Since this thesis is not focused on the DMFT, we will not describe the method in full extent, but concentrate on the technical problems that can occur.

This chapter is organized as follows: First, we will give a short introduction of the DMFT. We will explain the basic idea and clarify all names that are used to describe all different kinds of Green's functions. For further

use, we will describe all steps of the self-consistency loop in detail. We will present results and show that they match with previous publications. We will then describe the Cluster or Cellular DMFT, also with the algorithm and some results.

5.1 DMFT

5.1.1 Introduction and nomenclature

The basic idea of dynamical mean-field theory [44] is as follows: to calculate physical properties of a single site in a lattice (e. g. the local Green's function), one treats this lattice site as an isolated site and the rest of the system as a non-interacting bath. This usually is justified by the vanishing of the corresponding class of diagrams in the limit of high spatial dimensions. This can be connected to the Hamiltonian of the SIAM, having also one site with interaction, the impurity coupling to the electrons of the conduction band. Thus, one has a single site, the impurity with chemical potential ε_d and Coulomb repulsion U connected to L bath sites with hopping amplitude V_l. Each bath site has also a respective chemical potential ε_l, but no Coulomb repulsion. This Hamiltonian can be diagonalized (numerically exactly) and we can calculate the on-site Green's function of the impurity. The Hamiltonian is given by:

$$\begin{aligned} H &= \sum_{l,\sigma} V_l \left(d_\sigma^\dagger c_{l,\sigma} + c_{l,\sigma}^\dagger d_\sigma \right) \\ &+ \varepsilon_d \sum_\sigma n_{d,\sigma} + U n_{d,\uparrow} n_{d,\downarrow} \\ &+ \sum_{l,\sigma} \varepsilon_i n_{l,\sigma}. \end{aligned} \tag{5.1}$$

Before we continue, we need to look at all the different names that appear in various DMFT papers. The nomenclature can be very confusing in DMFT. There is G, G_0, G^0, G^{free}, G_{lattice}, G_{bath}, $\mathcal{G}$ to name but a few. Some G's mean essentially the same, so we start explaining the G's we use in this chapter:

- $\mathcal{G}_0$ is called the Weiss field. Its physical content is that of an effective amplitude for a fermion to be created on the isolated site, propagating through the bath, and coming back to the isolated site to be destroyed. $\mathcal{G}_0$ represents the bath and is therefore also called bath Green's function.

$\mathcal{G}_0$ is sometimes called G_0 and can be written as

$$G_0^{-1}(i\omega_n) = i\omega_n - \varepsilon_d - \mu - \sum_l \frac{V_l^2}{i\omega_n - \varepsilon_l}. \tag{5.2}$$

- G is the full on-site Green's function of the system, i. e. the isolated site (impurity) and the bath sites. We calculate G by means of the Lanczos method. G is also called impurity Green's function G_{imp}, G_{SIAM} (single impurity Anderson model), or G^{And}.
- $\Sigma(i\omega_n) = \mathcal{G}_0^{-1}(i\omega_n) - G^{-1}(i\omega_n)$ is the self-energy of the impurity. It is used as a momentum independent approximation to the lattice model, thus $\Sigma_k(i\omega_n) = \Sigma(i\omega_n) + \ldots$.

One can derive a self-consistent loop of equations. The two main equations are the well known Dyson equation and the self-consistency equation

$$\mathcal{G}_0^{-1}(i\omega_n) = i\omega_n + \mu + G^{-1}(i\omega_n) - R[G(i\omega_n)], \tag{5.3}$$

where R is the reciprocal function of the Hilbert transform. Hence, it is possible to calculate the new Weiss field from the on-site Green's function. This leads to a self-consistency loop explained in the following section.

5.1.2 Algorithm

In this section we present the self-consistency loop and explain each step. We start with a random set of parameters for the bath sites, V_l and ε_l. The more sites the better the fit quality, but one gets reasonable results with just $L = 4$ to $L = 6$ sites. Next, one has to set up the Hamiltonian of the SIAM, where we have one impurity that is connected with the hopping amplitude V_l to bath site l. We need to calculate the on-site Green's function $G(i\omega_n)$ on the impurity. In our case, this is done by means of the Lanczos method. The next step is the calculation of the local self energy

$$\Sigma(i\omega_n) = \mathcal{G}_0^{-1}(i\omega_n) - G^{-1}(i\omega_n), \tag{5.4}$$

where

$$\mathcal{G}_0^{-1}(i\omega_n) = i\omega_n - \varepsilon_d - \mu - \sum_l \frac{V_l^2}{i\omega_n - \varepsilon_l}. \tag{5.5}$$

Now, we have to use the self-consistency equation to determine the *new* Green's function. This is given by the Hilbert transform

$$G^{\mathrm{new}}(i\omega_n) = \tilde{D}\left(i\omega_n + \mu - \Sigma(i\omega_n)\right). \tag{5.6}$$

The last step of the loop is the calculation of the new parameters of the bath, V_l and ε_d. This is done by fitting the new Weiss field

$$\mathcal{G}_0^{\text{new}}(i\omega_n) = \left(i\omega_n - \varepsilon_d - \mu - \sum_l \frac{(V_l^{\text{new}})^2}{i\omega_n - \varepsilon_l^{\text{new}}} \right)^{-1} \tag{5.7}$$

to $G^{\text{new}}(i\omega_n)$. The new loop starts now with the calculation of G for a system with the new values for V_l and ε_d. To sum up:

1. set up initial values for V_l and ε_l (random)
2. calculate the on-site Green's function G
3. calculate the self-energy Σ
4. apply the self-consistency equation to get G^{new}
5. get the new parameters V_l and ε_l by fitting the new Weiss field to G^{new}
6. unitl V_l and ε_l are converged, go back to (2)

5.1.3 Results

We compared our results for the Green's function on the imaginary-frequency axis as well as the spectral densities with the results obtained by Werner Krauth's LISA program [44, 45]. Since they examined the Hubbard model on the Bethe lattice, the self-consistency equation simplifies to

$$G_0^{-1}(i\omega) = i\omega + \mu - G(i\omega)/2. \tag{5.8}$$

We have plotted the spectral density "on the impurity" for $U = 0, 1, 3, 5$ for 5 bath sites in Figg. 5.1-5.4. Since we only wanted to check the results, we will not interpret them. Nevertheless, one can see nicely the Mott-Hubbard transition when we change the value of the Coulomb repulsion U. We have also plotted the Green's function G on the imaginary axis for the same systems in Fig. 5.6. We have only plotted the imaginary part of the G, because the real part vanishes if $\varepsilon_d = -U/2$ and $\mu = 0$. Last, we show the convergence of the ten parameters of the system, $\varepsilon_1, \ldots, \varepsilon_5$ and $V_1, \ldots, V_5$ in Fig. 5.5. It is easy to see that the parameters converge after about 10 iterations. In addition to that, they are symmetric.

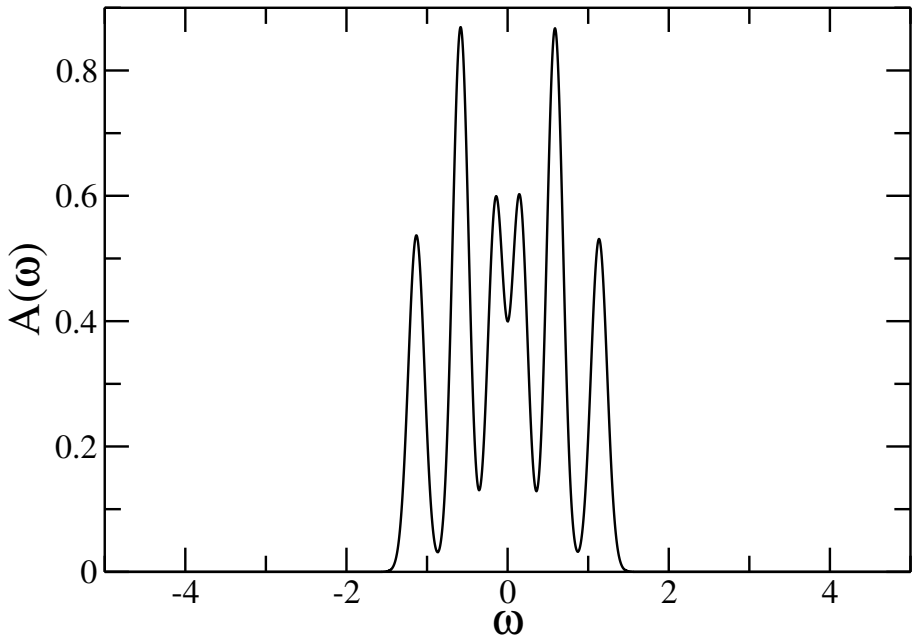

Figure 5.1: $A(\omega)$ with $U = 0$. We used 5 bath sites and did 40 loops. We use Gaussian broadening with $\sigma = 0.1$. Most of the weight is centered at the Fermi edge $\omega = 0$.

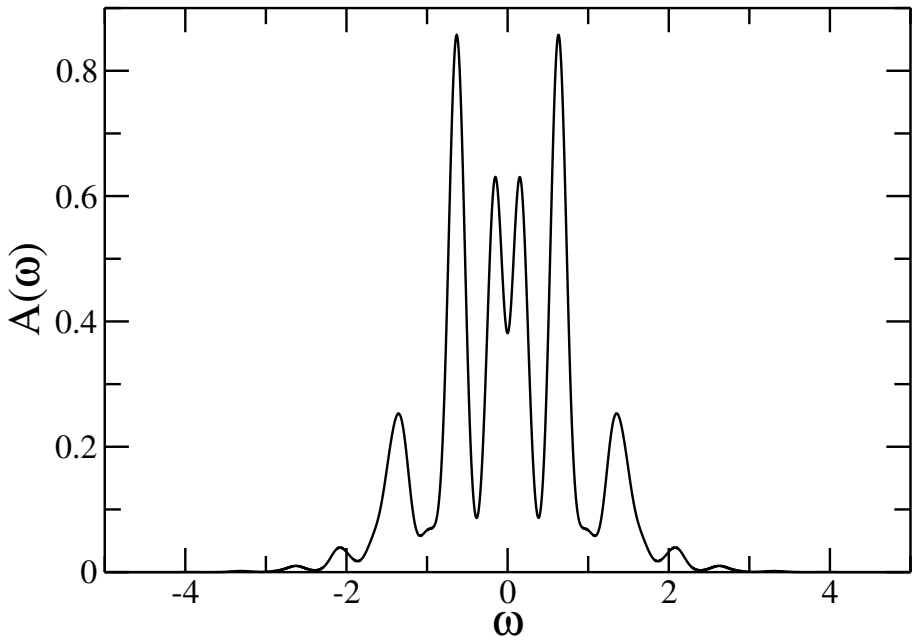

Figure 5.2: $A(\omega)$ with $U = 1$. We used 5 bath sites and did 40 loops. We use Gaussian broadening with $\sigma = 0.1$. The weight moves slowly to the middle of the band.

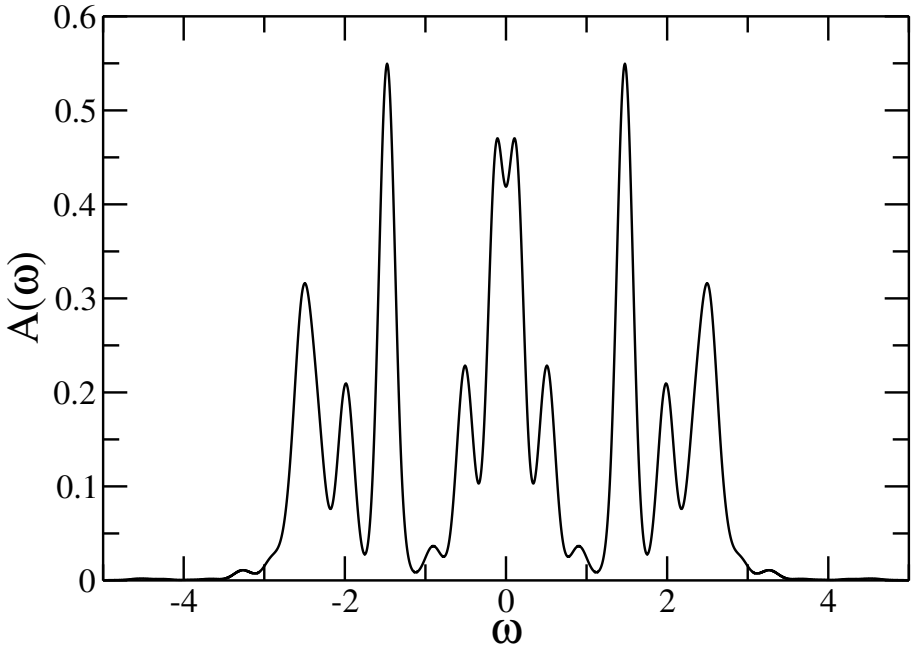

Figure 5.3: $A(\omega)$ with $U = 3$. We used 5 bath sites and did 40 loops. We use Gaussian broadening with $\sigma = 0.1$. One can see three main peaks: one in the middle and two at the band edge.

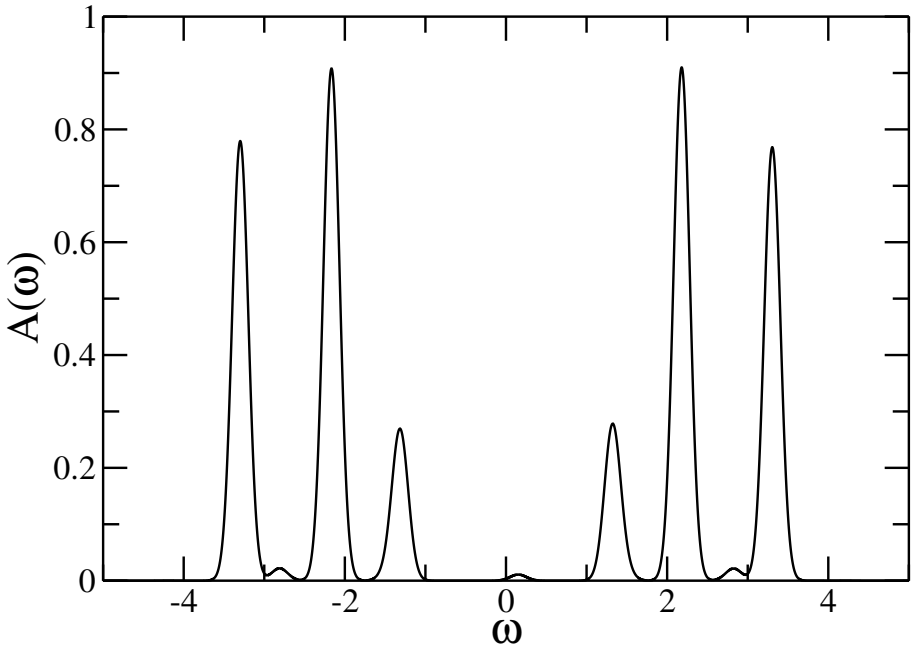

Figure 5.4: $A(\omega)$ with $U = 5$. We used 5 bath sites and did 40 loops. We use Gaussian broadening with $\sigma = 0.1$. There is almost no more weight in the middle of the band.

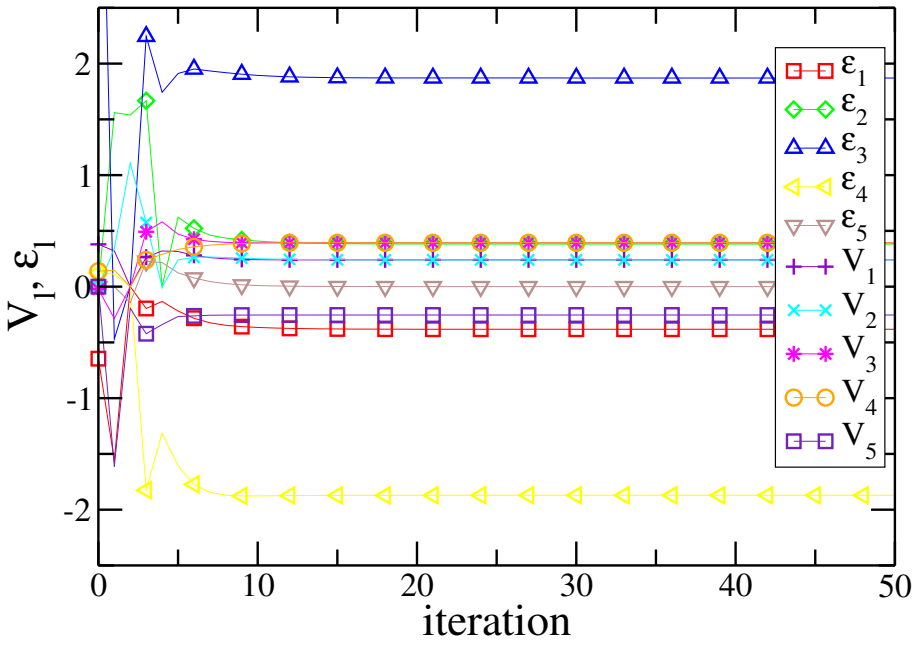

Figure 5.5: convergence of ε_l and V_l for $U = 3$.

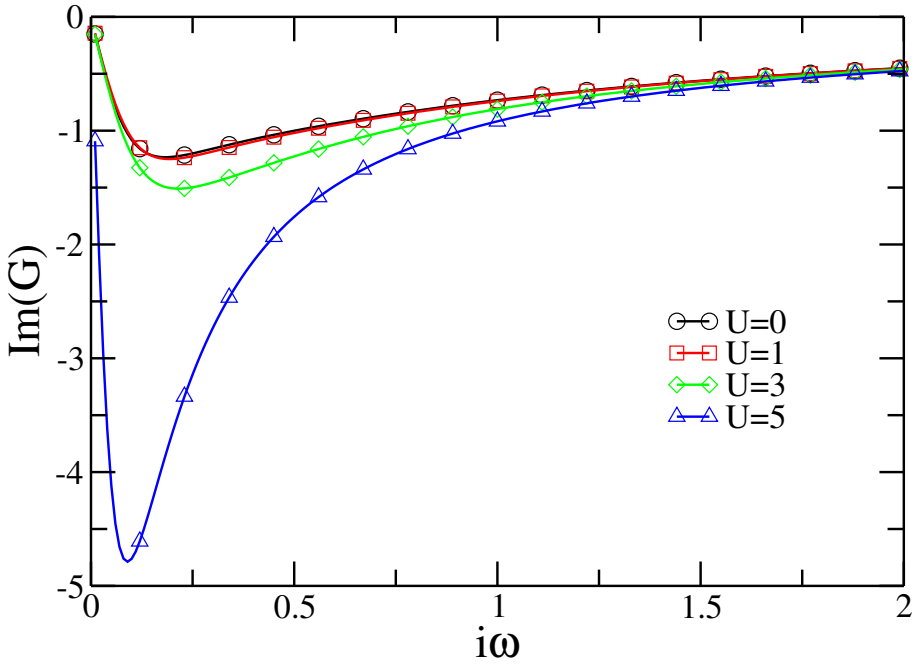

Figure 5.6: Im$G(i\omega)$ on the imaginary axis for different U. We have only plotted the imaginary part, because the real part vanishes for our set of parameters.

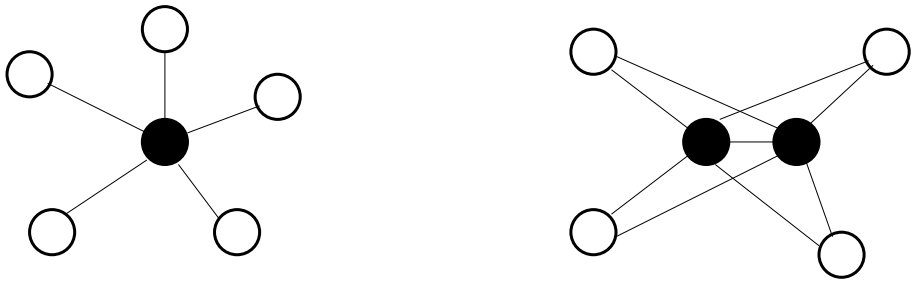

Figure 5.7: The *star* representation for the DMFT on the left hand side. The filled circle represents the Anderson impurity connected via coupling V_l to the bath sites, represented by empty circles. On the right hand side, we see the representation for the cluster or cellular DMFT, the CDMFT. We have two impurities connected by a hopping amplitude t representing the cluster. The bath sites are again represented by empty circles. It is important that each bath site is connected to both impurity sites. Thus, a particle can hop from impurity 1 to the bath and then to impurity 2.

5.2 CDMFT

5.2.1 Introduction

The normal or single-site DMFT is limited to the calculation of local Green's functions. One misses short range correlation, such as the k-dependence of the self-energy. It is therefore useful to extend the method, which is done in the Cellular DMFT, or Cluster DMFT [46, 47, 48]. The single site is replaced by a cluster of connected sites. We start with the simplest cluster possible containing more than one site: a two-site cluster. In this case, all bath sites now couple to both cluster sites. This is depicted in Fig. 5.7. The Hamiltonian changes in a canonical way and can now be written as:

$$\begin{aligned} H &= \sum_{l\mu,\sigma} V_{l\mu}\left(d^\dagger_{\mu,\sigma}c_{l,\sigma} + c^\dagger_{l,\sigma}d_{\mu\sigma}\right) \\ &+ \varepsilon_d \sum_{\mu,\sigma} n_{\mu,\sigma} + \sum_{\mu} U n_{\mu,\uparrow}n_{\mu,\downarrow} \\ &- t\sum_{\mu\neq\nu}\left(d^\dagger_{\mu,\sigma}d_{\nu,\sigma} + d^\dagger_{\nu,\sigma}d_{\mu\sigma}\right) \\ &+ \sum_{l,\sigma}\varepsilon_i n_{l,\sigma}. \end{aligned} \tag{5.9}$$

We use the standard notation, where l denotes a bath site, μ and ν denote cluster sites. The idea is about the same as in the single-site DMFT. We

have a similar set of equations forming a self-consistent loop. One of the main differences is that since the cluster has 2 sites, there is more than one Green's function. In fact, one has 4 Green's functions for each spin component:

- $G_{11}(z) = \langle\Psi_0| \left(c_1 \frac{1}{z-H} c_1^\dagger + c_1^\dagger \frac{1}{z+H} c_1\right) |\Psi_0\rangle$
- $G_{22}(z) = \langle\Psi_0| \left(c_2 \frac{1}{z-H} c_2^\dagger + c_2^\dagger \frac{1}{z+H} c_2\right) |\Psi_0\rangle$
- $G_{12}(z) = \langle\Psi_0| \left(c_1 \frac{1}{z-H} c_2^\dagger + c_2^\dagger \frac{1}{z+H} c_1\right) |\Psi_0\rangle$
- $G_{21}(z) = \langle\Psi_0| \left(c_2 \frac{1}{z-H} c_1^\dagger + c_1^\dagger \frac{1}{z+H} c_2\right) |\Psi_0\rangle$

The calculation of G_{11} and G_{22} (the diagonal elements) can be done by means of a standard routine, e. g. the Lanczos method. Since the calculation of the off-diagonal elements is more difficult, we present our solution of this problem: The Lanczos method cannot be applied directly, because c_1 is not the hermitean conjugate of $c_2^\dagger$. One possible way is to calculate the Green's function by the GMRES method leading to computational effort, because one has to calculate the Green's function for each frequency individually. Thus, we try to improve the Lanczos method. We want to calculate

$$\begin{aligned} G_{12}(z) &= \langle\Psi_0| c_1 \frac{1}{z-H} c_2^\dagger |\Psi_0\rangle \\ &= \sum_n \langle\Psi_0|c_1|\phi_n\rangle \frac{1}{z-E_n} \langle\phi_n|c_2^\dagger|\Psi_0\rangle, \end{aligned} \tag{5.10}$$

where ϕ_n is obtained using the Lanczos method. One source of error is the identity ϕ_n: The problem is that the Lanczos procedure breaks down when the ground state is reached and the eigenstates become non-orthogonal. If we stop the calculation of the basis when the ground state is reached, the basis is too small. One way is to apply re-orthogonalization. Another way is to check if each ϕ_n is really an eigenstate of the system. Thus, we check if

$$|H\phi_n - E_n\phi_n| < \varepsilon_E, \tag{5.11}$$

where $\varepsilon_E \sim 10^{-5}$ has proven to be useful. Another problem is the occurrence of so called *ghost* states in the Lanczos procedure. It is possible that higher lying states occur more than once in the Krylov basis. This problem has to be solved, because otherwise the spectral density gives unreasonable results

— some weights would be counted multiple times. To catch a ghost state, we compared the eigenenergies and the weights of two consecutive states. If

$$(|E_n - E_{n+1}| < \varepsilon_w \cdot E_n) \text{ and } (|w_n - w_{n+1}| < \varepsilon_w \cdot w_n)\,, \tag{5.12}$$

where $w_n = \langle \Psi_0 | c_1 | \phi_n \rangle \cdot \langle \phi_n | c_2^\dagger | \Psi_0 \rangle$ and $\varepsilon_w \sim 10^{-2}$, the state is discarded. We compared with results obtained from the GMRES method to check this method and to tune ε_w and ε_E.

5.2.2 Algorithm

To learn more about the CDMFT, we followed [47]. We will now briefly describe the self-consistent equations, which are similar to the single-site DMFT.

1. set up initial values for V_l and ε_l (random)
2. calculate the on-site Green's function $G_{\mu\nu}$
3. calculate the self energy $\Sigma_{\mu\nu}$
4. calculate $G^{\text{local}}_{\mu\nu}$
5. calculate the new Weiss field, $\mathcal{G}^{\text{new}}_{\mu\nu}$
6. get the new parameters V_l and ε_l by fitting the new Weiss field to G^{new}
7. if V_l and ε_l are not converged, go back to (2)

We have already noted that for a two-site cluster, the Green's functions and the self energy become (2×2) matrices. The self energy can be calculated from the Dyson equation

$$\Sigma = \mathcal{G}^{-1} - G^{-1} \tag{5.13}$$

which changes to

$$\Sigma_{\mu\nu} = \left(\mathcal{G}^{-1}\right)_{\mu\nu} - \left(G^{-1}\right)_{\mu\nu}. \tag{5.14}$$

The Weiss field is now given by

$$\mathcal{G}_{\mu\nu}(i\omega_n) = \left(i\omega_n \delta_{\mu\nu} - \varepsilon_d - \mu - \sum_l \frac{(V_{l\mu} V_{l\nu})}{i\omega_n - \varepsilon_l^{\text{new}}} \right)^{-1}. \tag{5.15}$$

The local Green's function is given by

$$G^{\text{local}} = \int_{-\pi/L_c}^{\pi/L_c} \frac{1}{i\omega_n + \mu - \Sigma_c(i\omega_n) - t(k)} \frac{dk}{2\pi/L_c} \tag{5.16}$$

with

$$t^{\mu\nu}(k) = -t[\delta_{\mu-\nu\pm1} + \exp(-ikN_c)\delta_{N_c+\mu-\nu\pm1} + \exp(ikN_c)\delta_{-N_c+\mu-\nu\pm1}], \quad (5.17)$$

where N_c is the number of cluster sites.

5.2.3 Results

We calculated the Green's function for different U and reproduced $\mathrm{Im}(G_{00}(i\omega_n))$ and $\mathrm{Re}(G_{01}(i\omega_n))$ from [46]. Our actual goal was to combine ideas of the DMRG and the DMFT. We will offer some ideas in the conclusion and outlook section of this thesis.

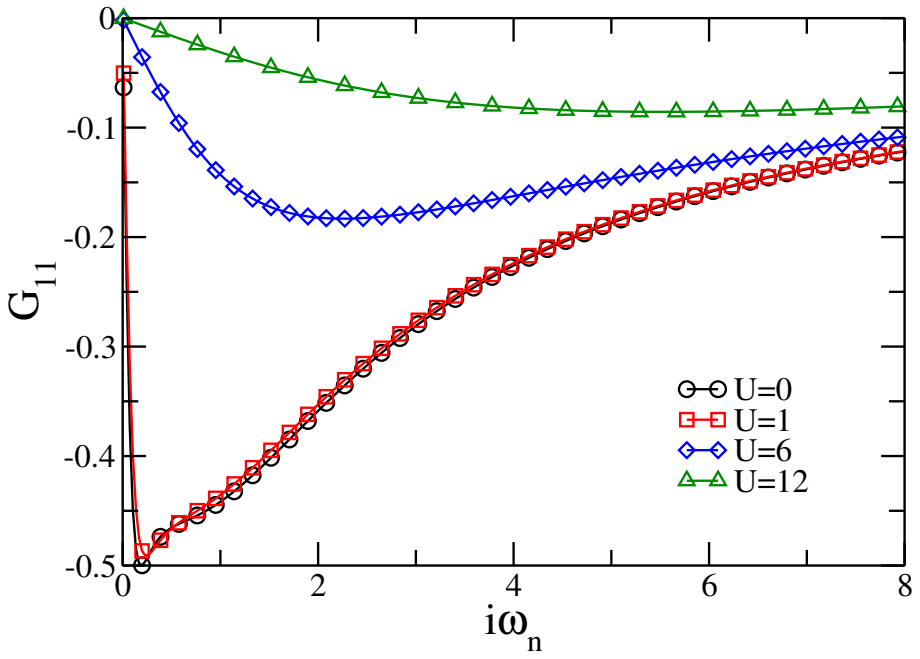

Figure 5.8: Im G_{11} on the imaginary axis for different U (Re $G_{11} = 0$). We used $L_{\text{bath}} = 4$ and $L_{\text{cluster}} = 2$.

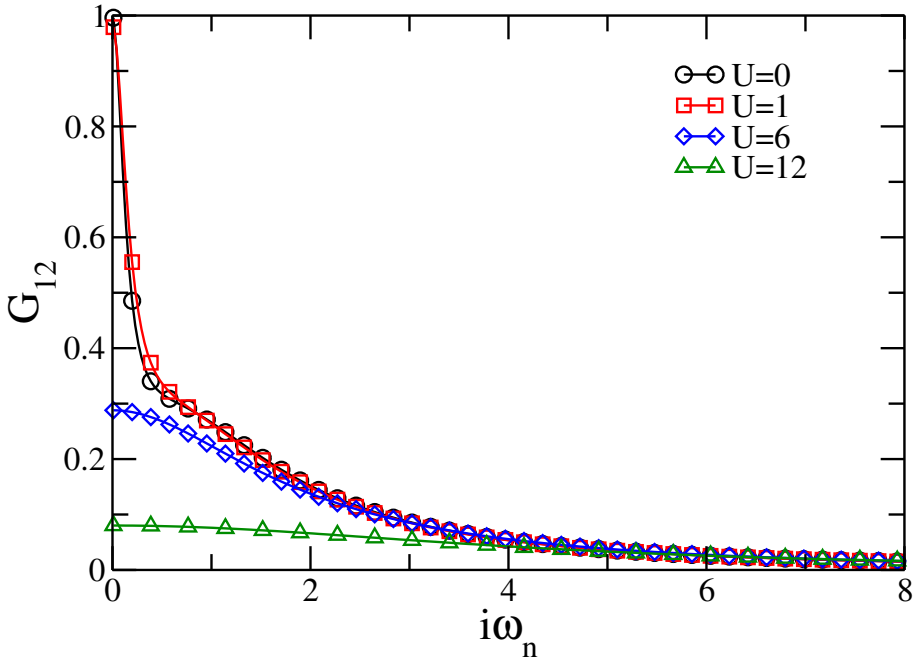

Figure 5.9: Re G_{12} on the imaginary axis for different U (Im $G_{12} = 0$). We used $L_{\text{bath}} = 4$ and $L_{\text{cluster}} = 2$.

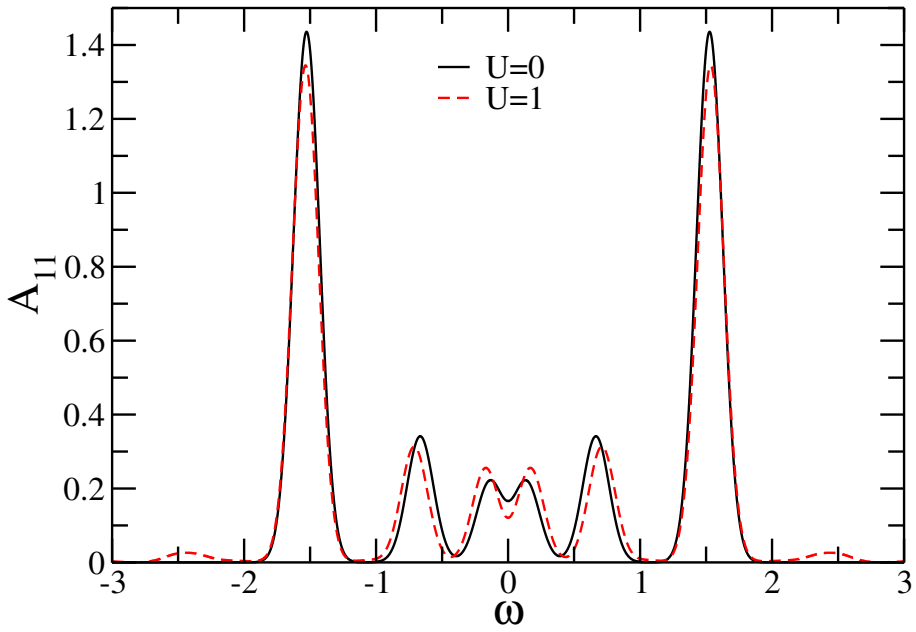

Figure 5.10: A_{11} for $U = 0$ and $U = 1$. We used $L_{\text{bath}} = 4$ and $L_{\text{cluster}} = 2$.

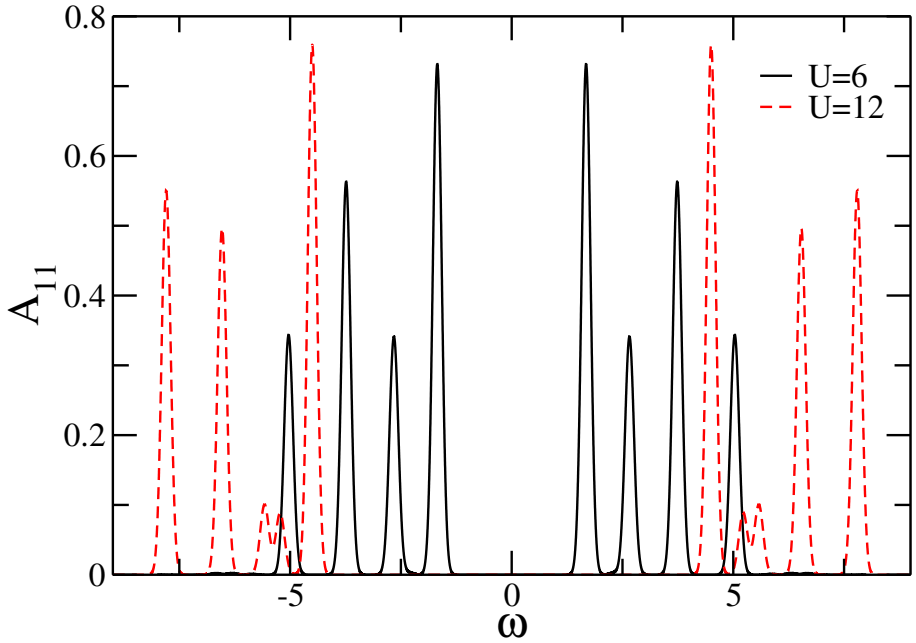

Figure 5.11: A_{11} for $U = 6$ and $U = 12$. We used $L_{\text{bath}} = 4$ and $L_{\text{cluster}} = 2$.

Chapter 6

Conclusion

The thesis is about various numerical methods and their application for physical systems. We started with the introduction of various theoretical models for quantum impurity problems and motivated this work with some experimental realizations. After explaining the concept of Greens functions and spectral densities, we start with the introduction of various numerical methods. The method of exact diagonalization is the most simple numerical method. No approximations are made, but the price is that one is limited to small system sizes. Since the Hilbert space of an interacting system grows exponentially with the number of system sites, one is restricted to about 10 lattice sites. Another way are iterative or *Krylov* methods: The idea of the *Lanczos* method is to transform the original Hamiltonian H into the Krylov basis $(v, Hv, H^2v, H^3v, \ldots, H^nv)$, where it is tridiagonal. The advantage is that the Hamiltonian is not needed explicitely — knowing how to build the product of Hamiltonian and wavefunction is sufficient. In addition, the ground state is approached very fast, such that about 100 Lanczos steps are sufficient for even much bigger matrices. It is also possible to calculate dynamical properties with the *Lanczos* method. This is used in other methods like DMRG and DMFT. The Bethe Ansatz is an exact method for the calculation of eigenvalues and eigenvectors of a limited class of quantum many-body systems. Although the eigenvalues and eigenvectors for a finite system may be obtained from numerical diagonalization, the Bethe Ansatz is not limited in the system size. In addition, it has two other advantages: All eigenstates are characterized by a set of quantum numbers which can be used to distinguish them according to specific physical properties, and the eigenvalues can be calculated in the thermodynamic limit. We used some results from the Bethe Ansatz for a 1D Hubbard model with open boundary conditions as reference values and sketched the Bethe Ansatz equation. Another approach are renormalization group calculations. The first one is the

numerical RG which was used to calculate the Kondo model. The idea of the NRG is to iteratively integrate out higher energy states in order to get the spectrum for the Hamiltonian H_N for each step N, which corresponds to a different energy scale.
One main part is the description of the density-matrix renormalization-group (DMRG). We recapitulate the properties of density matrices and show why the m eigenstates of the reduced density matrix with the highest eigenvalues are the optimal truncated basis. The idea of the *infinite system algorithm* is to start with a small system which is coupled to a bath. The system is increased in each step, while the basis size is kept constant by truncating it. The reduced density matrix is used to obtained the transformation matrix. The *finite system algorithm* is a further improvement: Several *sweeps* are performed where each block gets new information by adding non-truncated sites, while the total size of the superblock is kept constant.
There are two methods to measure dynamical properties with the DMRG: The *Lanczos vector method* and the *correction vector method*. The main difference in these methods is the choice of the target states (the states, that are used to calculate the density matrix). The Lanczos method is fast, but is limited to a small region around the Fermi energy. The correction vector method is difficult to use and slow, but gives accurate results all over the spectrum. Since the Lanczos method is very accurate in a region around the Fermi edge — we compared with results from the correction vector method — it fits our needs to calculate the Kondo resonance.
The main part of the thesis deals with the spectral density on the impurity and spin-spin correlations for a Single Impurity Anderson Model. First, we found that the spectral density is strongly dependent on the position of the impurity x_0. The higher the local density of states at site x_0, the more states can interact with the impurity and the higher the Kondo peak. Although we can not apply the standard formulas from Kondo physics to our problem due to differences in the Hamiltonian (local coupling of the impurity) and other assumptions (non-flat conduction band), we found good agreement between the estimated Kondo temperature and the height (or weight) of the Kondo peak. Next, we looked if the shape of the Kondo peak changes if the system size is increased. For an even number of particles in the system we found that the shape of the Kondo peak does not depend on the size of the system as long as the local density of states at site x_0 is sufficiently large. If this is not given, the Kondo peak collapses for large systems. We could observe strong differences in the spectra when the number of particles N in the system is even or odd. If N is odd, the double occupancy of the top most single particles level enforces one electron to move to the next higher lying energy state, thus reducing the energy gain from spin flip transition. Hence,

the height of the Kondo peak is smaller when N is odd. One could see that the height of the Kondo peak oscillates when the number of particles changes between even and odd. This could be used as a signature for experiments. Unlike the spectra for even N, the height of the Kondo peak increases when the system size is increased for odd N. The energy that one has to pay to lift one electron to the next higher lying level decreases with the increasing system size and finally converges. Hence, the height of the Kondo peak also converges for large systems.
By measuring the spin-spin correlation function of the impurity spin and the spin on the conduction band we could get an insight in the Kondo screening cloud. We found differences in the behavior of the correlations when N is even or odd, too. When N is even, we could observe the following: The higher the Kondo temperature, the more of the impurity spin is compensated in a smaller region near the impurity. We found regions where the correlation function $C(r) \sim 1/r$ and where $C(r) \sim \exp(-r)$. When the Kondo temperature is high, the correlations do not change for a large region around the impurity. The higher T_K, the better the match of correlation functions of different system sizes. We defined the numerical correlation length l_k^{num} by the site where 75% of the impurity spin is compensated. Although this means that l_k^{num} is always within the system, we could find resemblance to the theory. By increasing the system size, l_k^{num} increases and finally converges. The higher the Kondo temperature, the sooner l_k^{num} converges. If l_k^{num} does not change anymore by increasing the system size, the impurity spin is fully compensated within the system, and the Kondo cloud is fully developed, hence $\xi < L$.
If N is odd, we found that the correlation function decreases for smaller system. Since spin-flip transitions are reduced for smaller systems, n_d, the electron number on the impurity, is reduced, and a smaller impurity spin has to be compensated. For an even N, n_d is nearly constant for different L. In addition, we found that the correlation functions for an odd N and for different L do not match anymore, although they become more similar when we reach system sizes of ~ 500 lattice sites. We found a connection of the height of the Kondo peak and the numerical l_k for an odd N and different system sizes. Both values increase logarithmically for intermediate system sizes ($L < 200$) and then finally start to converge. We could not measure systems that large that l_k is finally fully converged.

We also looked at a Hubbard ring and a $t - J$ ladder with long range Coulomb interaction. The technical problem of including long range interactions in DMRG is that the number of operations increases with the square of the system size, L^2. The common strategy is to reduce the growth of

operations from L^2 to L by building a set of help operators. Much of the interesting physics of high-T_C superconductors is local on a length scale of the superconducting coherence length ξ_0, which is typically a few lattice constants. Studies of t-J systems have provided strong evidence of a robust d-wave character of local pairing correlations, and of a strong clustering tendency of holes which might lead to stripes or phase separation. However, most studies for the t-J model have failed to find evidence of the strong superconducting correlations needed to understand high-T_C superconductivity. All these calculations omit the long-range part of the Coulomb interaction. Various t-J lattices have been measured, where the DMRG is used to calculate the short range interaction, and the long-range interaction is taken into account within a Hartree approximation. Our goal was to proof the results, while including the long-range interaction into the DMRG. But first, we examined the hole density for a 16×2 t-J ladder with 2 to 6 holes. We found that without Coulomb repulsion, the holes tend to build pairs. By turning on Coulomb interaction, one can break up these pairs, which leads to the generation of stripes. It takes significantly more energy and a thus a stronger repulsion to break up three pairs instead of just one pair.

Besides the DMRG, one of many other important methods used in condensed matter physics is the dynamical mean-field theory. We explained the basic idea of the DMFT and clarified all names that are used to describe all different kinds of Green's function. For further use, we described all steps of the self-consistency loop in detail. We presented results and showed that they match with previous publications.
The normal or single-site DMFT is limited in the calculation of local functions. One misses short range correlation, such as k-dependence of the self-energy. It is therefore useful to extend the DMFT. This is done in the Cellular DMFT, or Cluster DMFT. The single-site is replaced by a cluster of interacting sites. We showed how the equations of the self-consistent loop change for a 2-site cluster. Last, we showed results and compared with previous published papers.

Although we could answer some question, there is still a lot that should be done in the future:

The spin-spin correlation gave us some insight into the Kondo screening cloud. The correlation function is a function in real space, but it should be possible to measure the spin-spin correlation in frequency space (energy resolved). We could also add coulomb interaction into the tight-binding chain, or even long-range coulomb interaction. Another interesting setup is one im-

purity at each end of a tight binding chain.

For the long-range interaction in the t-J ladder, there are much more things one should measure, like the spin gap $E_{S=1} - E_{S=0}$. The pair binding energy $E_{N+2} + E_N - 2E_{N+1}$ would also give more insight how the pairs behave and break up. The pair-pair correlation could be used to probe superconductivity.

We thought about possibilities to improve DMFT and CDMFT. Therefore, we first looked at the Green's function for a cluster that is connected to a bath, e. g. we split up a one-dimensional Hubbard chain into two blocks — like in the DMRG. The first question is how the full Green's function in the cluster can be expanded in terms of the bare Green's function of the cluster and the bath, and the connection between both parts. This leads to a *Lippmann-Schwinger* like equation, allowing the calculation of the T-matrix.

Chapter 7

Deutsche Zusammenfassung

Diese Arbeit behandelt die Untersuchung verschiedener physikalischer Systeme mit unterschiedlichen numerischen Methoden. Wir beschreiben einige Ansätze für theoretische Modelle der Quanten-Störstellen Probleme, allen voran das Kondo Modell und das Anderson Modell. Zudem motivieren wir diese Arbeit durch einige Experimente: Insbesondere die Versuche von Lieber et al. [9] zeigen, dass die untersuchten Proben mittlerweile so klein sein können, dass Effekte auftreten können, die nur durch die endliche Systemgröße bedingt sind.
Das Kapitel über numerische Methoden leitet die Methode der *Exakten Diagonalisierung* ein. Es ist die wohl einfachste Methode, da keine Approximationen verwendet werden. Allerdings kann sie nur auf kleine Systeme angewendet werden, also Systeme mit einer nicht zu großen Basis. Einen Zugang zu größeren System liefern die sogenannten *Krylov* Methoden. Sie sind iterativ, so dass der Hamilton-Operator nicht explizit aufgebaut werden muss — eine Funktion zur Berechnung des Produktes aus Hamilton-Operator und Wellenfunktion ist ausreichend. Die *Lanczos* Methode transformiert einen Hamiltonian in eine Basis, in der die Matrix tridiagonal ist und dann leicht diagonalisiert werden kann. Allerdings ist die Lanczos Methode auf die Berechnung des Grundzustandes und der ersten angeregten Zustände beschränkt. Weiterhin ist die Lanczos Methode auch geeignet, um Greensche Funkionen zu berechnen.
Der Vergleich mit exakten Daten ist unerlässlich beim Testen einer numerischen Methode. Eine geeignete Methode zur Berechnung von eindimensionalen Systemen ist der Bethe Ansatz. Wir beschreiben die Gleichungen, die sich für eine Hubbard Kette mit offenen Randbedingungen ergeben. Da diese Methode nicht durch die Systemgröße beschränkt ist, ist sie optimal, um die Implementierung der DMRG zu überprüfen. Eine weitere Herangehensweise an quantenmechanische Vielteilchensysteme sind Renormierungsgruppenver-

fahren. Die numerische Renormierungsgruppe (NRG) wurde entwickelt, um das Kondo Problem zu berechnen. Die Idee ist, dass man iterativ Zustände höhere Energie *ausintegriert*. So erhält man in jedem Schritt N das Spektrum eines Hamiltonians H_N, der einer anderen Energieskala entspricht. Der Nachteil der NRG ist, dass sie nicht eins zu eins auf Systeme im Ortsraum angewendet werden kann.
Den Hauptteil nimmt die Beschreibung der Dichtematrix Renormierungsgruppe ein. Wir wiederholen die Eigenschaften der Dichtematrix und zeigen, wie und warum die reduzierte Dichtematrix benutzt wird, um die Basis eines Systems abzuschneiden, das an ein Bad gekoppelt ist. Die Idee des sogenannten Algorithmus der unendlichen Systemgröße ist, mit einem kleinen System zu beginnen, das an ein Bad gekoppelt ist. Das System wird vergrößert, indem iterativ Gitterplätze hinzugefügt werden. Die Basis wird dabei in jedem Schritt abgeschnitten, wobei die m Eigenvektoren der reduzierten Dichtematrix mit den größten Eigenwerten die neue Basis bestimmen. Beim Algorithmus der endlichen Systemgröße wird die Größe des Superblocks (System und Bad zusammen ergeben den Superblock) konstant gehalten, nachdem der Superblock durch die Methode der unendlichen Größe die gewünschte Länge erreicht hat. Wir zeigen weiterhin, wie Operatoren gehandhabt und Messungen durchgeführt werden, sowie wie die jeweilige Grundzustandswellenfunktion in die neue Basis transformiert werden kann, um die neue Berechnung des Grundzustandes deutlich zu beschleunigen. Die DMRG leifert präzise Ergebnisse für Grundzustandserwartungswerte und Korrelationsfunktionen von niedrigdimensionalen Systemen. Weiterhin gibt es auch zwei Methoden, um dynamische Eigenschaften auszurechnen: Die Lanczos-Vektor Methode und die Korrektur-Vektor Methode. Der Hauptunterschied beider Methoden liegt in der Wahl der Zielzustände, also der Zustände, die benutzt werden, um die Dichtematrix zu berechnen. Bei der Lanczos-Vektor Methode sind dies in der Regel der Grundzustand, ein durch ein zusätzliches Teilchen angeregter Zustand, und die ersten paar Lanczos Vektoren. Dadurch ist diese Methode einfach zu implementieren und schnell durchzuführen. Allerdings liefert sie nur gute Ergebnisse in der Nähe der Fermikante. Bei der Berechnung der Zielzustände der Korrekturvektormethode wird eine Inversion des Hamilton-Operators benötigt, was sich als sehr zeitintensiv herausstellt. Der Vorteil ist jedoch, dass diese Methode nicht auf ein bestimmtes Gebiet des Spektrums beschränkt ist, indem der Zielzustand individuell an die untersuchte Frequenz angepasst wird. Wir vergleichen beide Methoden und zeigen, warum die Lanczos-Vektor Methode für unsere Berechnung der Kondo Resonanz ausreichend ist.
Einen Hauptteil dieser Arbeit nehmen unsere Ergebnisse über die Spektraldichte und die Spin-Spin Korrelationen im Anderson Modell ein. Unser unter-

suchtes System weist einige Unterschiede zum klassischen Anderson Modell auf: In unserem Modell koppelt die Verunreinigung nur mit einem Gitterplatz, zudem haben wir kein flaches Leitungsband. Neben den Standardparametern Coulombabstoßung U, Hybridisierung V und lokalem Niveau ε_d, die so bestimmt werden, dass sich das System im Kondo Regime befindet, müssen wir auch den Ort der Störstelle wählen. Falls die Kette aus einer ungeraden Anzahl an Gitterplätzen besteht, so ist der Grundzustand doppelt entartet, wenn x_0 ungerade ist und die Anzahl der Teilchen gerade ist. Dies ist ein direkter Effekt aus der endlichen Systemgröße: Die Wellenfunktion des Elektrons an der Fermikante hat an allen ungeraden Gitterplätzen einen Knoten und kann so mit der Störstelle nicht wechselwirken. Allerdings ist die Entartung nicht der einzige Effekt, der beobachtet werden konnte: So fanden wir heraus, dass die Spektraldichte sehr stark von der Position x_0 der Verunreinigung abhängt. Je höher die lokale Zustandsdichte am Ort x_0, desto mehr Zustände können zur Kondo Resonanz beitragen, was dann einen größeren Peak ergibt. Obwohl wir die Formeln der Standard Kondo Physik nicht andwenden können, konnten wir durch einen Vergleich der ersten beiden Ordnungen Störungsrechnung eine Abschätzung der Kondotemperatur geben, die gut mit den gemessenen Resultaten übereinstimmt: An den Orten, an denen die lokale Zustandsdichte groß war, ist sowohl T_K als auch die Kondoresonanz groß.
Interessant sind die Unterschiede zwischen einem System mit gerader und mit ungerader Teilchenzahl. So konnten wir einige Vermutungen [36] nicht bestätigen, haben allerdings andere Ideen durchaus aufgreifen können. Bei einer geraden Anzahl von Teilchen im System ändert sich die Kondoresonanz nicht, wenn wir die Systemgröße ändern, solange die lokale Zustandsdichte hoch genug ist. Der Grund ist die gegenseitige Aufhebung zweier Effekte: Eine Systemvergrößerung bewirkt zugleich eine Verkleinerung der Niveauabstände im Leitungsband. Dadurch befinden sich mehr Zustände im Bereich des Kondopeaks und können diesen vergrößern. Allerdings verringert sich die lokale Dichte eines jeden Zustandes mit steigender Systemgröße.
Falls die Zustandsdichte zu gering ist, kollabiert der Kondo-Peak bei steigender Systemgröße, weil kaum noch Zustände dazu beitragen können.
Bei einer ungerade Anzahl an Elektronen im System ist der oberste Zustand im Leitungsband doppelt besetzt. Ein Spinflip auf der Verunreinigung ist deshalb nur möglich, wenn ein Elektron auf einen höheren Zustand angeregt wird. Dadurch veringert sich die Energie des Systems durch einen Spinflip nicht mehr um $\sim T_K$, sondern nur noch um $\sim T_K - \Delta E$, wobei ΔE der Niveauabstand ist. Wir konnten beobachten, dass der Kondopeak im ungeraden Fall immer kleiner ist als im geraden Fall. Weiterhin konnten wir sehen, dass die Resonanz mit steigender Systemgrösse ansteigt. Durch das Ansteigen der

Systemgrösse verringert sich ΔE, was Spinflip Prozesse deutlich attraktiver macht. Das Ansteigen des Kondo-Peaks mit der Systemgröße konvergiert im gleichen Maße wie ΔE.

Eines der interessantesten Teilgebiete der Kondo Physik ist die Suche nach der sogenannten Kondo Abschirm-Wolke [37]. Man erwartet, dass ein Elektron ein Singulett mit dem Spin der Verunreinigung bildet und diese so komplett abschirmt. Elektronen außerhalb der Wolke mit einer Größe von $\xi = v_F/T_K$ *sehen* die Verunreinigung dann nicht mehr. Wie groß ist nun die Kondo-Wolke in einem endlichen System? Um dies zu untersuchen, haben wir die Spin-Spin Korrelationsfunktion des Spins auf der Verunreinigung und denen der Leitungsbandelektronen gemessen. Da im eindimensionalen System die Abschirmlänge gleich der Korrelationslänge ist, war dies eine geeignete Methode. Wir konnten leicht sehen, dass die Korrelationen im Bereich um die Verunreinigung stark mit der Kondo-Temperatur ansteigen. Wie erwartet wird bei hohem T_K ein großer Teil des Spins auf der Verunreinigung lokal abgeschirmt. Bei der Untersuchung von Systemen mit 100 bis 500 Gitterplätzen konnten wir zeigen, dass die Korrelationsfunktionen im Nahbereich der Verunreinigung bei hoher Kondo-Temperatur nicht von der Systemgröße abhängen: Die Verunreinigung ist schon im kleinen System völlig abgeschirmt. Doch wie definiert man die Korrelationslänge in einem endlichen System? Die Standarddefinition ist, dass bei ξ der komplette Spin der Verunreinigung abgeschirmt ist. Bei einem endlichen System im kanonischen Ensemble ist der Gesamtspin konstant, so dass sich die Kompensation des Spins der Verunreinigung über das komplette System erstreckt. Wir haben deshalb eine numerische Korrelationslänge wie folgt definiert: l_k^{num} ist der Abstand zur Verunreinigung, an dem 75% des Spins kompensiert sind.
In einem System mit ungerader Teilchenzahl nehmen die Korrelationen bei kleineren Systemen ab: Durch eine niedrigere Besetzung der Verunreinigung muss auch ein kleinerer Gesamtspin kompensiert werden. Weiterhin fanden wir, dass die Korrelationsfunktionen für verschieden große Systeme nicht mehr übereinstimmen — auch bei hoher Kondotemperatur. Allerdings konnten wir einen interessanten Zusammenhang zwischen der numerischen Korrelationslänge und dem Gewicht der Kondo Resonanz feststellen: Beide Größen steigen erst logarithmisch mit der Systemgröße an, bis sie dann schließlich konvergieren. Es ist uns also gelungen, einen festen Zusammenhang zwischen der Kondoabschirmwolke und der Kondoresonanz zu finden.

Weiterhin untersuchten wir Systeme — einen Hubbard Ring und eine t-J Leiter — mit langreichweitiger Coulombwechselwirkung mit Hilfe der DMRG. Das technische Problem besteht nun darin, dass bei langreichweitiger Wech-

selwirkung die Anzahl der Operationen quadratisch mit der Systemgröße ansteigt. Das übliche Vorgehen besteht in der Bildung von Hilfsoperatoren, so dass die Anzahl der Operationen nur noch linear mit der Systemgröße wächst.
Ein Grossteil der interessanten Physik der Hochtemperatur Supraleiter findet lokal auf eine Längenskala ξ_0 statt, die typischerweise ein paar Gitterkonstanten beträgt. Untersuchungen an t-J Systemen lieferten zum einen Hinweise auf einen d-Wellen Charakter der lokalen Paar-Korrelationen, zum anderen konnte gezeigt werden, dass sich Löcher lokal anhäufen was zur Phasenseparation führen kann. Die meisten Untersuchungen konnten allerdings noch keinen Beweis für die starken Korrelationen finden, die nötig sind, um die Hochtemperatur Supraleitung zu verstehen. Alle bisherigen Untersuchungen haben allerdings die langreichweitige Wechselwirkung vernachlässigt. Viele t-J Systeme wurden bereits untersucht, wobei die DMRG benutzt wurde, um die kurzreichweitigen Kräfte zu berechnen, und die langreichweitigen Kräfte mit Hilfe einer Hartree Approximation berücksichtigt wurden. Unser Ziel war es, diese Resultate zu verifizieren, indem wir die Hartree Approximation durch die DMRG ersetzen. Zuerst schauten wir uns eine 16×2 t-J Leiter mit 2 - 6 Löchern an. Wir konnten sehen, dass die Löcher ohne langreichweitige Coulombabstoßung Paare bilden. Beim Einschalten der langreichweitigen Wechselwirkung werden diese Paare aufgebrochen und es bilden sich sogenannte *stripes* (Streifen), wobei die benötigte Energie deutlich mit der Anzahl der Lochpaare ansteigt.

Eine sehr erfolgreiche Methode im Bereich der theoretischen Festkörperphysik neben der DMRG ist die Dynamische Molekularfeld Theorie (Dynamical Mean-Field Theorie, DMFT). Wir erläutern die Idee, die hinter dieser Methode steckt und zeigen im Vergleich unsere Ergebnisse mit bereits veröffentlichtem Material, dass wir das Verfahren beherrschen. Als Hilfe für folgende Arbeiten schildern wir die Schritte der Selbstkonsistenzschleife in aller Ausführlichkeit.
Die DMFT ist beschränkt auf die Berechnung von lokalen Größen. Kurzreichweitige Korrelationen, oder die Impulsabhängigkeit der Selbstenergie können nicht berücksichtigt oder untersucht werden. Eine Erweiterung der DMFT ist die *Cellular DMFT*. Wir zeigen, wie man die Selbstkonsistenzschleife erweitern muss, und zeigen Lösungen der auftretenden Probleme, z.B. die Berechnung nicht-diagonaler Green'scher Funktionen.

Obwohl wir viele Antworten auf unsere Fragen gefunden haben, konnten wir vieles auch nicht beantworten, auch weil sich durch neue Erkenntnise immer wieder Probleme aufwerfen. Folgendes sollte in naher Zukunft noch unter-

sucht werden, weil wir uns vielversprechende Resultate erhoffen:
Durch die Spin-Spin Korrelation haben wir einen ersten Einblick in die Kondo Abschirmwolke erhalten. Bisher haben wir die Korrelationen aber *nur* im Ortsraum untersucht. Interessant wäre sicherlich auch eine energieaufgelöste Korrelationsfunktion, um zu sehen, wie die Abschirmung bei unterschiedlichen Frequenzen aussieht. Weiterhin kann man eine Coulomb-Abstoßung in das Leitungsband einfügen, oder sogar eine langreichweitige Coulomb-Abstoßung. Weiterhin gibt es erste Experimente, bei denen zwei Verunreinigungen, jeweils am Ende der Kette, untersucht werden. Hier stellt sich die Frage, wie und ob sich beide Verunreinigungen beeinflussen. Sowohl die Spektraldichte als auch die Kondo-Abschirmwolken sind sicherlich interessante Größen, wobei die energieaufgelöste Korrelationsfunktion einen noch tieferen Einblick ermöglicht. Durch die Erfahrung mit der CDMFT ist das Programm auch in der Lage, nicht-diagonale Green'sche Funktionen zu berechnen, so dass von der Methodik keine Steine in den Weg gelegt werden.

Bei der Berechnung der Eigenschaften der t-J Leiter sind noch einige Sachen offen geblieben: Die Energielücke des Spins, also $E_{S=1} - E_{S=0}$, und die Paar-Bindungsenergie $E_{N+2} + E_N - 2E_{N+1}$ geben sicherlich noch mehr Einsicht in das Bilden und Aufbrechen von Loch-Paaren. Weiterhin kann man durch die Paar-Paar Korrelation feststellen, ob Supraleitung vorliegt.

Es gibt sicherlich mannigfaltige Entwicklungsmöglichkeiten im Bereich der DMFT und der CDMFT. Gerade CDMFT und DMRG haben einige Gemeinsamkeiten, so dass man versuchen sollte, die Stärke aus beiden Methoden zu vereinen. Als erste Gemeinsamkeit wäre zu nennen, dass man in beiden Methoden ein *System* mit einem *Bad* wechselwirkt. Bei der CMDFT besteht das System aus einigen wechselwirkenden Gitterplätzen, das Bad besteht aus freien Gitterplätzen. Bei der DMRG besteht das System entweder aus dem linken oder rechten Block, und das Bad bildet der jeweils andere Block. Die erste Frage, die sich uns gestellt hat, war, wie die volle Green'sche Funktion auf dem System aus der reinen Green'schen Funktion des Systems und der Green'schen Funktion des Bads bestimmt werden kann. Ein erster Versuch führte auf eine *Lippmann-Schwinger* Gleichung, aus der sich mit Hilfe von GMRES die T-Matrix bestimmen lässt.

List of Figures

List of Abbreviations

1D	one dimensional
SIAM	Single Impurity Anderson Model
L	number of chain sites (excluding impurity)
N	number of particles
U	Coulomb repulsion
V	coupling between impurity and site x_0
ε_d	local chemical potential on the impurity
x_0	site of chain that is connected to the impurity
DOS	density of states
D	bandwidth
$A_d(\omega)$	specral density on the impurity (on-site)
$A_{d,\sigma}(\omega)$	specral density on the impurity (on-site), calculated with $c_\sigma^\dagger$, c_σ
W_K	weight of the Kondo peak
H_K	height of the Kondo peak
ΔE	level spacing for finite systems
$K(x)$	spin-spin correlation function as function of the position
$C(r)$	spin-spin correlation function; $C(r) = (K(x) + K(x+1))/2$
l_k	correlation length for the spin-spin correlation
l_k^{num}	numerical l_k
DMFT	Dynamical Mean-Field Theory
CDMFT	Cellular Dynamical Mean-Field Theory
DMRG	Density-Matrix Renormalization-Group
GMRES	Generalized Minimal Residual Method

Bibliography

[1] P. Fulde. *Electron Correlation in Molecules and Solids*. Springer-Verlag, 1991.

[2] A. C. Hewson. *The Kondo Problem to Heavy Fermions*. Cambridge University Press, 1993.

[3] L. Kouwenhoven and L. Glazman. Revival of the Kondo effect. *Physics World*, 2001.

[4] J. Kondo. *Prog. Theor. Phys.*, 32:37, 1964.

[5] P. W. Anderson. *Phys. Rev.*, 124(41), 1961.

[6] P. W. Anderson and G. Yuval. *Phys. Rev. Lett.*, 23(89), 1969.

[7] L. Glazman and M. Raikh. Resonant Kondo transparency of a barrier with quasilocal impurity states. *JETP Lett.*, 47:452–455, 1988.

[8] D. Goldhaber et al. Kondo effect in a single electron transistor. *Nature*, 391:156–159, 1998.

[9] T.W. Odom, J. Huang, C.L. Cheung, and C.M. Lieber. Magnetic Clusters on a Single-Walled Carbon Naotubes: The Kondo Effect in a One-Dimensional Host. *Science*, 290:1549–1552, 2000.

[10] S. R. White and R. M. Noack. Real-Space Quantum Renormalization Groups. *Phys.Rev.Lett.*, 68(24):3487, 1992.

[11] S. R. White. Density Matrix Formulation for Quantum Renormalization Groups. *Phys.Rev.Lett.*, 69(19):2863, 1992.

[12] S. R. White. Density-matrix algorithms for quantum renormalization groups. *Phys.Rev.B*, 48(14):10345, 1993.

[13] V. Madhavan, W. Chen, and T Jamneala. Tunneling into a Single Magnetic Atom: Spectroscopic Evidence of the Kondo Resonance. *Science*, 280(567), 1998.

[14] A. Abrikisov, L. P. Gorkov, and I. E. Dzyaloshinski. *Methods of quantum field theory in statistical physics.* Dover, 1963.

[15] A. Fetter and J. Walecka. *Quantum Theory of Maqny-Particle Systems.* McGraw-Hill Book Company.

[16] J. W. Negele and H. Orland. *Quantum Many Particle Systems.* Perseus Books, 1998.

[17] Yousef Saad. *Iterative methods for sparse linear systems.* SIAM, 2003.

[18] C. Lanczos. An Iteration Method for the Solution of the Eigenvalue Problem of Linear Differential and Integral Operators. *J.Res.Nat.Bur.Stand.*, 45, 1950.

[19] G. Golub and C. van Loan. *Matrix Computations.* North Oxford Academic, 1983.

[20] C. Paige. *The Computation of Eigenvalues and Eigenvectors of Very Large Sparse Matrices.* PhD thesis, London University, 1971.

[21] S. Kaniel. Estimates for Some Computational Techniques in Linear Algebra. *Math.Comp.*, 20(369-78), 1966.

[22] E. Dagotto. Correlated electrons in high-temperature superconductors. *Rev.Mod.Phys.*, 66(3), 1994.

[23] H. Bethe. *Z.Phys.*, 71(205), 1931.

[24] H.J. Schulz. The Metal-Insulator Transition in One Dimension. *cond-mat/9412036*, 1993.

[25] H.J. Schulz. Hubbard chain with reflecting ends. *J.Phys. C*, 18:581–601, 1985.

[26] S. Kneer. Diplomarbeit. 1997.

[27] J. Cardy. *Scaling and Renormalization in Statistical Physics.* Cambridge University Press, 1996.

[28] K. Wilson. *Rev.Mod.Phys.*, 47:773, 1975.

[29] I. Peschel et al. *Density-Matrix Renormalization.* Number 255-82. Springer-Verlag, 1998.

[30] B. Stroustrup. *The C++ Programming Language.* Addison-Wesley, 1997.

[31] K. Hallberg. Density-matrix algorithm for the calculation of dynamical properties of low dimensional systems. *Phys.Rev.B*, 52(14), 1995.

[32] T. Kühner and S. R. White. Dynamical correlation functions using the density matrix renormalization group. *Phys.Rev.B*, 60:335, 1999.

[33] U. Schollwöck. The density-matrix renormalization group. *Rev. Mod. Phys.*, 77(259), 2004.

[34] J. von Delft and D.C. Ralph. Spectroscopy of discrete energy levels in ultrasmall metallic grains. *Physics Reports*, 345(61), 2001.

[35] T. Hand, J. Kroha, and H. Monien. Spin-Correlations and Finite-Size Effects in a One-Dimensional Kondo-Box. *cond-mat/0602352*, 2006. to be submitted to PRL.

[36] W. Thimm, J. Kroha, and J. van Delft. Kondo Box: A Magnetic Impurity in an Ultrasmall Metallic Grain. *Phys. Rev. Lett.*, 82(10), 1999.

[37] I. Affleck. The Kondo Screening Cloud. *cond-mat/0111321*, 2001.

[38] R. Schrieffer and P. Wolff. *Phys. Rev.*, 149(491), 1966.

[39] E. Sorensen and I. Affleck. The Kondo Screening Cloud around a Quantum Dot: Large Numerical Results. *cond-mat/0409034*, 2004.

[40] S.R. White. private conversation, 2005.

[41] T. Xiang. Density-matrix renormalization-group method in momentum space. *Phys. Rev. B*, 53(R10445-R10448), 1996.

[42] G. Fano, F. Ortolani, and A. Parola. Unscreened Coulomb repulsion in the one dimensional electron gas. *cond-mat/9909140.*

[43] E. Arrigoni, A.P. Harju, and W. Hanke. Stripes and superconducting pairing in the t-J model with Coulomb interactions. *Phys. Rev. B*, 65(134503), 2002.

[44] A. Georges, G. Kotliar, and W. Krauth. Dynamical mean-field theory of strongly correlated fermion systems and the limit of infinite dimensions. *Reviews of Modern Physics*, 68(1), 1996.

[45] M. Caffarel and W. Krauth. Exact Diagonalization Approach to Correlated Fermions in Infinite Dimensions: Mott Transition and Superconductivity. *Phys.Rev.Let*, 72(10), 1994.

[46] T. Maier, M. Jarrell, and T. Pruschke. Quantum cluster theories. *Reviews of Modern Physics*, 77(1027), 2005.

[47] M. Capone, M. Civelli, S. Kancharla, C. Castellani, and G. Kotliar. Cluster Dynamical Mean-Field Theory of the density-driven Mott transition in the one-dimensional Hubbard model. *Phys. Rev. B*, 69(195105), 2004.

[48] C. Bolech, S. Kancharla, and G. Kotliar. Cellular Dynamical Mean Field Theory for the 1D Extended Hubbard Model. *Phys. Rev. B*, 67(075110), 2003.

Danksagung

An erster Stelle möchte ich Hartmut Monien für die interessante Aufgabenstellung danken. Er hat mir die Möglichkeit gegeben, meine Arbeit über ein faszinierendes Thema zu schreiben und mich dabei fachlich und persönlich hervorragend betreut. Ich bedanke mich recht herzlich bei Herbie Dreiner für die spontane Übernahme des Korreferats. Hans Kroha danke ich für viele interessante Anregungen und Diskussionen. Ich danke Steve White für die Zusammenarbeit und die zahlreichen guten Ratschläge, die mir bei der Arbeit immer eine Hilfe waren. Insbesondere danke ich meinen beiden Bürokollegen, Jerry Amadon und Christian Kolf, für die immer gute Arbeitsatmosphäre sowie zahlreiche Golf- und Schachspiele. David Heilmann und Andreas Fuhrmann waren während der ganzen Zeit immer hilfsbereit und verdienen meinen Dank nicht nur für zahlreiches Korrekturlesen. Ich danke Axel Grzesik für die ausgezeichnete Matrixklasse. Matthias Niemeyer danke ich, dass er sich immer Zeit genommen hat, um uns zu helfen, und mit seinen vielen Rätseln die Mittagspausen bereichert hat. Andreas Wisskirchen danke ich für die Beseitigung aller Computerprobleme. Patricia Zündorf und Dagmar Fassbender danke ich für die Hilfe in allen bürokratischen Fragen. Zum Abschluss geht ein großes Dankeschön an Carolin Neumann-Giesen und meine Eltern, die mich während der kompletten Zeit unterstützt haben.